UNIVERSITY of CALIFORNIA

Santa Barbara

Induced Magnetism and Symmetry Breaking within Strongly Correlated Oxide Heterostructures

A Dissertation submitted in partial satisfaction of the

requirements for the degree

Doctor of Philosophy

in

Materials

by

Ryan F. Need

Committee in charge:

Professor Stephen D. Wilson, Chair

Professor Ram Seshadri

Professor Susanne Stemmer

Professor Andrea Young

December 2017

The dissertation of Ryan F. Need is approved.

Professor Ram Seshadri

Professor Susanne Stemmer

Professor Andrea Young

Professor Stephen D. Wilson, Committee Chair

December 2017

Induced Magnetism and Symmetry Breaking

within Strongly Correlated Oxide Heterostructures

by

Ryan F. Need

for the family, friends, and mentors who helped me foster

the curiosity and confidence to pursue my dreams

Acknowledgments

There are many individuals who helped me leading up to and throughout my PhD, and to whom I owe my heartfelt thanks.

First and foremost, I would like to thank my advisor, Prof. Stephen Wilson, for all of his guidance, patience, and expert advice throughout our projects. A majority of these experiments were envisioned by Stephen, and without his assistance I would not have been able to execute them to the degree that I did. More importantly, I would like to thank Stephen for creating a safe and friendly working environment, for nuturing the professional growth of myself and others within the group, and for setting an incredible example as an academic advisor.

I would also like to thank the other members of my committee, Profs. Susanne Stemmer, Ram Seshadri, and Andrea Young, for their support and collaboration in our various projects together. Susanne and her students, Brandon Isaac and Patrick Marshall, were of course responsible for the outstanding thin film samples I was fortunate to be able to study. Moreover, it was only due to Susanne's long and thought-out study of these rare earth titanate films that we had the foundation of knowledge necessary to pursue and analyze our experiments. Ram, and his student Josh Bocarsly, were instrumental in analyzing the magnetocaloric potential of my FeGe crystals and without them I'm not sure anything

would have been published from those efforts. I also owe Ram a debt of gratitude for instilling in me high standards for figure making and presentations, as well as being a wonderful advisor to my wife and partner, Megan. Finally, Andrea and his group collaborated on our transition metal dichalcogenide work, making a valiant to exfoliate the rather tiny crystals I gave them and generally being a wonderful group to work with.

I also owe thanks to the many previous advisors, mentors, and collabotors I have had during my undergraduate studies and internships along the way, including: Prof. Molly Kennedy, Prof. Dave Bahr, Dr. Dan Josell, Dr. Chuck Mielke, Dr. Brian Kirby, and Dr. Julie Borchers.

To all the friends I made during my time in Santa Barbara, of which there are far too many to name, I want to thank you for making Santa Barbara feel more like home than any other place I have lived. I will always be grateful for the time we spent together and the memories we share. Each and every one of you is true friend and holds a special place in my heart.

To my parents, sister, grandparents, aunts, uncles, and cousins, thank you for being the most supporting of families and for finding time to celebrate together. To my parents and sister in particular, thank you for all your love and kindness throughout the years - you continually inspire me to be a better son, brother,

and human being.

Finally, to my wife, best friend, and partner, Megan, thank you. Thank you for everything. For your support throughout the program, for your belief in me as a person, and for agreeing to take this leap of faith with me and see where it leads together.

Curriculum Vitae

Ryan F. Need

Education

Sept. 2014–**Present** PhD Candidate

Materials Department, University of California, Santa Barbara

Advisor: Professor Stephen D. Wilson

Sept. 2012–**Sept. 2014** Graduate Student Researcher

Materials Department, University of California, Santa Barbara

Advisor: Professor Chris Palmstrom

Sept. 2007–**Dec. 2011** B.S. Ceramics and Materials Engineering

Materials Science and Engineering Department, Clemson University, Clemson

Graduation: Sum Cum Laude, Dec. 2011

Publications

6. **R.F. Need**, B.J. Issac, B.J. Kirby, S. Stemmer, and S.D. Wilson. Octahedral tilt independent magnetism in confined $GdTiO_3$ films. *Submitted for review.*

5. **R.F. Need**, P.B. Marshall, E. Kenney, A. Suter, T. Prokscha, Z. Salman, B.J. Kirby, S. Stemmer, M.J. Graf, and S.D. Wilson. Quasistatic antiferromag-

netism in the quantum wells of $SmTiO_3/SrTiO_3$ heterostructures. *Submitted for review.*

4. **R.F. Need**, B.J. Issac, B.J. Kirby, S. Stemmer, and S.D. Wilson. Interface-driven ferromagnetism within the quantum wells of a rare earth titanate superlattice. *Physical Review Letters*. 117 037205 (2016). [doi: 10.1103/PhysRevLett.117.037205]

3. **R.F. Need**, D.J. Alexander, R.D. Field, V. Livescu, P. Papin, C.A. Swenson, and D.B. Mutnick. The effects of equal channel angular extrusion on the mechanical and electrical properties of alumina dispersion-strengthened copper alloys. *Materials Science and Engineering A*. 565 450-458 (2013). [doi: 10.1016/j.msea.2012.12.007]

2. C.M. Hangarter, B.H. Hamadani, J.E. Guyer, H. Xu, **R.F. Need**, and D. Josell. Three dimensionally structured interdigitated back contact thin film heterojunction solar cells. *Journal of Applied Physics*. 109 7 (2011). [doi: 10.1063/1.3561487]

1. D.J. Morris, **R.F. Need**, M.J. Anderson, and D.F. Bahr. Enhanced actuation and acoustic transduction by pressurization of micromachined piezoelectric diaphragms. *Sensors and Actuators A*. 161 1-2 (2010). [doi: 10.1016/j.sna.2010.05.028]

Abstract

Induced Magnetism and Symmetry Breaking

within Strongly Correlated Oxide Heterostructures

by

Ryan F. Need

In strongly correlated electron systems, the independent electron approximation fails and electron-electron correlations must be taken into consideration. Such systems display an abundance of technologically useful behaviors including metal-insulator transitions, superconductivity, and colossal magnetoresistance. Within the broad class of correlated materials, Mott insulators are a canonical example. These compounds have repulsive Coulomb interactions between on-site electrons large enough to open an energy gap between two portions of a valence band, thereby turning what conventional band theory would predict to be a metal into a (Mott) insulator. Despite many years of investigation, Mott insulators remain an exciting area of materials research owing in part to their proximity to quantum critical points and spin liquid ground states.

Here we have studied thin films of the Mott insulating rare earth titanates

RTiO$_3$ (R = Gd, Sm), and heterostructures of these compounds with the band insulator SrTiO$_3$. At the RTiO$_3$/SrTiO$_3$ interface, electrostatic doping creates a two-dimensional electron liquid (2DEL) that resides within the SrTiO$_3$ layer near the interface. In the case of thin SrTiO$_3$ quantum wells between magnetic RTiO$_3$ barriers, we used polarized neutron reflectometry and muon spin rotation to show that there is a critical well thickness below which the 2DEL electrons exhibit magnetic correlations. This critical thickness was found to be independent of the sign of the magnetic exchange interactions in the neighboring RTiO$_3$ barriers. A follow up study on thin GdTiO$_3$ embedded within SrTiO$_3$ revealed magnetic dead layers at the interface of the two materials, but bulk-like ferrimagnetism within the center of the thin GdTiO$_3$ layers. The independence of magnetism from the notable structural distortions observed within the thin GdTiO$_3$ layers highlights the weak coupling between the magnetic exchange interactions and electronic bandwidth in this material. Finally, element-specific resonant X-ray measurements were used to probe electronic symmetry breaking within SmTiO$_3$ films and found evidence for in-plane orbital polarization at room temperature. Together, these studies add to the collective understanding of electron-electron correlations within Mott insulating thin films, particularly those in proximity to a high-density 2D electron system.

Contents

List of Figures

Chapter 1

Introduction

Correlations are simply relationships between two or more objects. Those objects can be physical particles in a solid, variables in a mathematical model, or even people. The correlation between two objects – the way they interact – can take any number of functional forms from a simple linear relation to a discontinuous step-like pattern. However, regardless of the exact nature of the correlation, its presence is usually enough to have an observable effect on the system's collective behavior. For example, consider a dinner party in which one of the attendees is being rude to the other guests. That individual's interaction with the the other guests will almost certainly sour the mood of the whole party. Similarly, we can consider an ordered ferromagnet in which one of the magnetic

moments is anti-aligned. This raises the energy of the entire system of spins relative to the fully aligned ground state.

It is also important to remember that correlations can themselves be correlated to an external variable. In other words, the relationship between two objects may depend on a third object. Consider this time stubbing your toe on an uneven sidewalk as you as a friend are walking outside. If it is just the two of you, you might use some colorful language to express your displeasure. However, if one of you is pushing a sleeping child in a stroller, your observable external response is likely to be muted. In other words, the correlation between pain and its expression is modified by your environment and the people in it. For a more scientific example, we can consider climate change in which a famously large number of parameters are cross-correlated creating complex feedback cycles [1].

There are two points here. First, just because two objects are correlated, it does not mean that there is a causal relation between them. For example, both the Earth's average surface temperature and the percentage of CO_2 in the atmosphere have increased as a function of year over the last 100 years. However, no one (at least that I am aware of) is claiming that the aging of the Earth is responsible for the additional carbon dioxide in the air. The second point is that studying the correlations between measurable parameters – whether they are

related to climate change, electronic solids, or human behavior – is one of the most important ways we have to understand the world around us. Through the careful study of correlations, it is possible to determine which correlations *are* causally related and therefore provide us proverbial knobs and levers we can use to move the world toward our vision.

1.1 Correlated Electron Systems

In condensed matter physics, correlations often refer specifically to electron-electron correlations. A correlated electron system is therefore one in which interactions between electrons cannot be ignored. The opposite is an uncorrelated electron system in which individual electrons within a material are assumed to be non-interacting. This simplifying condition of non-interacting electrons, first proposed by Drude [2], turns out to be a surprisingly good description of many materials, particularly when the quantized nature of electronic states was added to the model by Sommerfeld [3]. The resulting free electron (or Drude-Sommerfeld) model forms the basis of electronic band theory that works well for many simple metals, semiconductors, and insulators [4].

However, in the years since the Drude-Sommerfeld model was introduced, a number of materials were found to violate the independent electron assump-

tion [5]. Broadly speaking, these materials can be lumped into two categories: transition metal oxides and rare earth intermetallics. The first group includes materials such as superconducting cuprates [6, 7] and colossal magnetoresistance manganites [8, 9]. The Mott insulating rare earth titanates $GdTiO_3$ (GTO) and $SmTiO_3$ (SmTO) studied in this thesis also belong to this category. The rare earth intermetallics group is also referred to as heavy metal fermions. It hosts materials like $CeAl_3$ [10] and $Ce(Pd,Cu)_2Si_2$ [11] that display a combination of superconductivity, low temperature transport phenomena, and quantum criticality [12, 13]. Today the materials community studies a variety of strongly correlated materials to better understand the nature of electron-electron interactions under different constraints and study the so-called emergent phenomena that arise from the competitive ground states found in these systems [14].

1.2 Rare Earth Titanates in Bulk and Thin Film

As noted above, the rare earth titanates (RTO) are one of many transition metal oxide families with strong electron correlations. The entire RTO series, where R is a trivalent ion from the lanthanide series, has been extensively studied in their bulk form through both experiment and theoretical calculations. These compounds are Mott insulators with a single electron in the 3d orbitals

and crystallize in the orthorhombic space group $Pnma$ or $Pbnm$ (No. 62) [15]. The structure is a distorted perovskite in which the oxygen octahedra that surround the titanium sites deviate from the ideal cubic perovskite by a series of cooperative tilts and rotations often referred to as a $GdFeO_3$-type distortion [16]. This distortion is present across the entire R series, though it increases in magnitude moving from large to small ionic radii (i.e. from La to Lu). In addition to the $GdFeO_3$-type distortion, which causes only minor deviations in the cubic symmetry of the octahedra during their rotation, the smaller end of the RTO series (e.g. Gd, Tb, Yb) displays a significant Jahn-Teller distortion that strongly breaks cubic symmetry [16, 17].

Given the single d^1 electron in this system and the nominal cubic symmetry surrounding the Ti ion, it is perhaps surprising that only part of the RTO series undergoes this Jahn-Teller distortion that lifts the t_{2g} degeneracy. Adding to this puzzle were experimental observations of orbital-ordered, non-degenerate ground states in a number of RTO compounds, including $LaTiO_3$ which has the smallest Jahn-Teller distortion [18, 19]. This seeming conflict was resolved by electronic structure calculations that showed in the larger radii R ions with small Jahn-Teller distortion, the R crystal field breaks the t_{2g} degeneracy and stabilizes an orbital-ordered ground state [15, 20].

This same model of crystal field competition explains the magnetic cross over

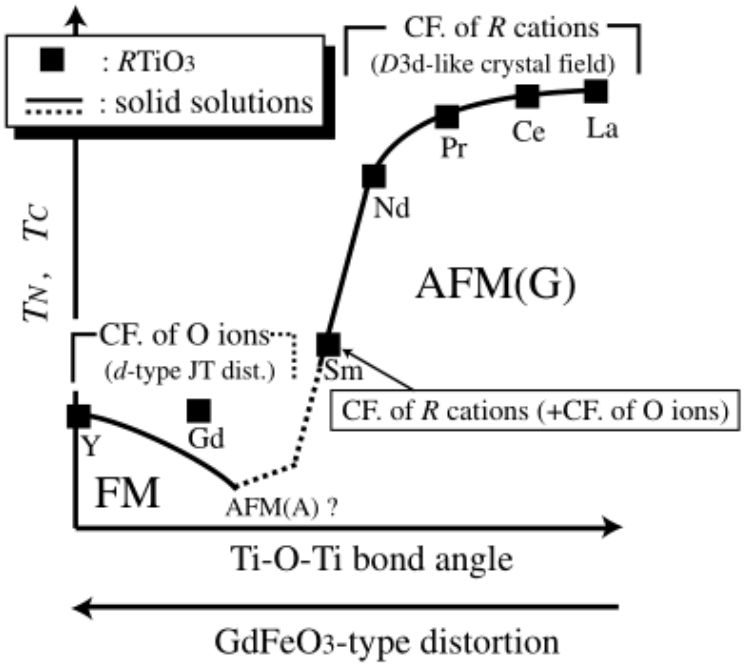

Figure 1.1: Magnetic phase diagram for the $R\mathrm{TiO}_3$ series highlighting the effects of competing R and O crystal fields. From Ref. [15].

that occurs between $SmTiO_3$ and $GdTiO_3$ [15]. $SmTiO_3$ and all RTO members with larger ionic radii (e.g. R = La-Pm) possess an antiferromagnetic ground state with Neél temperatures that decrease with decreasing ionic radii [21]. The remaining RTO members display either a ferromagnetic (R = Y) or ferrimagnetic ground state with no clear trend between Curie temperature and ionic radii [22]. This magnetic transition coincides with the onset of a strong Jahn-Teller distortion in the series and the weakening influence of the R crystal field. The general picture that arises is one where competition between crystal fields from the R and O ions acts in conjunction with changing structural distortions to determine both the electronic and magnetic ground states across the R series. This is summarized in Fig. 1.1.

Less work has been done on the these materials in thin film form as the growth of these RTO materials in epitaxial thin films is challenging due to the difficulty stabilizing the Ti^{3+} valence state and perovskite structure. The films are easily over-oxidized resulting in the related pyrochlore structure [23]. Therefore growth, whether by molecular beam epitaxy or pulsed laser deposition, usually proceeds under low oxygen pressures. However, this frequently results in the formation of oxygen vacancy defects that can dramatically alter the electrical and magnetic properties of the system [24–26]. Recently, a hybrid molecular beam epitaxy (MBE) approach has been developed for some RTO

compounds that generates remarkably stoichiometric films [27–29]. The low defect density and high interface quality of these films has allowed unprecedented experimental access to the intrinsic properties of these materials in thin film form.

1.3 RTiO$_3$/SrTiO$_3$ Interfaces and Heterostructures

The work in this thesis investigates thin film heterostructures of RTO and $SrTiO_3$ (STO) grown by hybrid molecular beam epitaxy. At the interface of these materials, a fixed charge density arises due to an electrostatic discontinuity between the polar RTO and non-polar STO layers as shown in Fig. 1.2 [30]. Transport measurements of GTO/STO heterostructures show that the total carrier concentration of a film increases linearly with the number of interfaces [31], and unequivocally demonstrates that conduction at these interfaces is not due to charged defects, but the precise transfer of 1/2 an electron per surface unit cell. Due to the band alignment between RTO and STO, this fixed charge leads to a two-dimensional electron liquid (2DEL) with a sheet charge density of $\sim$3 x 10^{14} cm^{-2} that resides within the STO layer and is confined to $\sim$3 nm from the interface [31].

Another effect to consider at RTO/STO interfaces is the tuning of TiO_6 octa-

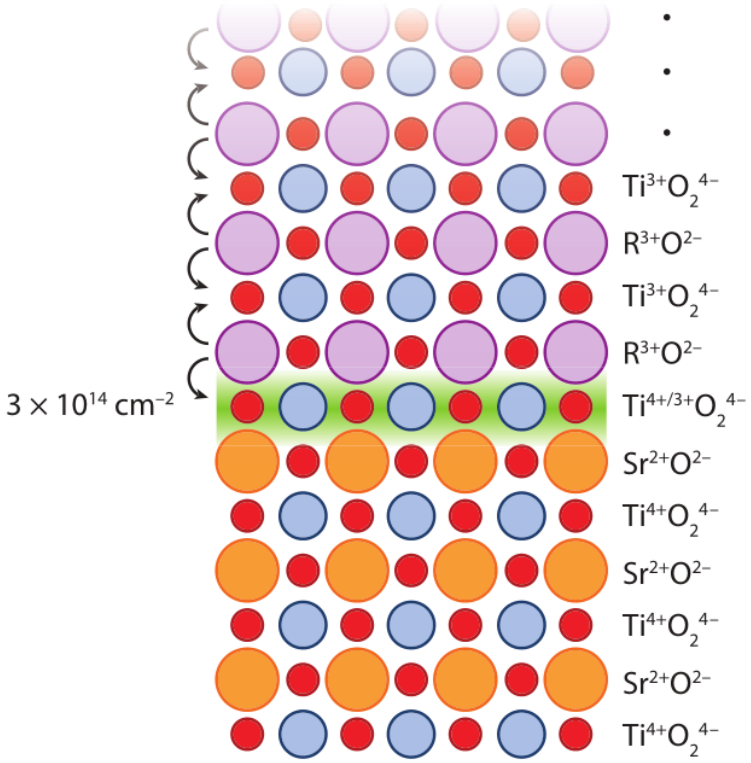

Figure 1.2: Schematic of electrostatic doping of STO/RTO interfaces leading to the formation of a high-density, two-dimensional electron liquid. From Ref. [30].

hedra tilts between the fully tilted bulk structure of RTO and the untilted cubic structure of STO. When either the RTO or STO layers are made sufficiently thin and embedded within thicker barrier layers of the other material, the tilting pattern of the well material is distorted towards that of the barrier layers [32, 33]. For STO wells in a RTO matrix, the induced tilting in STO is less in the case of SmTO barriers than for GTO barriers [34]. This corresponds to a true Mott insulating metal-insulator transition in GTO/STO, and the absence of a metal-insulator transition altogether in SmTO/STO.

1.4 Chapter Overviews

Our goal in the work of this thesis was to investigate magnetism and orbital ordering, features known to be present and important to the understanding of bulk RTO, in thin films and heterostructures of these materials.

Chapter 2 begins with detailed descriptions of the experimental methods used during our studies. First, the background and fundamental concepts for reflectometry are discussed. This is the basic scattering technique we have used to resolve magnetism and orbital polarization as a function of depth into complex thin film heterostructures. Differences between X-ray and polarized neutron reflectometry (PNR), such as atomic scattering lengths and polarization channels,

are discussed as well as how these differences result in techniques that both contrast and complement one another. Finally, this chapter reviews a collection of muon-based techniques known as μSR that is based upon particle implantation and decay rather than diffraction. Together these techniques provide an incredibly powerful means of studying physics in buried layers and interfaces.

In Chapters 3–6, we describe four separate experimental studies that probed changes in electron-electron correlations in RTO/STO heterostructures. Each chapter is a self-contained story with specifically tailored introductory information needed to understand our results and place them into the broader context of correlated transition metal oxides.

The first study in Chapter 3 uses polarized neutron reflectometry to observe an induced-ferromagnetic state in STO quantum wells constrained between GTO barriers. However, this state only appears below a critical STO layer thickness, or correspondingly, above a critical electron density in the well. Our data demonstrate that the interplay between proximate molecular exchange fields and itinerant carriers can stabilize extended magnetic states within STO quantum wells, and constitutes the likely origin of quantum critical transport in this system.

In Chapter 4 we again use polarized neutron reflectometry to explore GTO/STO heterostructures and find evidence for magnetic dead layers at

GTO/STO interfaces. However, bulk-like ferrimagnetism persists within the center of GTO layers even as the GTO layers are thinned towards a single unit cell and the titania octahedral network within those layers is distorted. These results suggest an independence between structural distortions and magnetic correlations that is masked in bulk magnetometry measurements.

The study in Chapter 5 investigates thin STO quantum wells embedded within antiferromagnetic SmTO barriers using a combination of μSR and supporting PNR measurements. We observed slow magnetic fluctuations that begin to freeze into a quasistatic spin state below a critical temperature of $\sim$20 K. This onset coincides with the opening of a pseudogap in the tunneling spectra, and PNR data show that these fluctuations must be antiferromagnetic in origin. Together, this data suggests a common physical model of the pseudogap state observed in this thin film system and those observed in bulk, antiferromagnetic Mott insulators. Lastly, these low temperature magnetic correlations are only observed in STO quantum wells below the same critical layer thickness found for the GTO/STO system, strengthening the notion that above a critical electron density itinerant electrons in STO are capable of propagating adjacent molecular fields.

Finally, in Chapter 6 we use resonant X-ray reflectometry (RXR) and X-ray absorption spectroscopy (XAS) to investigate orbital polarization in the

SmTO/STO system. From XAS measurements, we find all samples capped with a SmTO layer exhibit an oxidized surface such that the titanium is closer to a Ti^{4+} valence state than its nominal Ti^{3+} state. Therefore, RXR data measured across the Ti $L_{2,3}$-edges were analyzed within a model of an oxidized surface layer and the anomalous scattering factors for buried titanium were refined. Refinements of a pure SmTO control film reveal that the surface oxidation only penetrates 2-3 nm into the film, and that the buried SmTO contains the correct Ti^{3+} state. Moreover, fitting of the linear polarization asymmetry suggests that SmTO thin films have a polarization favoring the in-plane orbitals, opposite expectations from the film's compressive epitaxial strain. Furthermore, these results provide good agreement when used as fixed input to refine data for superlattice heterostructure. Orbital polarization with embedded STO quantum wells is shown to require a similar polarization preference to the neighboring SmTO layers.

Chapter 2

Experimental Methods

2.1 Thin Film Growth

The thin film samples used for experiments in this dissertation were grown using hybrid molecular beam epitaxy (MBE) by members of Prof. Susanne Stemmer's group. The hybrid MBE technique differs from traditional, solid source MBE in that it uses a metal-organic precursor, specifically, titanium tetraisopropoxide (TTIP), as the source of both Ti and O atoms but retains the use of solid sources for cation elements such as Sr, Gd, and Sm [35, 36]. Compared with other MBE methods for oxide film growth, this strategy possesses a number of advantages. First, it eliminates the need for complicated ozone or

rf plasma sources to supply oxygen during growth. Second, TTIP has a vapor pressure many orders of magnitude larger than elemental Ti facilitating faster growth rates [35]. Third and most importantly, the use of TTIP and hybrid MBE opens up a growth window in which the cation stoichiometry is self-regulating at practical substrate temperatures [36, 37]. Without such a growth window, oxide growth requires high precision flux calibrations and yet still tends to result in poor stoichiometry control, as evidenced by the dramatic improvements in defect density and carrier mobility achieved using hybrid MBE to grow STO [38].

All STO, GTO, and SmTO films and heterostructures studied were grown on (001) $(La_{0.3}Sr_{0.7})(Al_{0.65}Ta_{0.35})O_3$ (LSAT) substrates by hybrid MBE. The materials were grown in co-deposition mode on a heated substrate. Layer thicknesses were controlled with near atomic layer precision using in-situ reflection high-energy electron diffraction (RHEED). All samples were below the critical thickness for strain relaxation as evidenced by X-ray diffraction and atomic force microscopy on numerous similar growths. Furthermore, samples were assumed to possess the epitaxial orientation and film morphology previous TEM studies had shown for similarly grown films. Specifically, the rare earth titanates with space group *Pnma* were oriented with the long *b*-axis in the plane of the film and [101] parallel to the substrate surface normal [36]. Due to the nominally

cubic symmetry of the underlying LSAT substrate, four crystallographic domain variants were assumed to be present, related by 90° rotations about the surface normal [33]. Further details regarding the electronic and magnetic properties of these films and heterostructures can be found in Ref. [27, 31, 32, 34, 39] and in the introductions of the subsequent chapters.

2.2 Reflectometry Overview

Reflectometry is a analytical technique that uses the interference of radiation reflected from surfaces and interfaces to characterize a material's composition and structure. While primarily applied to thin films or stacks of films, the technique is applicable to a wide range of materials and scientific inquiries, including: diffusion and magnetism in metallic multilayers [40–42], interfacial phenomena in magnetic oxides [43–45], structural stability in lipid bilayers [46, 47], and order and adsorption in copolymers [48–50] to name a few. This flexibility is due in part to the fact that depending on the form of incident radiation chosen, the technique will have different sensitivity to various chemistries and structural length scales. For example, X-rays are generally more sensitive to heavy elements while neutrons often provide better results with light elements and adjacent 3d transition metals. Similarly, cold neutrons and soft X-

rays, with their longer wavelengths, are better suited to films several nanometers or greater in thicknesses, while thermal neutrons and hard X-rays can probe sub-nanometers length scales more effectively. Regardless of the material(s) being investigated or the form of radiation, much of the underlying mathematics of reflectometry is identical. The following sections present an overview of important concepts and mathematical relations used to calculate the reflectivity from a theoretical film stack.

2.2.1 Fresnel Equations and Refractive Index

We begin by considering a light wave of amplitude E and wavevector k incident on a single interface between two materials with dissimilar indices of refraction n as sketched in Fig. 2.1. As the light wave hits the interface, part of the wave's intensity will be transmitted while part will be reflected. Equations to describe the ratio of reflected (r) and transmitted (t) light intensity relative to the intensity of the incident light, as the wave moves from material 1 into material 2, were written down by the French physicist and optics expert Augustin-Jean Fresnel [51]:

$$r_\sigma = \frac{E_r}{E_i} = \frac{n_1 cos\theta_i - n_2 cos\theta_t}{n_1 cos\theta_i + n_2 cos\theta_t} \tag{2.1}$$

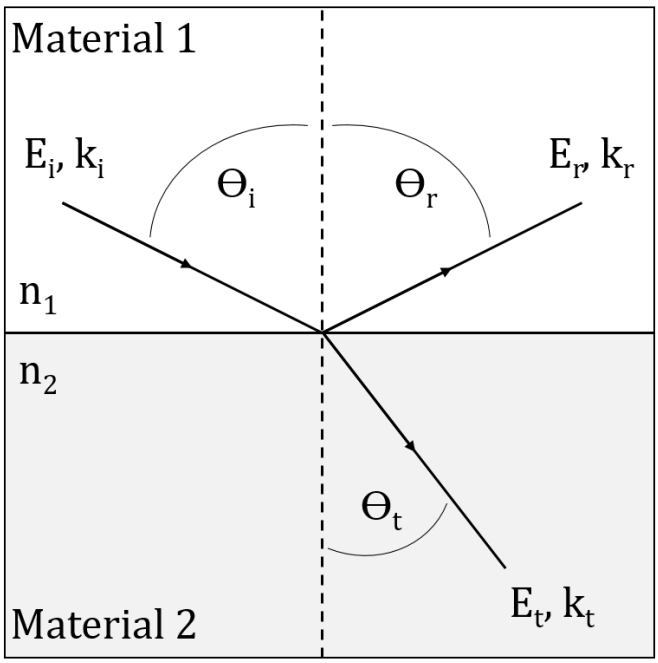

Figure 2.1: Schematic of Fresnel reflection and transmission at an interface.

$$r_\pi = \frac{E_r}{E_i} = \frac{n_1 cos\theta_t - n_2 cos\theta_i}{n_2 cos\theta_i + n_1 cos\theta_t} \tag{2.2}$$

$$t_\sigma = \frac{E_t}{E_i} = \frac{2n_1 cos\theta_i}{n_1 cos\theta_i + n_2 cos\theta_t} \tag{2.3}$$

$$t_\pi = \frac{E_t}{E_i} = \frac{2n_1 cos\theta_i}{n_2 cos\theta_i + n_1 cos\theta_t} \tag{2.4}$$

where n_1 and n_2 are the refractive indices of materials 1 and 2, respectively. Equations 2.1–2.4 are interrelated through the reversibility of the optical path and the conservation of energy [52], which imply that $r_{ij} = -r_{ji}$ and $t_{ij} = 1 - r_{ij}$, where i and j are adjacent layers in a film stack.

Note that there are two equations for reflection and two for transmission. One set corresponding to each of the fundamental linear polarization channels, where the σ channel corresponds to an electric field vector perpendicular to the scattering plane while the π channel has the electric field vector in the scattering plane. This distinction is necessary because, as the equations suggest, the reflection or transmission of light depends on its polarization. This principle underlies everyday objects like polarized sun glass lenses, and also forms the basis of a related experimental technique known as ellipsometry.

The refractive index of a material is intimately tied to its chemical composi-

tion. Therefore, measuring the amount of light reflected or transmitted by an interface at a known angle provides information about the chemistry of the two materials creating the interface. More specifically, the refractive index of a material, its dielectric permittivity tensor ϵ, and its electric susceptibility tensor χ are related back to atomic density N_i and scattering length f_i of element i as follows [52]:

$$n^2 = \epsilon = 1 + \chi \propto \sum_i N_i f_i. \tag{2.5}$$

The exact relations between atomic density, scattering factors, and refractive index depend upon the type of incident radiation, and is treated separately for electromagnetic radiation and neutrons in Sections 2.3 and 2.4, respectively.

2.2.2 Recursion Algorithms

While the Fresnel equations lay important groundwork for understanding and calculating the reflectivity of materials, they are insufficient to handle real systems. To highlight why this is the case, consider that even a single layer film will have two relevant interfaces (e.g. film-air and substrate-film, or top and bottom). This leads to multiple beam reflections as depicted in Fig. 2.2. As additional layers are added to the film stack, the situation quickly becomes more

complicated as each wave transmitted through one interface has some probability of reflecting or transmitting at the next interface. In theory, solving this problem can be thought of as summing all the partially reflected and transmitted waves incident on an interface from both above and below. However, in practice, the problem can be simplified by instead solving the wave field at each interface using the Fresnel equations and a recursive algorithm, the first variant of which was introduced by Lyman Parratt [53]. Parratt's recursive solution takes the form:

$$R_i = \frac{r_i + R_{i+1} e^{2ik_{i_1} d_{i+1}}}{1 + r_i R_{i+1} e^{2ik_{i_1} d_{i+1}}}. \tag{2.6}$$

Here r represents the same Fresnel coefficients defined above, while R_i is the total ratio of reflected and transmitted electric field amplitudes within layer i. The recursion begins by assuming a semi-infinite substrate from which no transmitted light is reflected back, then solving for R_N in the bottommost layer and working sequentially back toward the surface interface.

The advantage of Parratt's formalism is its simplicity, which in turns leads to quick and stable computation. The disadvantage of this approach is that it can only be used to calculate σ or π polarized light. Any evaluation of unpolarized or circularly polarized light using the Parratt algorithm requires an assumption

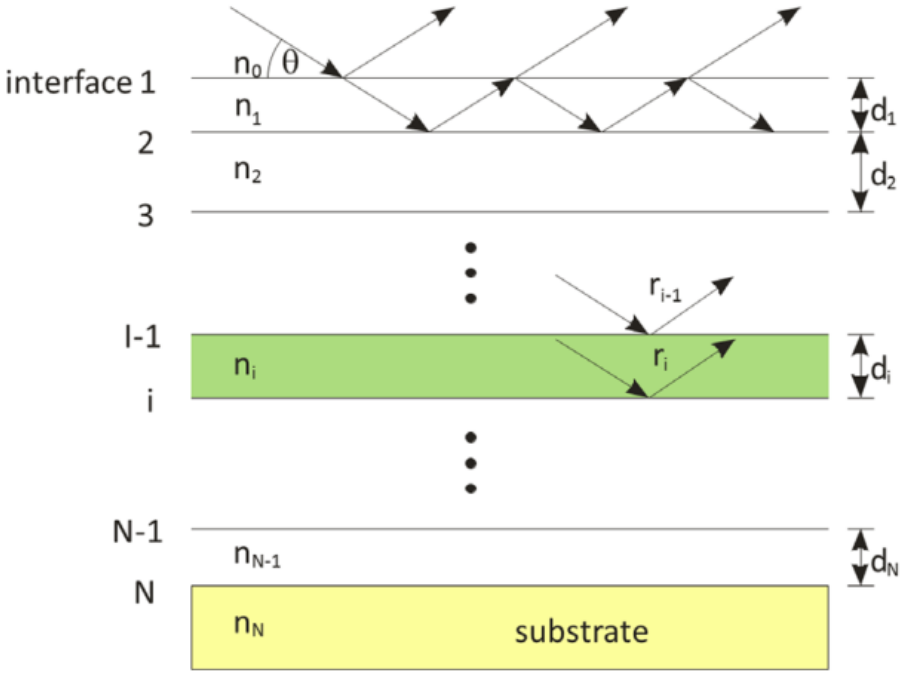

Figure 2.2: Schematic of light propagating and reflecting within a multilayer stack highlighting the problem of multiple reflections. Adapted from Ref. [52]

about how to average of the two linear polarization channels to approximate the desired polarization state [52]. This works reasonably well for isotropic materials examined with unpolarized light, but generally fails to handle anisotropic or magnetic materials.

When a more precise treatment is required, either due to the material or polarization, then reflectivity is calculated by a transfer matrix or optical matrix formalism [52, 54, 55]. This method relies on the continuity of the electric field E and its derivative across each interface as required by Maxwell's equations [51]. Specifically, these conditions can be written as:

$$E(z) = E_t e^{ikz} + E_b e^{-ikz} \tag{2.7}$$

$$\frac{dE}{dz} = ikE_t e^{ikz} - ikE_b e^{-ikz} \tag{2.8}$$

where the subscripts t and b refer to light waves coming from the top or bottom of a layer, respectively, and the film layers are stacked in the z direction. For a layer of thickness d, the propagation matrix describing how the electric field changes from one interface to the next is:

$$M_i = \begin{bmatrix} cos(kd_i) & \frac{1}{k}sin(kd_i) \\ -ksin(kd_i) & cos(kd_i) \end{bmatrix} \tag{2.9}$$

$$\begin{bmatrix} E(z+d_i) \\ \frac{dE}{dz}(z+d_i) \end{bmatrix} = M_i \cdot \begin{bmatrix} E(z) \\ \frac{dE}{dz}(z) \end{bmatrix} \tag{2.10}$$

A stack of N layers is then described by the product of all individual layer matrices M_N. Note that Maxwell's equations also require continuity of the magnetic field across an interface, leading to four continuity conditions and 4 x 4 matrices [52]. However, for simplicity of illustrating the mathematical process, only the electric field has been considered reducing the system to 2 x 2 matrices.

To determine the reflectivity or transmission of the stack, boundary conditions similar to those used in the Parratt formalism are applied (i.e. semi-infinite substrate and vacuum top surface) and the system matrix M_N is solved. The reflectivity of the stack can then be written in terms of the system matrix elements M_{ij} as follows:

$$R = \left| \frac{(M_{21} + k_b k_t M_{12}) + (i(k_b M_{22} - k_t M_{11})}{(-M_{21} + k_b k_t M_{12}) + (i(k_b M_{22} + k_t M_{11})} \right|^2 \tag{2.11}$$

This type of matrix algorithm has the flexibility and sophistication to rigorously treat any variety of light polarization and material anisotropy. Therefore,

all of the reflectivity refinements and models described in the chapters below were calculated using a matrix method.

2.3 Resonant X-ray Reflectometry

Resonant X-rays are electromagnetic radiation with energy $\hbar\omega$ corresponding to the energy gap between a core atomic energy level and an unoccupied excited state near the Fermi level [56, 57]. Because these atomic level transitions are unique for each element, resonant X-rays provide unique sensitivity to specific elements within a material. However, the ability to access these resonant energies requires a bright, tunable X-ray source (i.e. a synchrotron). When resonant X-rays are absorbed by an atom, they excite a virtual transition that increases the scattering cross-section. That enhancement depends strongly on the *local* environment of the the resonant atomic species within the host material [56, 58]. Therefore, the use of resonant X-rays can provide information about the spin, charge, and orbital configuration of the probed atoms that cannot be obtained using off-resonant X-rays.

This section adds to the preceding reflectometry considerations presented in Section 2.2, all of which apply to resonant X-ray reflectometry (RXR), by reviewing theoretical and experimental concepts needed to understand how the

resonant absorption process changes the atomic scattering length densities that are needed to calculated a layer's refractive index and ultimately a film's reflectivity.

2.3.1 Components of the Atomic Scattering Factor

The total atomic scattering length f_i, also called the scattering factor or form factor, describes how the amplitude and phase of incident plane wave is altered during scattering with an atom of species i [56]. In the case of X-rays, the scattering length is the result of several different scattering mechanisms including resonant and non-resonant processes [52, 59]. Following the treatment by Hannon *et al.* [60] within the dipole approximation, which assumes all higher order transition processes can be neglected because of their small probabilities [61], results in a total scattering length described by:

$$\begin{aligned} f(q,\omega,e_f,e_i) = &-(e_f \cdot e_i) \cdot [f_0(q) + f_1(\omega) + if_2(\omega)] \\ &+i(e_f \times e_i) \cdot b[m_1(\omega) + im_2(\omega)]. \end{aligned} \tag{2.12}$$

In Eq. 2.12, b is the atomic magnetic moment vector and m_1 and m_2 are resonant magnetic scattering terms related to a bound-bound excitation [52]. Unlike the three preceding non-magnetic terms, these magnetic scattering pro-

cesses change the polarization during scattering resulting in different scattered intensity at the detector depending on the configuration of a polarization analyzer crystal placed in the scattered beam before the detector. This method of the polarization analysis can be very helpful for disentangling various scattering mechanisms in resonant X-ray scattering [18, 62]. However, for the RXR experiments conducted here, no polarization analyzer was used and all polarization states were collected with equal probability. Furthermore, in the case of the $SmTiO_3$/$SrTiO_3$ films we studied, the nanoscale four-fold symmetric domain structure [33] combined with a small Ti magnetic moment [63] result in a negligible magnetic contribution to the total scattered intensity.

Therefore, only the first three terms in Eq. 2.12 are relevant to the modeling and interpretation of the RXR experiments discussed in Chapter 6. The first term f_0 is derived from the Thomson scattering process and is proportional to the total number of electrons of the atom [64]. This process does not depend strongly on the photon's incident energy, and thus away from the resonant absorption edges it constitutes the dominant (for most purposes, only) scattering process. The Thomson scattering process does depend on the momentum transfer q=k_f-k_i of the scattering event. However, these values are well known and tabulated [65].

The remaining two terms are known as the anomalous scattering factors with f_1 sometimes being referred to as the dispersive term and f_2 the absorptive term

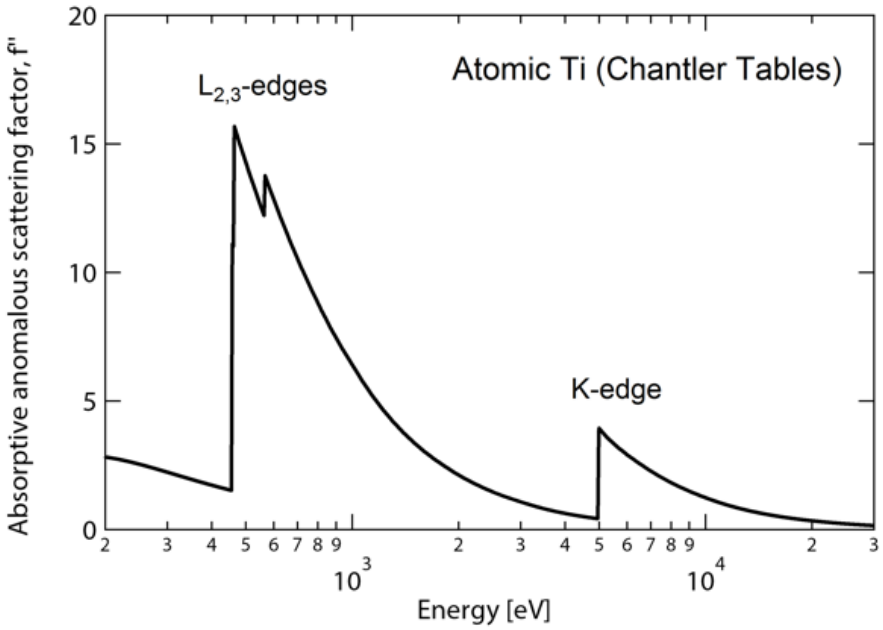

Figure 2.3: X-ray scatter factors of titanium, showing characteristic jumps at the absorption edges. Values taken from the Chantler tables [69].

[52]. Each term corresponds to a different energy-dependent scattering process but are both related, in a classical sense, to envisioning the atom as a collection of dipole oscillators with resonant frequencies equal to the differences in atomic energy level [66]. The dispersive term relates to an excitation from a bound core state to an unbound continuum of states and results in a series of characteristics steps in the absorption cross-section as shown in Fig. 2.3 [67]. Values for f_1 can be found in tables by Henke [68] and Chantler [69].

The absorptive term describes the virtual transition from a bound core state

to a bound unoccupied state near the Fermi level [52]. Because the final state in this process is typically a valence state, its energy dependence across the absorption edges is intimately related to the atom's local environment, including its charge and crystallographic symmetry [58, 61]. This absorptive scattering process forms the basis of X-ray absorption spectroscopy (XAS) [67, 70]. Furthermore, by experimentally measuring the XAS, it is possible to extract the anomalous scattering factors so that they can then be used as input for reflectometry modeling.

2.3.2 Measuring the Anomalous Scattering Factors

While RXR measurements collected at non-resonant energies can rely on tabulated values to provide the atomic scattering factors necessary to calculate layer refractive indices and the sample's reflectivity, this is not the case for RXR measurements on or near an absorption edge. In this case, the easiest and most accurate approach is to measure the X-ray absorption spectra of the RXR samples as well as any relevant sample standards [52]. For example, when looking at $SmTiO_3/SrTiO_3$ films, there is nominally Ti^{3+} in $SmTiO_3$ and Ti^{4+} in $SrTiO_3$. Therefore, standards for both Ti valence states in O_h symmetry should be measured to provide a comparison to the spectra measured from the het-

erostructures themselves. The XAS can be collected in surface-sensitive total electron yield mode or bulk-sensitive fluorescence yield mode [71]. Each mode has advantages and disadvantages and care should be taken when choosing which mode to use for a given sample depending on its thickness and composition [72]. However, many instruments today allow both modes to be collected simultaneously [73].

The measured XAS, an example of which is shown for the Ti $L_{2,3}$-edges of a $SmTiO_3$ film in Fig. 2.4, is then scaled and cut into the tabulated non-resonant values for f_2 from the Henke or Chantler tables (c.f. Fig. 2.3). This scaling converts the measured XAS data directly into meaningful units. The dispersive anomalous scattering factors f_1 are then calculated using the Kramers-Kronig relation [74]:

$$f_1(\omega) = \frac{2}{\pi} P \int_0^\infty \frac{\omega\prime f_2(\omega\prime)}{\omega^2 - \omega\prime^2} d\omega\prime \tag{2.13}$$

where P is the Cauchy principle value. Kramers-Kronig transform calculators are freely available online, including one associated with the ReMagX software [52, 75] used for the refinement of RXR data in this work.

The resulting values should look something like Fig. 2.5 where the inset clearly shows the XAS structure at the absorption edge has been preserved and

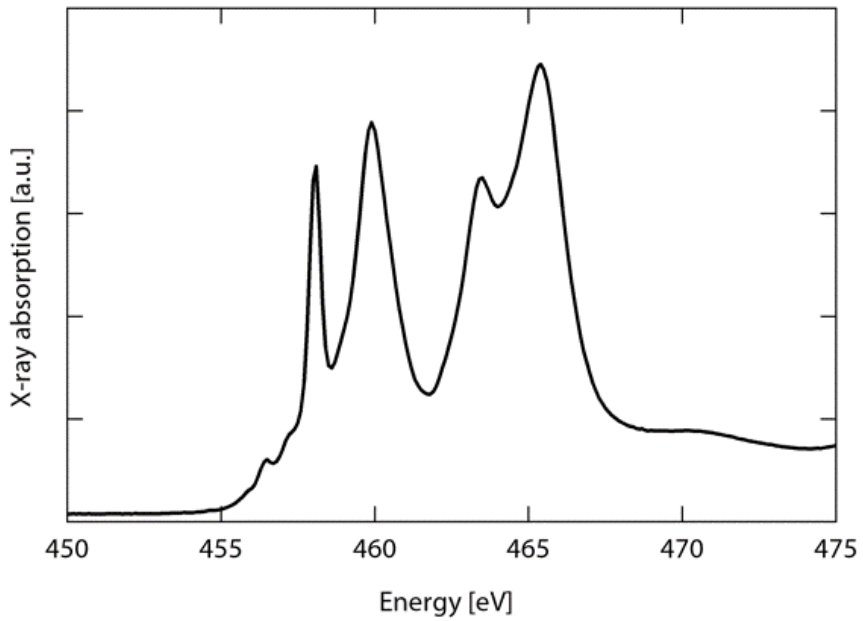

Figure 2.4: X-ray absorption spectra of a $SmTiO_3$ film collected at the Ti $L_{2,3}$-edges.

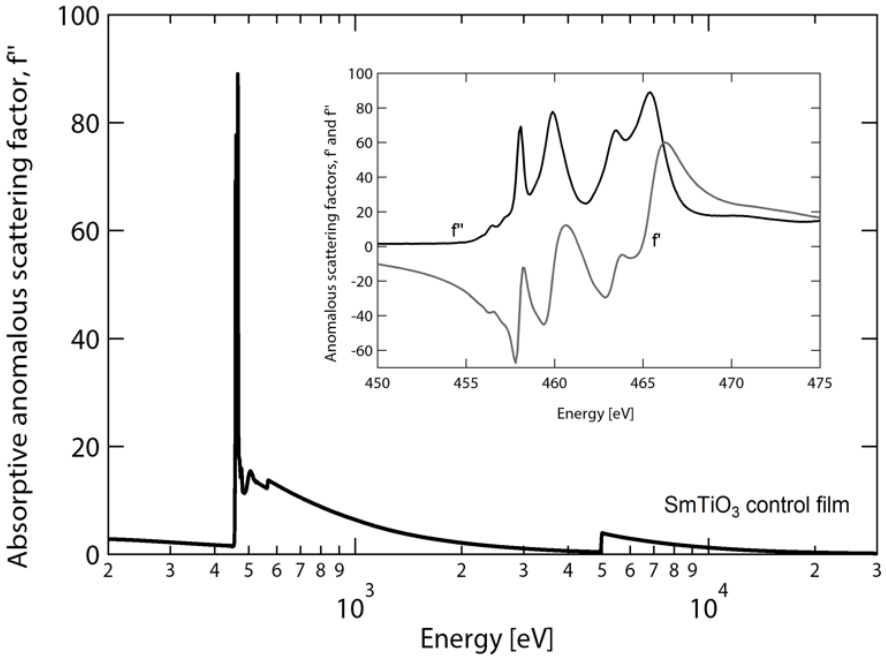

Figure 2.5: Anomalous scattering factors calculated from XAS spectra and the Kramers-Kronig transformation.

a corresponding change in the dispersive term can be seen across the absorption edge energies. These values are then ready to be input into a reflectivity refinement program like ReMagX [52] or GenX [76] that will implement a recursive algorithm to solve for the reflectivity of the sample(s).

2.3.3 Instrument Specifications

The resonant X-ray reflectometry measurements described in Chapter 6 were performed at BESSY-II synchrotron, part of Helmholtz Zentrum Berlin in Adlershof, Germany. The undulator beamline UE46-PGM1 was chosen for these experiments because it has a high degree of linear polarization over the 400 eV to 500 eV incident energy range required to probe the Ti $L_{2,3}$-edges. In addition, UE46 has an ultra-high vacuum endstation (their so-called XUV diffractometer) that provides a stable environment in which to measure oxygen-sensitive rare earth titanate films, and the cryostats needed to do so across a wide temperature range.

2.4 Polarized Neutron Reflectometry

Many of the general principles already discussed for X-ray reflectometry measurements apply to polarized neutron reflectometry (PNR). In particular, neutron reflectometry data is refined to layer models using the same type of theory and recursive algorithms described in Section 2.2. However, there are several important points on which neutron and X-ray reflectometry differ, including: neutron scattering lengths, polarization measurement channels, and design of

the instrument endstation. These differences are elaborated upon within the sections below.

2.4.1 Neutron Scattering Lengths

Compared to X-rays, neutron scattering lengths possess a very different relationship with the size of the atom. This is illustrated in Fig. 2.6 which compares the neutron and average X-ray scattering length as a function of atomic number. It is this relationship that gives neutron scattering and reflectometry better sensitivity to light elements and better contrast between neighboring transition metals. This also means a given film heterostructure may have better or worse contrast between adjacent layers depending on the probe, and care should be taken when designing samples and experiments. In addition, whereas X-ray atomic scattering lengths have a strong energy-dependence (cf. Eq. 2.12), neutron scattering lengths are to first order independent of the neutron's energy and wavevector [77, 78]. As discussed below, this greatly simplifies the data refinement process relative to RXR.

There are two relevant interactions to consider in determining neutron scattering lengths, namely the neutron-nucleus interaction and the magnetic interaction between the neutron's moment and the total dipole moment of the atom's

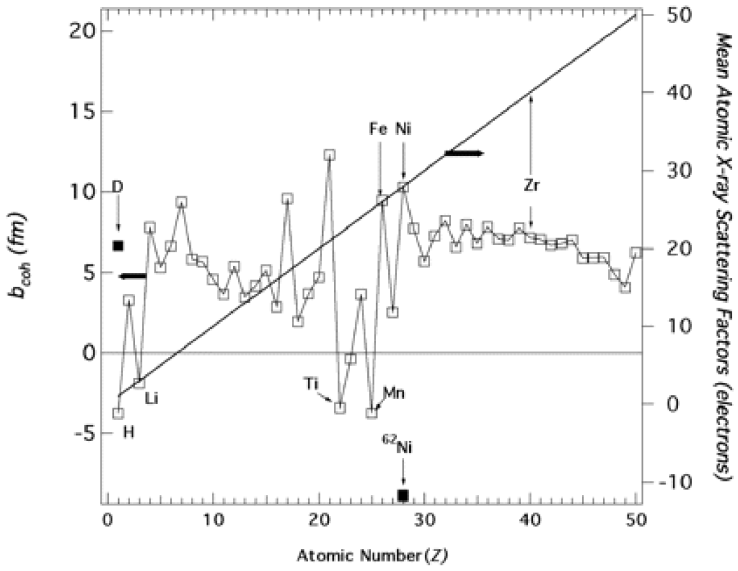

Figure 2.6: Comparison of neutron and average X-ray scattering lengths for different elements highlighting the areas where contrast differs between the two scattering probes. From Ref. [79]

electrons. These interactions lead to the nuclear scattering length and the magnetic scattering length, respectively. Other interaction potentials are at least two orders of magnitude weaker, and are generally neglected [80].

The coherent nuclear scattering length is the result of the strong nuclear force. While strong, it is also very short range, which results in scattering lengths on the same order as the much weaker but longer range magnetic interaction. The coherent nuclear scattering length b_i is related to the nuclear scattering potential V_N by:

$$V_N = \frac{2\pi\hbar^2}{m_n} \sum_i^M N_i b_i \tag{2.14}$$

where N_i is the number density of isotope i and the summation runs over all isotopes from i to M within a given material [81]. The expression can simplified by defining a scattering length density for layer j as

$$\rho_j = \sum_i^M N_i b_i. \tag{2.15}$$

The similarity between this equation and Eq. 2.5, which relates refractive index to atomic density and generic scattering length, is clear. In the case of the coherent nuclear scattering length, derivation of the precise relationship between scattering length and refractive index is simple and is accomplished by

plugging Eq. 2.14 into the time-independent Schrodinger equation within the assumption of elastic scattering [81]. The resulting relation is:

$$n^2 = 1 - \frac{4\pi \sum_i^M N_i b_i}{k_0^2} \tag{2.16}$$

in which k_0 is the component of the neutron's wave vector perpendicular to the z direction.

In theory, the nuclear scattering length is a complex value (i.e. $b_N = b_1 - ib_2$), but for most isotopes and materials, the neutron absorption cross-section is negligibly small and the imaginary term is ignored [82]. However, this is not true for Gd, and the treatment of neutron absorption during the modeling of PNR experiments on $GdTiO_3$ films is detailed in Section 3.3.

In practice, values for b_i, as well as those for incoherent nuclear scattering [83], are determined empirically and tabulated values can be found in Ref. [84]. These tabulated values are used as input into reflectometry models in order to refine experimental data.

Magnetic scattering lengths arising from dipolar interactions are generally treated as refined model parameters in reflectometry, except perhaps in the case of a few well-studied materials, for which some tabulated values are also available [81, 85]. Adding the magnetic scattering term to the scattering potential

in Eq. 2.14 results in the following expression:

$$V_T = \frac{2\pi\hbar^2}{m_n} \sum_i^M N_i b_i \mp \mu_n B \tag{2.17}$$

where B is is the magnetic induction inside a given layer of a sample and is related to an externally applied field H and internal magnetization M through the standard expression $B = \mu_0 H + M$. Rewritten in terms of refractive index and the magnetic scattering length b_{m_i}, the relation in Eq. 2.17 becomes:

$$n^2 = 1 - \frac{4\pi \sum_i^M N_i (b_i \pm b_{m_i})}{k_0^2}. \tag{2.18}$$

2.4.2 Polarization Scattering Channels

Because the nuclear and magnetic scattering lengths are similar in magnitude, neutrons are highly sensitive to magnetism within materials. However, it is important to note that the neutron is only sensitive to the component of B that is perpendicular to the scattering vector q. This arises from the dipolar nature of the magnetic scattering interaction [77].

Magnetic sensitivity can be improved by using a polarized neutron beam in which all of the neutrons have a uniform alignment of their magnetic moment

[86]. When both the incident and scattered neutron beams are polarized, there are four distinct polarization channels that can be measured. These channels are depicted in Fig. 2.7. The two on the left are known as the non-spin-flip channels and are sensitive to both nuclear scattering and magnetic components parallel to the neutron's moment. On the right are the two spin-flip channels, which are only sensitive to magnetic scattering and only the magnetic component perpendicular to the neutron's moment.

For a geometry with specular reflectivity scattering in the x-y plane, the scattering potential of these different channels can be summarized in matrix form:

$$\begin{bmatrix} V^{++} & V^{+-} \\ V^{-+} & V^{--} \end{bmatrix} = \frac{2\pi\hbar^2}{m_n} \begin{bmatrix} \rho_n + \rho_{mz} & \rho_{mx} - i\rho_{my} \\ \rho_{mx} + i\rho_{my} & \rho_n - \rho_{mz} \end{bmatrix} \tag{2.19}$$

where ρ_n and ρ_m are the nuclear and magnetic scattering length densities, respectively [81]. The second subscript on ρ_m indicates the directional component of the magnetization vector.

These polarization channel relations can be used to design clever experiments and extract information not possible from unpolarized neutron scattering. For example, measuring a peak in both the non-spin-flip and spin-flip channels can discriminate between features that are magnetic and structural in origin [87]. Comparing spin-flip and non-spin-flip channels can also be used to differ-

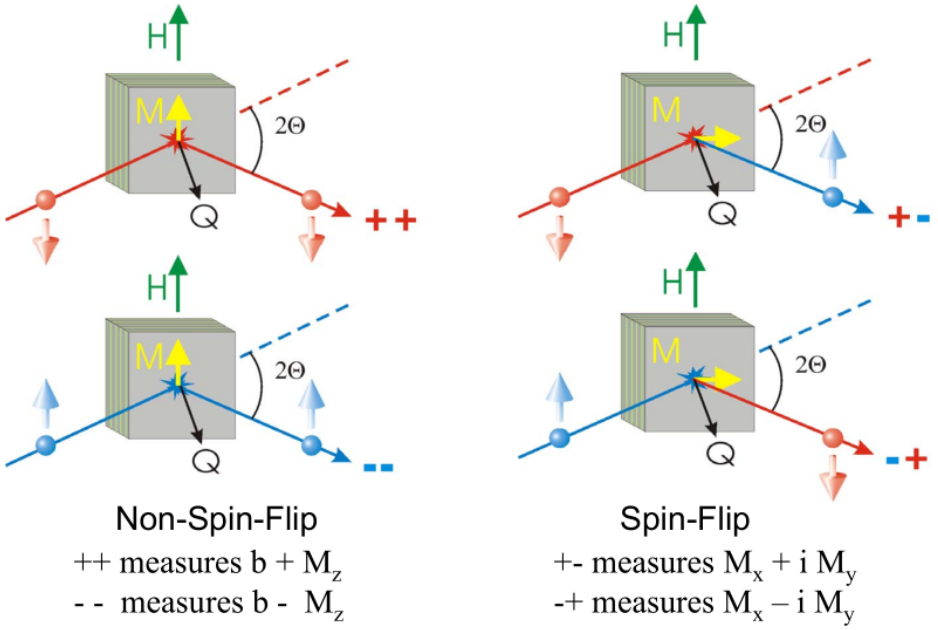

Figure 2.7: Schematics for the four polarized neutron scattering channels.

entiate longitudinal and transverse excitations in inelastic spectra [88].

2.4.3 Instrument and Experiment Specifications

All of the polarized neutron reflectometry measurements discussed in the experimental chapters below were taken at the NIST Center for Neutron Research on the Polarized Beam Reflectometer (PBR). This beamline uses a pyrolytic graphite monochromator to select out 4.75 $\mathring{A}$ neutrons from a moderated white beam of cold neutrons. An initial Fe/Si supermirrors selects out spin up neutrons and polarize the incident beam. The resulting flux after polarization is

on the order of 5,000 neutrons/cm^2/s. Mezei spin flippers before and after the sample allow the polarized beam to be precessed such that all four polarization channels can be measured. For our experiments, it was sufficient to collect data in the non-spin-flip channels and specular geometry only.

Samples were mounted in a closed-cycle He cryostat and placed inside either a $\mu_0 H = 0.7$ T or 3 T electromagnet. Field-dependent measurements were taken by zero-field cooling (ZFC) the sample from room temperature, saturating the sample under a maximum field, and then collecting PNR measurements at stepped intervals moving back towards zero field. Field-cooled (FC) and temperature dependent measurements were taken by cooling the sample from well above the Curie temperature ($T_C = 32$ K) down to 5 K under 0.7 T, and stepping temperature back towards T_C. All PNR measurements were collected with the applied external field oriented in the plane of the film.

2.5 Muon Spin Rotation/Relaxation/Resonance

The term μSR stands for muon spin rotation or relaxation or resonance, with all three of those R-variations constituting similar but distinct experimental techniques. All of the μSR variants rely on the muon as a very sensitive probe of magnetism in materials [89]. The muon is a radioactive lepton with a decay

lifetime of 2.2 μs, and is cousin to the more familiar electron. It has a mass of $\sim$200 m_e or equivalently $\sim$1/9 m_p, and carries either a positive or negative fundamental charge [90]. Typically, it is the positively charged variety that are used in experiments (because they are easier to produce) and therefore it often makes more sense to think of the muon as a light hydrogen ion, rather than a heavy electron.

General principles muon spin rotation and relaxation are discussed in detail below, but all of the μSR techniques share some common characteristics. For example, all μSR experiments are based upon individually implanting an ensemble spin-polarized muons in a material and measuring their decay. This is different than scattering in that the probing particles come to rest within the material being studied. The thermalization and arresting process of the muon occurs on a timescale of $\sim$10's of ps [91]. The muon's large magnetic moment, 3.18 μ_p, then becomes a probe of the local internal magnetic field at the muon's stopping site. For positive muons, the stopping site is generally a region of high electron density. However, this is not always the case and knowing the stopping site(s) of muons within a material can be critical to understanding the results of a μSR experiment [92].

After a few microseconds, the implanted muon decays into a positron (i.e. β particle) and a neutrino-anti-neutrino pair. The key feature that enables these

μSR techniques is the fact that when the positron is emitted, it is emitted preferentially in the direction of the muon's magnetic moment at the time of decay [90]. These positrons are then counted on detectors placed on various sides of the sample. The muons are implanted one-at-a-time and time stamped so that each decay event can be binned into a time histogram, $N(t)$. Then, by collecting an ensemble of millions of decay events, asymmetry in the positron counts between different detectors can be linked back to the direction and magnitude of static magnetic structures and/or the dynamics of magnetic fluctuations.

2.5.1 Types of μSR Experiments

This section provides further details for the two μSR variations used in the experiments in Chapter 5. The techniques can be performed with either high or low energy muons, and therefore have been described in general terms applicable to either.

In weak transverse field (wTF) μSR, or just transverse field μSR, the R stands for rotation. This technique is depicted in Fig. 2.8, and as the name implies, utilizes an applied field transverse or perpendicular to the muons' initial polarization. When the muons are implanted, they precess/rotate about the applied field H at the corresponding Larmor frequency $\omega = \gamma_\mu H$ where the muon's gy-

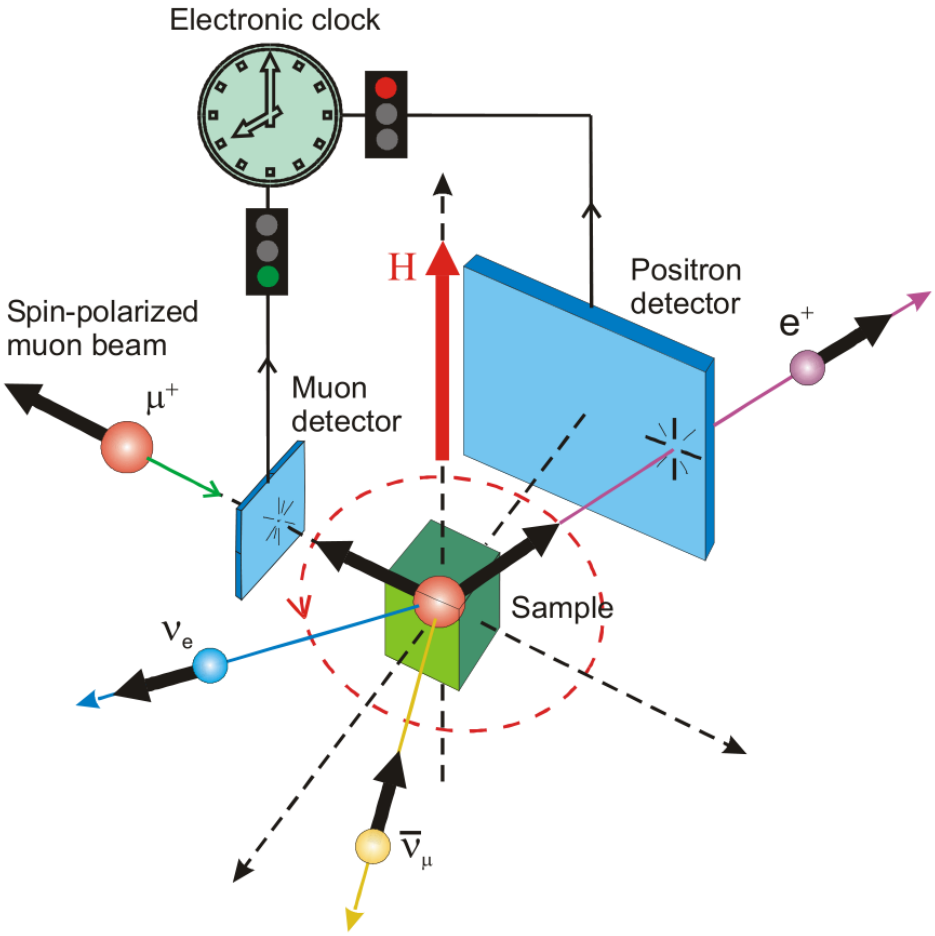

Figure 2.8: Weak transverse field μSR experimental geometry. From Ref. [93]

romagnetic ratio, γ_μ, is 2π·136 kHz mT^{-1} [90]. This frequency is imprinted on the time histogram, which has the form:

$$N(t) = N_0 e^{-t/\tau}[1 + A_0 P(t)] \tag{2.20}$$

where N_0 is a normalization prefactor proportional to the total number of muon decay events measured and the exponential term accounts for the muon's decay lifetime [91]. $A_0 P(t)$ is the asymmetry and $P(t)$ is the depolarization function that contains the essential magnetic physics of the material. The exact expression for $P(t)$ depends on both the type of μSR experiment and material under investigation, however in a wTF experiment, $P(t)$ often takes the form:

$$P(t) \propto e^{-\lambda t} cos(\omega t + \phi) \tag{2.21}$$

where we see the Larmor frequency from the applied field and a phase offset term. The exponential term in Eq. 2.21 describes the rate at which internal magnetism, whether static or dynamic, depolarizes the muons as they precess and causes a damping in the Larmor oscillation. In the experiments below, the wTF depolarization rate was tracked as a function of temperature to observe how magnetism within $SmTiO_3$ films and heterostructures evolved. The technique has also been useful in the study of field distributions in superconducting

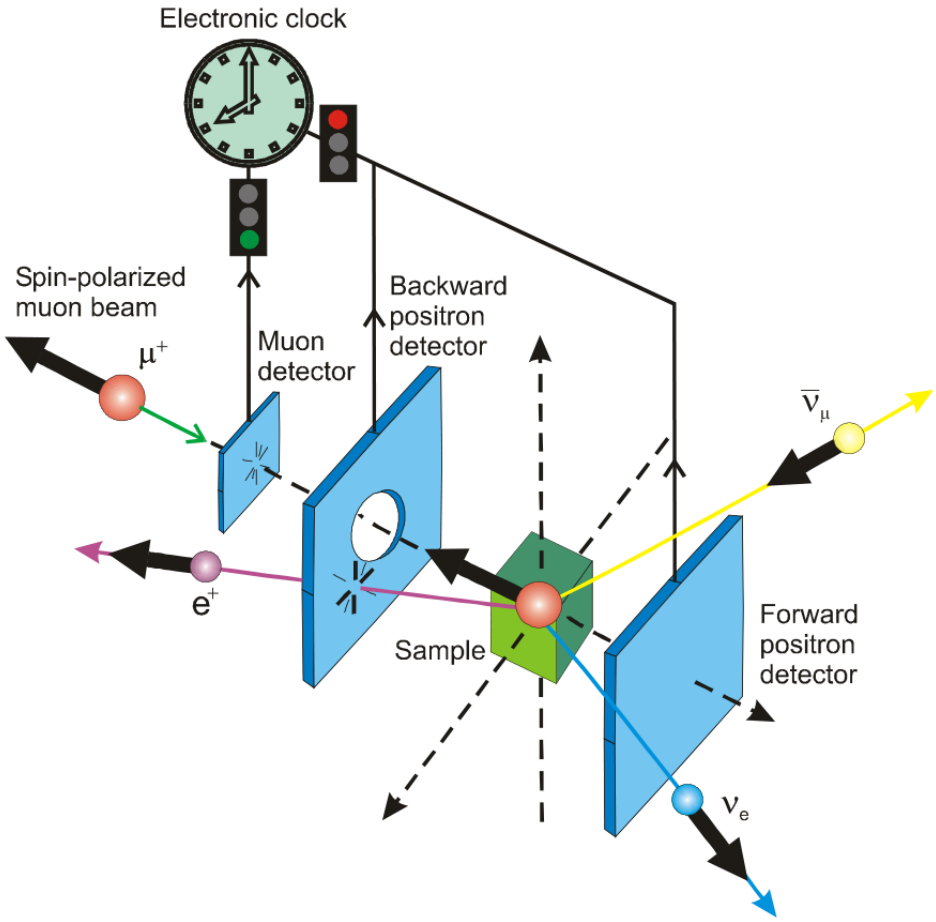

Figure 2.9: Zero field μSR experimental geometry. From Ref. [93]

vortex lattices [94] and measuring the Knight shift in heavy fermion compounds [95, 96].

When no external field is applied, the μSR technique is referred to as zero field (ZF) muon spin relaxation, a schematic of which is shown in Fig. 2.9. This experimental geometry is in most ways similar to the wTF geometry just described. At its core, ZF μSR still relies on counting an ensemble of individual

muon decay events and binning them to create a time histogram. However, because there is no applied field, there is often no oscillatory component to the depolarization function. The exception to this is when muons are implanted into a well-ordered single crystal with a non-collinear alignment of the muon polarization and magnetic moments. Then the internal field acts identically to the applied field in wTF experiments. Regardless, changes in the line shape of the asymmetry curve provide an extremely sensitive means of tracking the development of internal magnetic order. It has therefore been widely used in the fields of frustrated magnetism [97, 98] and spin glass/liquid systems [99, 100].

2.5.2 Low Energy Muons

Generating a beam of low energy muons begins by colliding a high-energy proton beam with a light element target such as carbon or beryllium [93]. This creates a large number of stationary pions on the surface of the target that subsequently decay into a beam of muons and neutrinos. These so-called surface muon beams are nearly 100% spin polarized anti-parallel to their momentum due to the parity violating pion decay process [101]. Because the pions all decay at rest, all of the surface muons are generated with the same 4.1 MeV kinetic energy. However, at this energy the typical implantation depth is on the

order of hundreds of microns. For nanometer thickness films, this results in all of the muons landing uselessly in the substrate.

To slow the muons down, they are passed through a moderator, much the same as in the generation of cold neutrons. In this case, the moderator consists of a nitrogen or argon film a few hundred nm thick condensed on a silver substrate at $\sim$10 K [91]. Unfortunately, only about 1 in 10,000 of the incident surface muons are slowed as they pass through the moderator resulting in a marked decrease in beam intensity relative to surface muon beamlines. In absolute numbers, this reduces the muon flux from roughly 10^8 s^{-1} to 10^4 s^{-1} and causes proportional increases in count times.

The muons that are moderated, so-called epithermal muons, have a residual kinetic energy of $\sim$15 eV. They are then re-accelerated to keV implantation energies by applying a voltage between the moderator and the sample stage [91]. At these energies, the muon implantation depth ranges from a few nanometers to a few hundred nanometers making them an ideal probe for many technological films. Moreover, the ability to easily tune the implantation energy between 0.5 keV and 30 keV means that buried layers and interfaces can be probed by moving the peak of the implanted muon distribution through the sample [102–104], allowing previously hidden phenomenon to be studied.

2.5.3 Instrument and Experiment Specifications

All μSR data were collected at the Low Energy Muon (LEM) spectrometer on the μE4 beamline at the Paul Scherrer Institute [105]. As of 2017, this is the only beamline in the world where low energy muons are available. For all measurements using this instrument, an implantation energy of 1.5 keV was used resulting in a mean implantation depth of $\sim$10 nm. At these low velocities the muon beam spot size is $\sim$10-15 mm in diameter, and in order to capture the majority of incident muons, each sample was comprised of four separate 1 cm x 1 cm films placed in a 2x2 grid. The samples were mounted in a flow cryostat and measured over the temperature range 5 K to 150 K. The initial muon polarization was in the plane of the sample. Data were collected both under a 10 mT magnetic field applied transverse to the initial muon polarization and in zero field. All SR data were analyzed and fit via Musrfit [106].

Chapter 3

Interface-driven Ferromagnetism within the Quantum Wells of a Rare Earth Titanate Superlattice

Here we present polarized neutron reflectometry measurements exploring thin film heterostructures comprised of a strongly correlated Mott state, $GdTiO_3$, embedded with $SrTiO_3$ quantum wells. Our results reveal that the net ferromagnetism inherent to the Mott $GdTiO_3$ matrix propagates into the nominally

[1]The contents of this chapter have substantially appeared in Reference 44: R. F. Need, B. J. Isaac, B. J. Kirby, J. A. Borchers, S. Stemmer, and S. D. Wilson, Interface-driven ferromagnetism within the quantum wells of a rare earth titanate superlattice, *Phys. Rev. Lett.* **117**, 037205 (2016). Copyright 2016 American Physical Society.

nonmagnetic $SrTiO_3$ quantum wells and tracks the magnetic order parameter of the host Mott insulating matrix. Beyond a well thickness of 5 SrO layers, the magnetic moment within the wells is dramatically suppressed, suggesting that quenched well magnetism comprises the likely origin of quantum critical magnetotransport in this thin film architecture. Our data demonstrate that the interplay between proximate exchange fields and polarity induced carrier densities can stabilize extended magnetic states within $SrTiO_3$ quantum wells.

3.1 Introduction

Interfaces between $RTiO_3$ (R=Gd, Sm, ...) and $SrTiO_3$ aggregate charge via a polar discontinuity between the differing valence states intrinsic to the rare earth and alkali earth layers of the two compounds [30]. In multilayer films, two sequential interfaces define a quantum well into which the polarization-induced carriers preferentially spread [30, 31]. This induced charge lives in a physically rich landscape; one where traversing between sufficiently thick layers also necessitates the relaxation of *d*-electron orbital polarization, long-range magnetic order, and strong on-site Coulomb interactions [107]. The thickness of the quantum well also defines a length scale for the mediation of interactions between polarity-induced carriers, which at sufficiently high densities have the

potential to drive electronic order [108]. Adding further complexity, structural symmetries (i.e. oxygen octahedral tilts) from the parent RTiO$_3$ can coherently propagate across the interface and into the well before relaxing beyond a critical thickness [33, 109, 110]. Ultimately, the combination of these effects may modify the bandwidth and electronic states manifest within the well, generating a parameter space not realizable in bulk form.

The interplay between polar interface charge and a proximate correlated state renders exotic transport phenomena in SmTiO$_3$/SrTiO$_3$ and GdTiO$_3$/SrTiO$_3$ heterostructures [28, 111]. The band insulator SrTiO$_3$, when embedded as thin quantum wells within Mott insulating GdTiO$_3$ barriers, exhibits metallic transport mediated via interface carriers [34]. A metal to insulator transition (MIT) emerges as the well thickness (defined by the number of SrO layers) decreases to 2 SrO layers and the corresponding well carrier density diverges [112]. Prior to this MIT, SrTiO$_3$ quantum wells with thicknesses of approximately 3 SrO layers display an unusual hysteresis in their low temperature longitudinal magnetoresistance—a state suggestive of domain switching and a field coupled electronic order parameter [39, 113].

Intriguingly, a divergent carrier mass was also observed near the stabilization of this order parameter, consistent with a quantum critical point (QCP) driven by the well carrier density/dimensionality [112]. However, little remains un-

derstood regarding the origins of this unusual phase behavior in $GdTiO_3/SrTiO_3$ heterostructures absent a direct resolution of the order parameter within the wells. Addressing this and searching for the presence of interface-induced magnetic order requires access to an experimental probe sensitive to magnetic polarization and capable of resolving its depth profile throughout a heterostructure—both of which are achievable via polarized neutron reflectometry (PNR) [114–116].

In this work, we present a PNR study exploring magnetic order within the quantum wells of $GdTiO_3/SrTiO_3$ heterostructures. Our data reveal the presence of magnetization induced within the $SrTiO_3$ wells below a critical well thickness of 5 SrO and demonstrate a novel realization of magnetic order induced within a nonmagnetic medium through the interplay between polarity induced charge density and proximity induced magnetic exchange. Furthermore, our results suggest that well magnetism represents the local order parameter whose suppression generates the divergent carrier mass reported in earlier magnetotransport studies [112].

3.2 X-ray Reflectivity Data and Models

A series of superlattice films containing a quintuple of 4 nm $GdTiO_3$ spacer layers separated by variable width $SrTiO_3$ quantum wells (2 SrO, 3 SrO, 5 SrO, and 10 SrO layers) were grown via molecular beam epitaxy, and PNR measurements were collected at the NIST Center for Neutron Research on the PBR reflectometer. PNR models of magnetism in $GdTiO_3/SrTiO_3$ heterostructures benefit from independent measurements of the films' structures in order to constrain the number of free-parameters. To achieve this, structural profiles were collected via room temperature x-ray reflectivity (XRR) measurements, and the XRR layer thicknesses and effective roughnesses were used as a fixed input in subsequent PNR models.

Figure 3.1 show the results of our XRR measurements and corresponding fits from the structural model of the films. The layer thicknesses and interfacial roughnesses were refined using Refl1D [117], a least squares regression program that uses an optical matrix formalism based upon the input layer model of the sample [82]. Structural models are denoted to the right of each data set. Excellent fits were obtained for all samples after allowing each layer thickness and scattering length density to vary independently while constraining the roughnesses of a given interface type (i.e. STO→GTO and GTO→STO) to be

identical within a given sample. Distinct interface types were allowed to be independent, including the surface and substrate interfacial roughnesses, and the value of a given interface type was allowed to vary between samples. The scattering length density of the top GTO layer was allowed to vary independently of the four buried layers in order to account for oxidation effects during the samples brief exposure to atmosphere during mounting.

It should be noted that while transmission electron microscopy (TEM) measurements of identical superlattice films show sharp interfaces [31, 33, 34] and a maximum chemical intermixing of one atomic layer [34], roughnesses measured by reflectivity are an average across the entire sample surface area, including effects from step edges across the underlying substrate. Hence, modeling quantum wells in the thin layer limit renders widths, roughnesses, and scattering length densities (SLDs) whose values become intrinsically coupled. As such, the refined roughness values in the thin well limit do not have an independent physical meaning and should not be compared to local probe measurements (e.g. TEM).

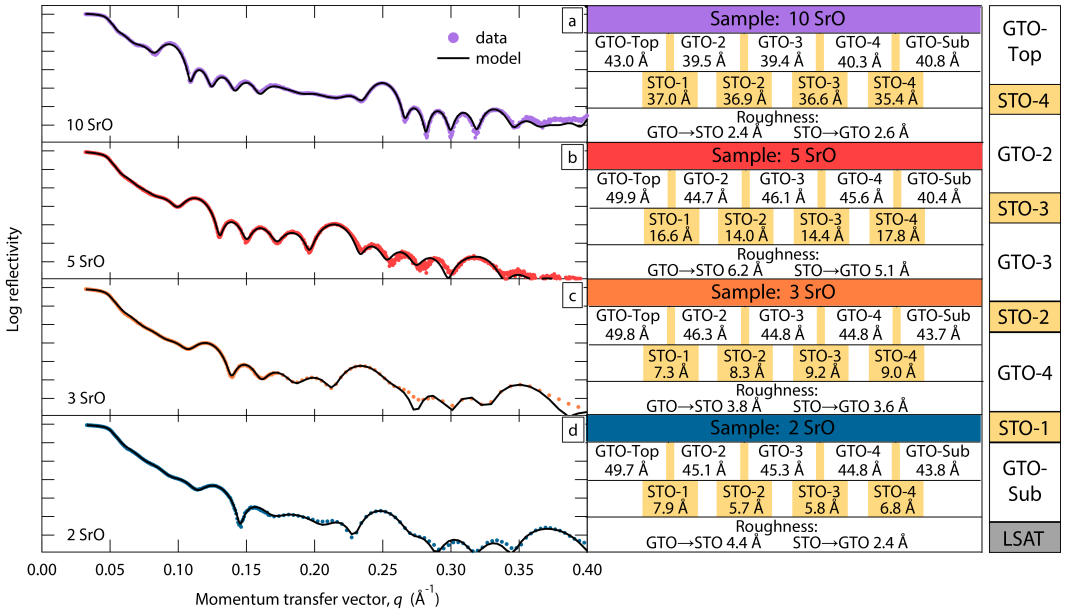

Figure 3.1: (a)-(d) Reflectivity as a function of momentum transfer for GTO/STO superlattice structures with quantum wells of thickness 10 SrO, 5 SrO, 3SrO, and 2 SrO layers respectively. Solid lines are fits to the data using the structural model located beside each panel. Layer thicknesses for all GTO and STO layers as well as roughnesses for each interface type are listed in this panel.

3.3 Reflectivity Modeling

The raw PNR data were reduced by first subtracting background scans from the signal, adjusting for polarization efficiencies, and correcting for the footprint of the incident beam. In non-absorbing samples, there is a sharp critical edge, below which the reflectivity is unity, and this footprint correction is simple. However, the large absorption cross section of Gd smears out this sharp critical edge in the samples investigated here. Therefore, the footprint correction was done by measuring the critical edge of a non-absorbing substrate (here, STO) that matched the dimensions of the LSAT substrates used in this study. The numerical footprint correction of the substrate was calculated and then applied to the GTO-containing samples. This method is only an approximation, but relatively accurate since the footprint correction is primarily a geometric consideration of how the beam's intensity changes at very small angles. To ensure that the empirical footprint correction used here did not strongly affect the results, small changes (5%) in the numerical correction were made and checked against the refined structure. Such changes made a negligible impact on the refined scattering length densities (SLDs) in the neutron layer models.

While the neutron SLD of a material can naively be calculated from first principles, for our analysis it was necessary to refine the STO and GTO SLDs.

The SLDs were allowed to vary from their nominal theoretical values for the following reasons: (1) gadolinium has a large wavelength-dependent neutron absorption cross section [118], which blurs the critical edge in the reflectivity profile and adds ambiguity to absolute profile normalization and (2) the large ratio of roughness to thickness in thinner STO layers means that their SLDs are intrinsically coupled to their other layer parameters (e.g. thickness, roughness, magnetic SLD).

For each sample, the chemical structure, determined via XRR, was used as input to help refine the neutron nuclear and magnetic SLD profiles in Refl1D. The neutron nuclear SLDs were determined via this low temperature (4 K) refinement. A competing model, where the nuclear SLDs were determined by refinement at high temperature (30 K), is compared below. Refining nuclear SLDs at low temperature was found to generate better fits to spin asymmetry data. Those values were then fixed and only magnetic SLDs were allowed to vary as a function of increasing temperature.

Within the Refl1D fitting software package, a number of regression algorithms are available. For the refinements in this work, the DREAM algorithm was used with the exception of the co-refinement method discussed in the alternative models section below. The DREAM algorithm is a Markov chain Monte Carlo method with a differential evolution step generator. It explores param-

eter space using a random walk similar to simulated annealing algorithms, always accepting a better point in phase space but also accepting a worse point depending on how much worse and at what point in the regression it is. Regressions were run using between 400-1000 steps depending on the number of free parameters, always using an initial population of 10 points in an epsilon ball distribution.

Interface between layers in Refl1D are allowed to vary smoothly via an error function profile, which blends the layers on either side of the interface. The roughness value itself is the 1- Gaussian roughness that moves the interface away from a simple step function. In the fitting algorithm, this layer transition is done using a Nevot-Croce formalism, which scales the index of refraction between two adjacent layers by exp(2knkn+12). The free parameter in the fit is the value for a given interface type (i.e. layer transition).

Error bars plotted in raw reflectometry data represent one standard deviation of the data. All errors of refined parameters, including magnetic moments, are reported as 95% confidence intervals calculated by a Monte Carlo simulated annealing algorithm in the Refl1D package as the moment range, which contains 95% of the accepted hops.

3.4 Polarized Neutron Reflectivity Data and Models

Figure 3.2 shows the results from low temperature ($T = 4$ K) PNR measurements on four superlattice samples collected under a field-cooled (FC) state ($\mu_0 H = 0.7$ T). Solid and empty symbols show non-spin flip data collected for specular reflectivity curves with the incident and scattered neutron polarizations oriented down (R^{--}) and up (R^{++}) relative to the sample field respectively, both of which encode information regarding the nuclear and magnetic SLD profiles of the film [119, 120]. While the overall oscillation of both curves is primarily reflective of the chemical profile of the film, splitting between these curves denotes a net, in-plane, magnetic polarization along the field direction where changes in magnetization between layers produce a difference in the ($R^{++} - R^{--}$) cross section. Chemical and magnetic scattering profiles can be modeled simultaneously via an optical matrix formalism [82], and the resulting fits are plotted in Fig. 3.2. Gaps in the data sets (i.e. $q = 0.055 - 0.080$ $\mathring{A}^{-1}$ in Figs. 3.2 (b) and (b)) are due to limited measurement time and prioritization of q ranges where $SrTiO_3$ features are most salient.

The parameters summarizing the modeled films' depth profiles at 4 K and 30 K are plotted in Fig. 3.3. Chemical contrast varies as expected between $GdTiO_3$

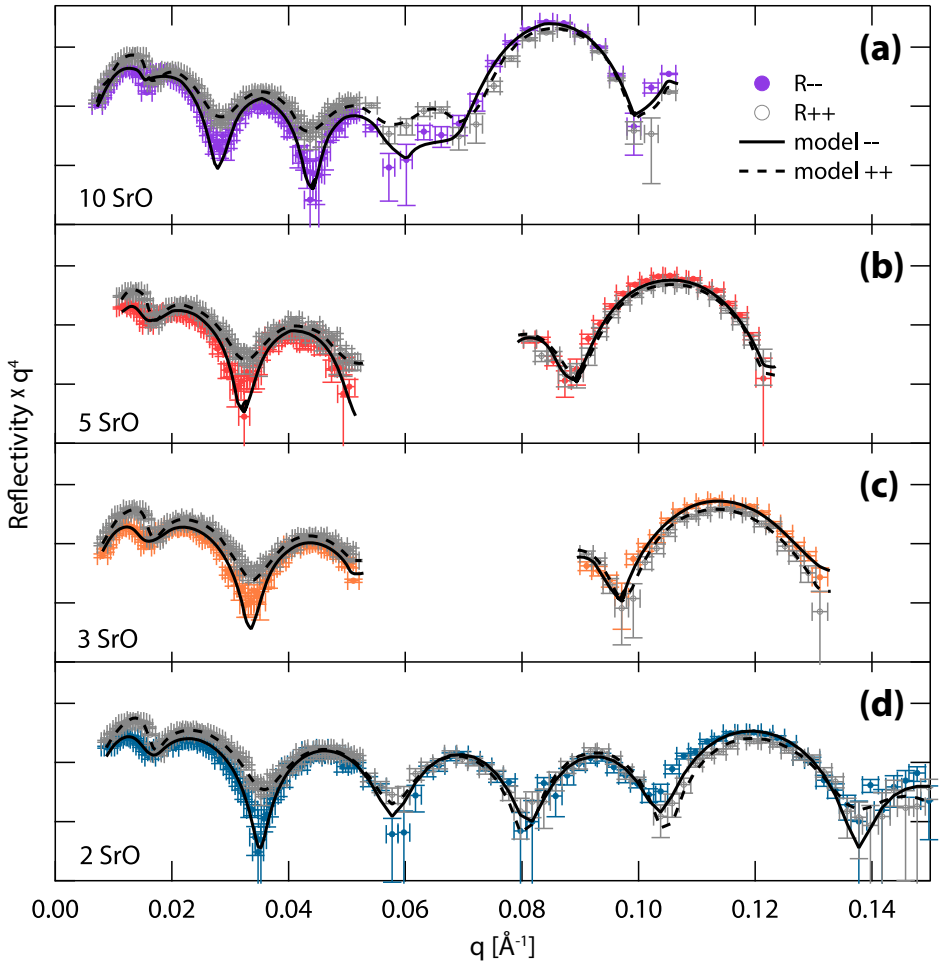

Figure 3.2: (a)-(d) Neutron reflectivity as a function of momentum transfer for $GdTiO_3/SrTiO_3/GdTiO_3$ superlattice structures with quantum wells of thickness 10 SrO, 5 SrO, 3SrO, and 2 SrO layers respectively. Open gray symbols denote the R^{++} cross section and closed color symbols denote R^{--}. Dashed lines (R^{++}) and solid lines (R^{--}) indicate the fits resulting from structural and magnetic models of the data.

and $SrTiO_3$ layers with the topmost $GdTiO_3$ layer distinct from the buried layers due to brief periods of exposure to atmosphere. The effective roughnesses of the $GdTiO_3 \rightarrow SrTiO_3$ and $SrTiO_3 \rightarrow GdTiO_3$ interfaces span the thicknesses of the wells in the 2 SrO and 3 SrO samples; however the wells in the 5 SrO and 10 SrO samples are able to reach their nominal bulk SLDs and increasingly decouple from neighboring layers. To better isolate magnetism in the wells, nuclear SLDs were refined at low temperature and then fixed; only the magnetic neutron SLDs were allowed to vary as a function of temperature.

The magnetic contrast between neighboring layers at 4 K notably does not follow the expected contrast between ferrimagnetic and nonmagnetic layers. Instead, a finite magnetization persists across the $SrTiO_3$ wells for the 2 SrO, 3 SrO, and 5 SrO samples. To better demonstrate this, the magnetic components of the total scattering profiles are isolated by plotting the spin asymmetries, $(R^{++} - R^{--})/(R^{++} + R^{--})$ in Fig. 3.4. Here, the low-q portion of the asymmetry is dominated by the ferrimagnetism of $GdTiO_3$ spacers comprising the bulk of the sample. At higher q values, the scattering is more sensitive to magnetism associated with the $SrTiO_3$ quantum wells, particularly at a thickness-dependent Bragg position of the bilayer repeat. Modeling the combination of these two extremes allows for the magnetic contrast between the layers to be directly refined.

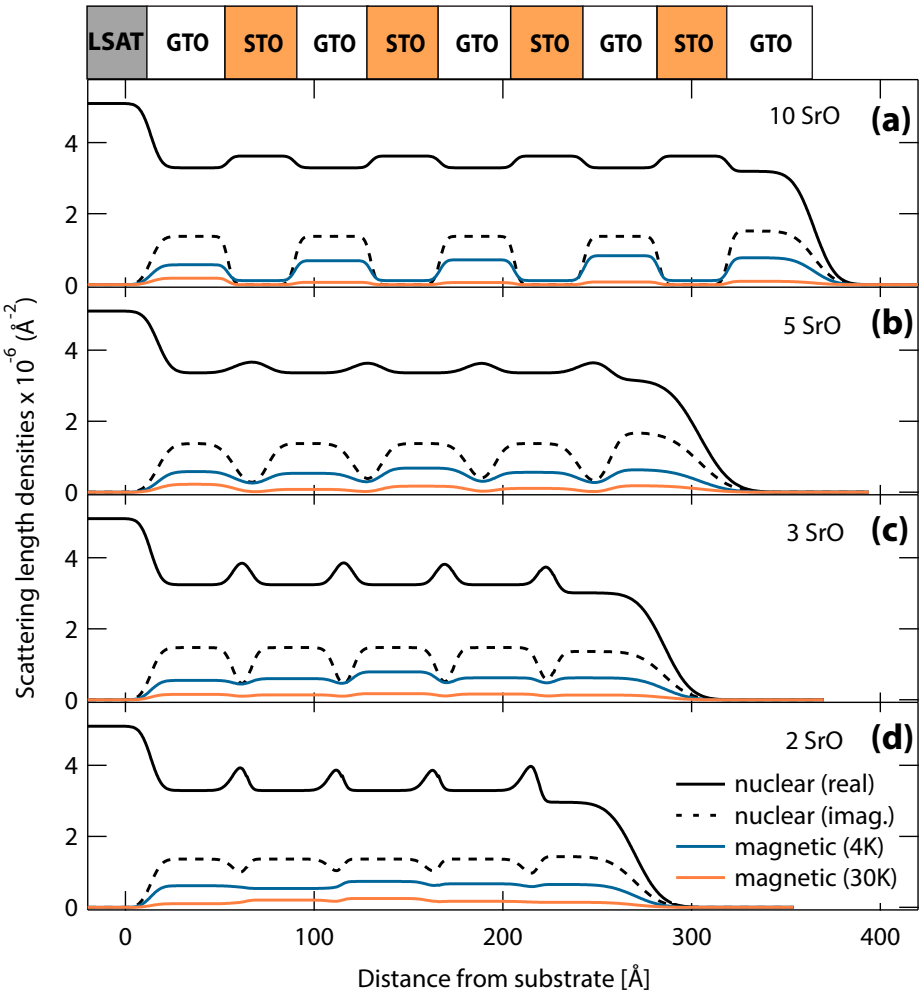

Figure 3.3: Nuclear and magnetic depth profiles of $GdTiO_3/SrTiO_3$ superlattice films. SLDs as a function of film depth corresponding to the structural and magnetic models of PNR data for superlattice films with (a) 10 SrO, (b) 5 SrO, (c) 3 SrO, and (d) 2 SrO layers thick $SrTiO_3$ wells. Solid and dashed black lines correspond to the real and imaginary components of nuclear scattering density profile, while the blue and orange lines correspond to the magnetization fits at $T = 4$ K and 30 K.

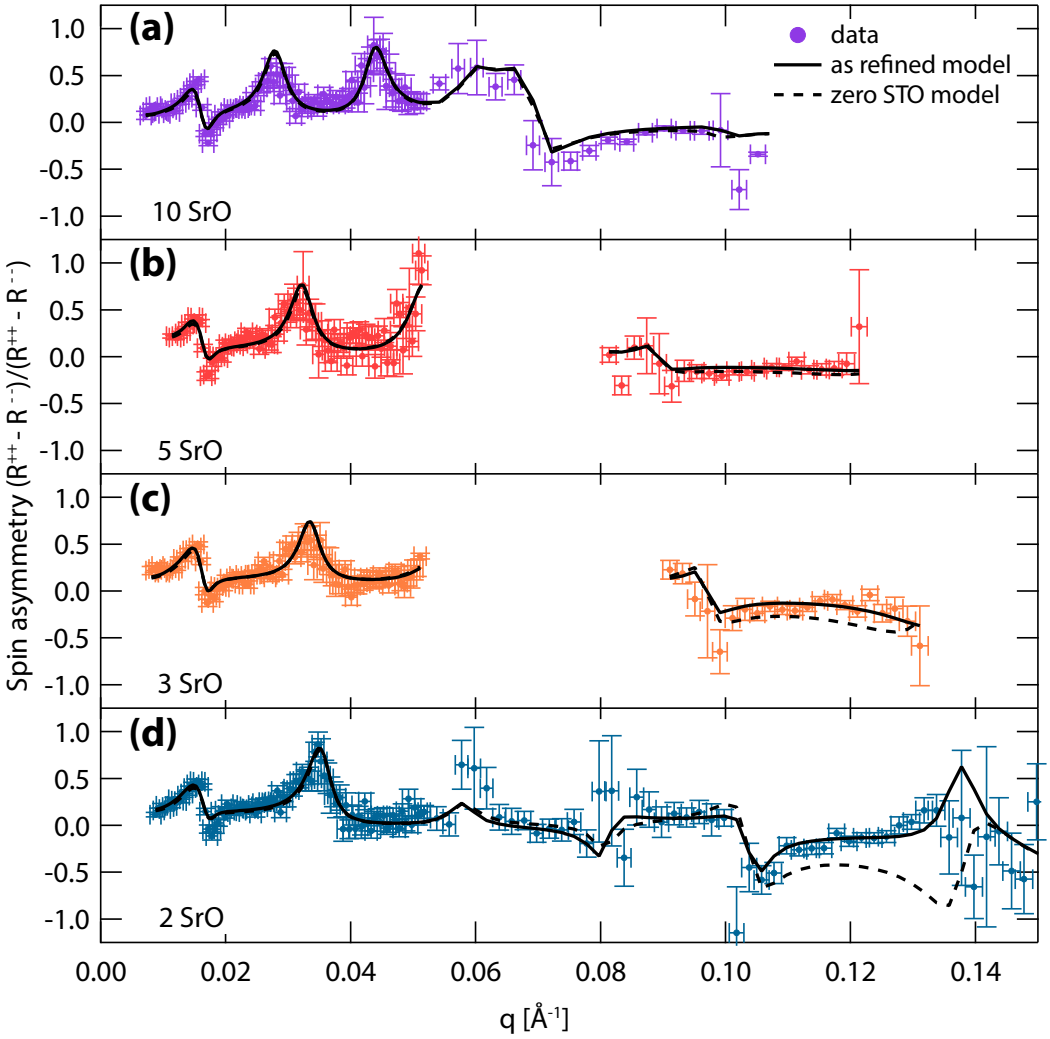

Figure 3.4: Spin asymmetry at T = 4 K in $GdTiO_3/SrTiO_3$ superlattice films with (a) 10 SrO, (b) 5 SrO, (c) 3 SrO, and (d) 2 SrO layers thick $SrTiO_3$ wells. Solid lines represent the refined models to the data, and the dashed lines represent a model constraining zero magnetization contribution from $SrTiO_3$.

A qualitative sense of magnetism inside the thinnest 2 SrO wells is apparent via inspection of Figs. 3.2 (d), 3.3 (d), and 3.4 (d). Fig. 3.2 (d) illustrates the Bragg peak and the corresponding R^{++} and R^{--} cross sections associated with the bilayer repeat at $q \approx 0.12\mathring{A}^{-1}$. The model profiles corresponding to these reflectivity curves plotted in Fig. 2 (d) show sharp contrast between the nuclear SLDs; however nearly negligible contrast is apparent within the magnetizations between layers. In order to account for this diminished magnetic contrast, the presence of magnetism within the $SrTiO_3$ wells is illustrated in Fig. 3.4 (d). Here a model of spin asymmetry allowing magnetized $SrTiO_3$ wells is compared with one forcing the magnetization contribution from $SrTiO_3$ to zero in the well center. The freely refined model, placing finite magnetization in the $SrTiO_3$ wells, matches the data substantially better in the high q limit where sensitivity to $SrTiO_3$ is maximal. Stated in other words, spin asymmetry values near zero in the region of the Bragg peak necessitate a model with magnetism in the $SrTiO_3$ wells in order to produce the muted magnetic scattering contrast in the data.

3.5 Alternative PNR Models

Common Layer Thicknesses, Unique Layer Roughnesses: In the XRR data and analysis section, it was noted that our structural model constrained each unique

interface type (i.e. GTO-STO and STO-GTO) to be uniform at each occurrence of that interface, while each layers thickness was allowed to be unique. This was primarily done to reduce the number of free parameters in the model, without which, the algorithm has difficulty converging. A similar reduction in the number of free parameters can be achieved by a reverse model, in which each type of layer has a constrained thickness for each occurrence of that layer and all interfaces are allowed to be unique.

To address this, it is important to begin with a reminder that in this regime where layer thicknesses and roughnesses are nearly equal, convolution of roughnesses and well thicknesses results in the loss of the common physical meaning of these parameters and precludes testing this in a meaningful way. Nevertheless, we did try fits using the fixed layer thicknesses and varying roughnesses. The results were not strongly or systematically different than the current model, as such there is no reason to prefer one to the other. Moreover, with the loss of physical meaning of the two parameters in the thin well limit, it is perhaps more correct to think of these two models as two different descriptions of the same profile than two unique models.

Refining Neutron Nuclear SLDs at 30K: As noted above, the nuclear neutron SLDs were refined together with the magnetic neutron SLDs using the low temperature (4 K) data. Then the nuclear SLDs were fixed for a given sample and

only the magnetic SLDs were allowed to vary as a function of temperature. It turns out that this low to high method generates better fits, particularly to the spin asymmetry, than the reverse high to low case where nuclear SLDs are refined at 30 K. This is demonstrated in Fig. 3.5.

Although it may seem counter intuitive to refine nuclear SLDs at low temperature where magnetism is largest, it is beneficial to utilize the magnetization density as an added contrast when determining the structure. The magnetization can be thought of as additional information that reduces the number of possible models that can accurately fit all of the data. This is analogous to the benefit provided by scanning a larger q range.

Co-refinement of XRR and PNR: Another alternative method of refining the data presented in this study would be to co-refine the XRR and PNR data. In principle this is a very correct approach. However, as shown in Fig. 3.6 below, this tends to fail in practice. Figure 3.6 compares the results of sequential refinement of the XRR and PNR data utilized in the main text of this study to the co-refinement method just described. In the case of the 10 SrO sample, where STO thicknesses are large and decoupled from interface roughness or SLD, the results show very little difference between the two refinements methods. However, as the STO thickness is decreased, the magnitude of the differences between the refinement methods increases culminating in the very poor spin asymmetry fit

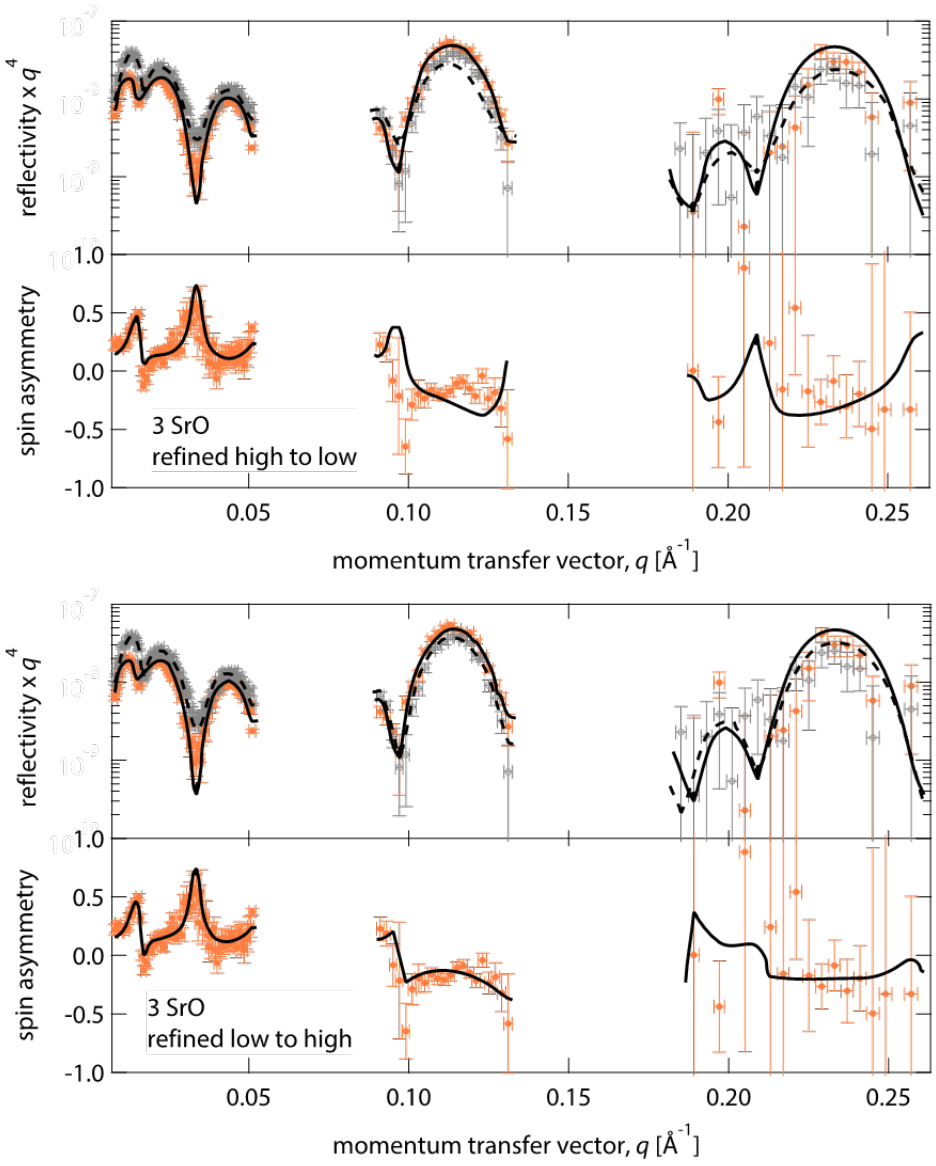

Figure 3.5: PNR data and refinements of the 3 SrO superlattice film using the high to low and low to high refinement methods. The top panel shows the reflectivity adjusted for Fresnel decay (i.e. Rq^4). The bottom panel shows the spin asymmetry data (in solid orange circles) and the fit (as a solid black line).

seen for the 2 SrO sample.

This trend is due to the large difference in the relative error bars between the XRR and PNR data and the manner in which the refinement algorithm fits the model to the data set. In both XRR and PNR, the error is proportional to the number of detector counts. The XRR counts are many orders of magnitude higher than the PNR data resulting in much smaller relative error for the XRR data. As a result, the fitting algorithm preferentially fits the model to the XRR data in order to minimize the overall χ^2 goodness of fit. However, this preferential fit to the XRR data comes at the expense of the fit to the neutron data, which is most evident in the spin asymmetry of the 2 SrO sample. Therefore, better fits of the magnetization profile can be obtained by refining the PNR independently of the XRR data such that there is no mismatch in the magnitude of the errors involved.

3.6 $GdTiO_3$ Control Film Measurements

In order to corroborate the refined magnetization of the GdTiO3 layers in superlattice samples, a control film consisting of 5 nm of GTO on LSAT was measured by PNR at 4 and 30 K under identical field cooled conditions as the superlattice films. The low temperature (4 K) data, spin asymmetry, and refined

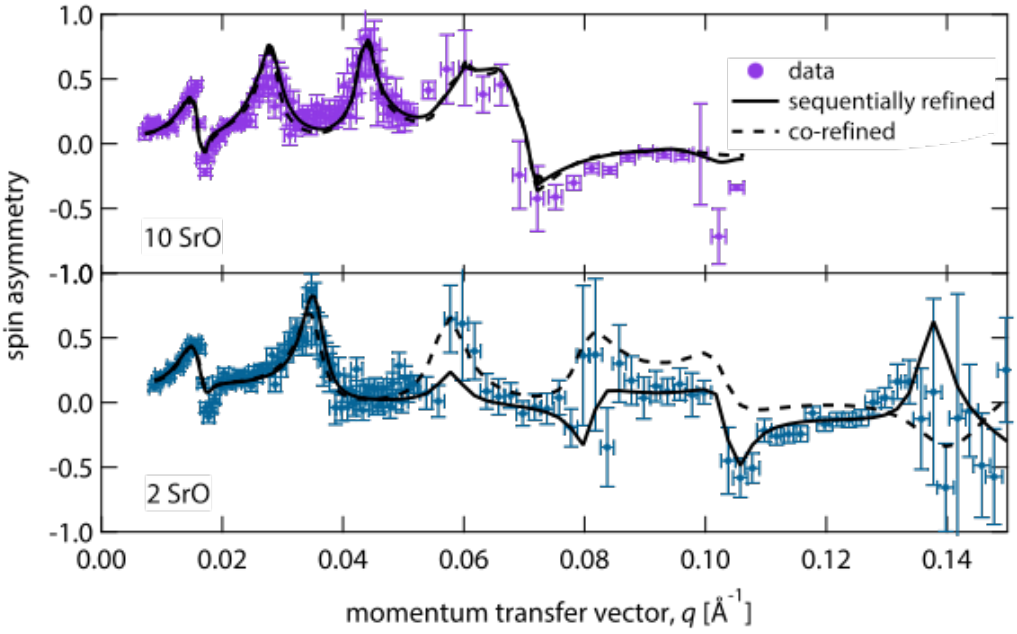

Figure 3.6: PNR spin asymmetry data and refinements for the 10 SrO (top panel) and 2 SrO (bottom panel) superlattice films comparing sequential and co-refined methods. For each sample, the spin asymmetry data is shown in solid colored circles, the fit from sequential refinement (included in the main text) as a solid black line, and the fit to from co-refinement as a dotted black line.

model are displayed in Figs. 3.7 (a), (b), and (c), respectively. The roughnesses at both the LSAT and air interfaces, 5 and 10 , respectively, are in good agreement with average values from the superlattices. Furthermore, the magnetization in the center of the GTO layer is within error of the values refined for the GTO layers in the superlattices samples.

3.7 Magnetization Summary and the Effect of Quantum Well Thickness

The average magnetization values in each superlattice (collected at the layer center values in model profiles) are plotted as a function of temperature for the four buried $GdTiO_3$ and $SrTiO_3$ layers in Figs. 4 (a) and (b), respectively. Looking first at the spacer $GdTiO_3$ layers, ordered moment values show a temperature dependence tracking that of the ferrimagnetic order parameter observed in bulk crystals and relaxed films [21, 27, 32]. The small amount of scatter in the data arises from ambiguities in the absolute normalization of the reflectivity data, and taken as an average, the moments observed in the $GdTiO_3$ layers are 1.42 $\pm$ 0.20 μ_B/f.u. at 4 K and 0.33 $\pm$ 0.11 μ_B/f.u. at 30 K (f.u. = formula unit). In order to confirm that the $GdTiO_3$ magnetization is independent

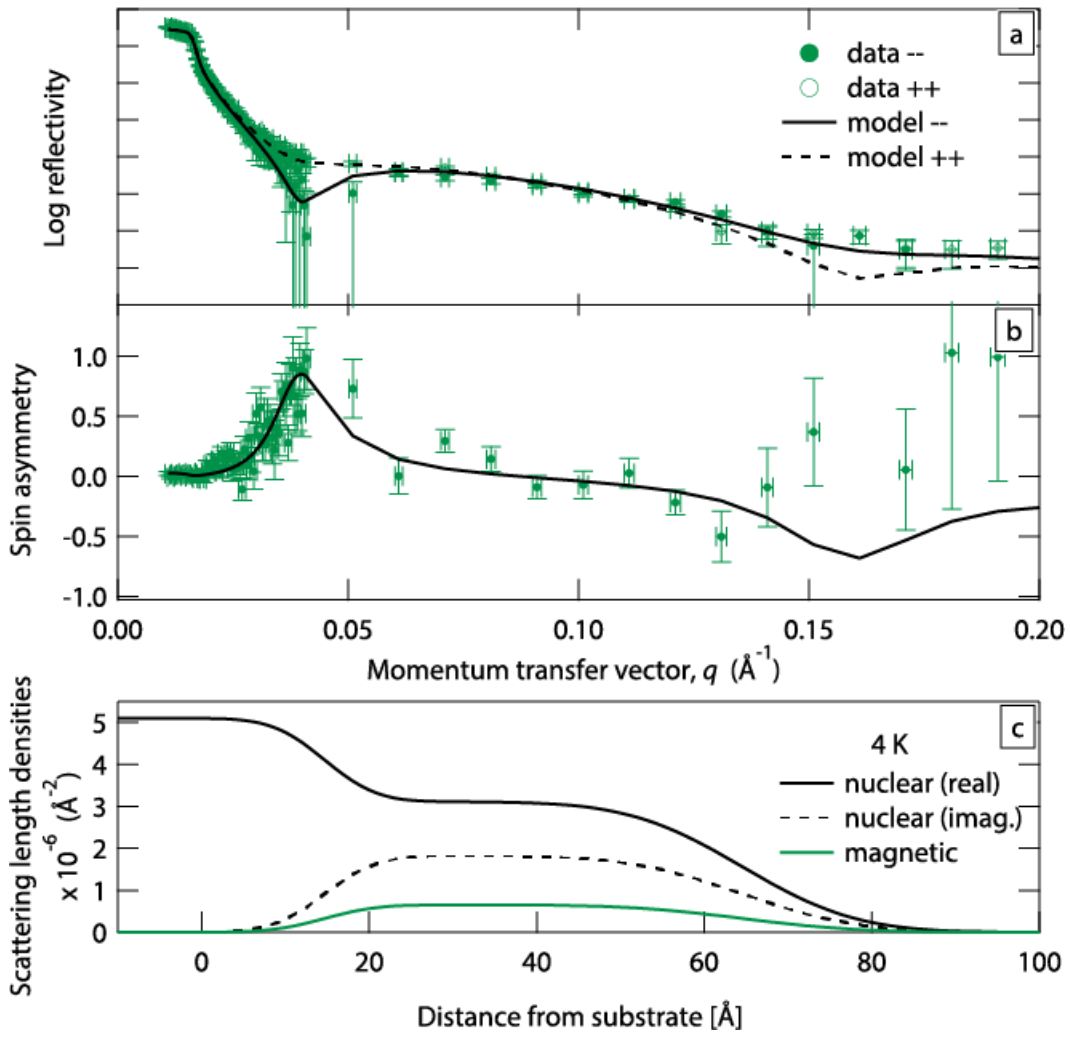

Figure 3.7: (a) Reduced and normalized PNR data of a 5 nm GTO control film. (b) Spin asymmetry of the 4 K PNR data set. In both (a) and (b) open and closed circles represent the data while lines represent best fits from the refined model. (c) Refined layer model of the GTO control film. Black solid and dashed lines indicate the real and imaginary parts of the nuclear SLD, respectively. Green line displays the neutron magnetic SLD.

of the well thicknesses, a separate film comprised of only a single 5 nm layer of $GdTiO_3$ was measured under identical conditions (i.e. $\mu_0 H = 0.7$ T FC). The magnetization was refined to be 1.43 $\pm$ 0.13 and 0.24 $\pm$ 0.19 μ_B/f.u. at 4 K and 30 K, respectively—within error of the superlattice values. The agreement between the magnetic properties of the isolated thin film and $GdTiO_3$ spacer layers confirms that the $GdTiO_3$ spacer layers are thick enough to decouple from the $SrTiO_3$ quantum wells. This allows for added confidence in isolating the evolution of $SrTiO_3$ magnetism under varying well thickness.

The magnetization values inherent to the $SrTiO_3$ layers are plotted in Fig. 4 (b). For the three thinnest wells (2 SrO, 3 SrO, and 5 SrO), $SrTiO_3$ layers exhibit a finite magnetization whose temperature dependence seemingly tracks that of the polarizing $GdTiO_3$ spacer layers. The saturated (4 K) moments in the $SrTiO_3$ layers increase as the well thicknesses are decreased and the electron gas at the interfaces is further confined; eventually reaching a peak value 1.11 $\pm$ 0.11 μ_B/f.u. in the center of the 2 SrO wells. This value is within error of the 1 μ_B/Ti naively expected for fully polarized $S = 1/2$ Ti^{3+} moments. In contrast, the thickest 10 SrO sample refines to show a nearly vanishing $SrTiO_3$ magnetic moment within resolution (0.25 μ_B/f.u. at 4 K). Here the experimental sensitivity is effectively constrained by the uncertainty in the magnetization of the $GdTiO_3$ layers at this temperature. This is illustrated in Fig. 3(a) where

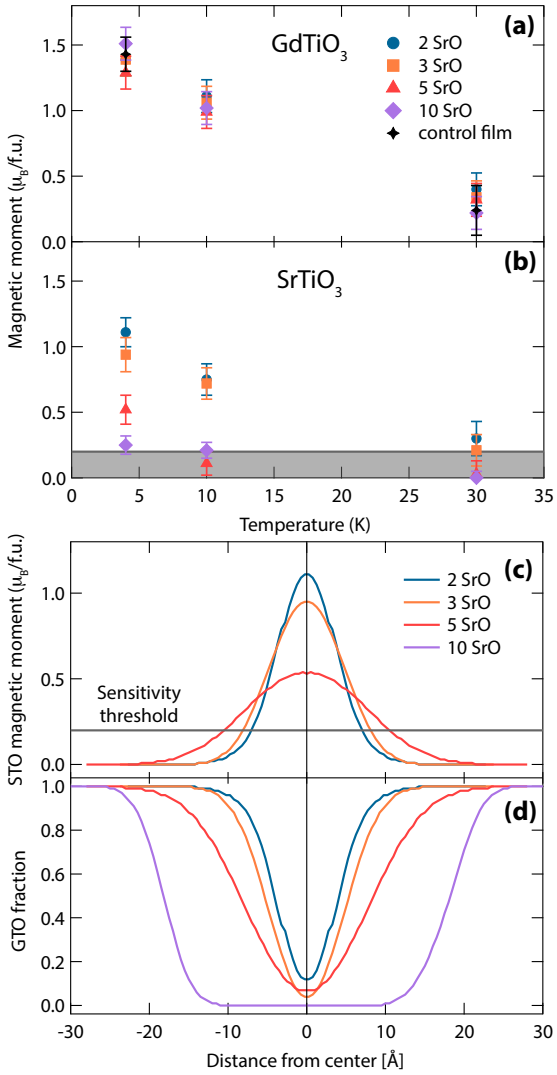

Figure 3.8: (a) Magnetic moment per formula unit in $GdTiO_3$ layers. (b) Magnetic moment per formula unit observed within $SrTiO_3$ layers. Shaded region denotes approximate experimental sensitivity to $SrTiO_3$ moments. (c) Effective magnetization profiles for quantum wells after removing convolved $GdTiO_3$ contributions. (d) The relative fraction of $GdTiO_3$ convolved within the quantum wells as a function of distance from the well center.

models of the spin asymmetry containing magnetic versus nonmagnetic $SrTiO_3$ layers are identical.

In order to parameterize the magnetism native to the quantum wells, the contribution of $GdTiO_3$ moments to the apparent magnetization of the $SrTiO_3$ wells can be largely accounted for and removed [115]. Specifically, the concentration of $GdTiO_3$ apparent within the wells can be calculated from the real parts of the nuclear SLD profiles by interpolating between pure $GdTiO_3$ and pure $SrTiO_3$. This average convolution between layers is plotted in Fig. 4 (d) and represents the fraction of $GdTiO_3$ convolved into the $SrTiO_3$ layers as a function of displacement from the center of the wells. In the thickest 10 SrO wells, the $GdTiO_3$ fraction drops to zero throughout the majority of the well, whereas in the thinnest 2 SrO wells the apparent roughness mixes in a substantial fraction of $GdTiO_3$ close to the well center. This effective profile of $GdTiO_3$ within the wells can then be multiplied by the magnetization inherent to these spacer layers, yielding a maximum magnetic contribution from $GdTiO_3$ throughout the depth of the well. The $GdTiO_3$ contribution is then subtracted from the total refined $SrTiO_3$ magnetization profile (c.f. Fig. 2), and the result is plotted in Fig. 4 (c). This subtracted profile gives an average sense of how much of the refined moment is attributable to electrons induced within the well by the polar discontinuities.

The intrinsic ferromagnetism within the $SrTiO_3$ layers necessarily originates via the high-density two-dimensional electron gas (2DEG) induced at the interfaces. Half of an electron per area unit cell is contributed to each well via the top and the bottom interfaces, yielding a total of one electron per well [30]. Therefore the integrated polarized moment in each well should be a constant value of 1 μ_B regardless of the well thickness. From our models, we calculate total integrated moments in the wells to be 2.75 μ_B, 2.83 μ_B, and 2.60 μ_B/well, for the 2, 3, and 5 SrO samples, respectively. Although these values are consistent with a picture of a constant integral moment, their magnitude likely reflects an inherent overestimation born by modeling the magnetization density as peaked in the center of the $SrTiO_3$ wells.

While *f-d* hybridization effects may play a role in polarizing some fraction of electrons directly at the interfaces, the majority of induced electrons are known to substantially delocalize into the volume of the $SrTiO_3$ wells and suggest a more extended exchange mechanism [31]. The density of interface-induced carriers nominally decays by 50% over approximately 1 nm into the bulk of $SrTiO_3$ [39], and the average 1.8 nm thick wells of the 5 SrO sample are consistent with a threshold where the overlap between interface states becomes appreciable. Moving substantially above this thickness corresponds to distances where the extended 2DEGs stabilized at each polar interface no longer sufficiently overlap

and support the continuation of the exchange field across the well. We stress here however that our PNR measurements are unable to comment on presence of magnetic texture within the wells themselves, rather, in the thin well limit, the resolution of our data only permits effective models of uniformly magnetized wells. Despite this, the disappearance of $SrTiO_3$ magnetism with increasing well thickness connects ferromagnetic spin correlations in the $SrTiO_3$ wells with the local order parameter destabilized at the quantum critical point in this system [112].

3.8 Conclusions

The temperature dependence of the ordered moments within the wells tracks that of the ferrimagnetism within $GdTiO_3$ spacing layers, suggesting that the molecular field of neighboring $GdTiO_3$ polarizes moments within the wells. The induced phase is therefore distinct from the hysteretic response identified in prior magnetoresistance measurements with a lower characteristic temperature ($T_c \approx 5$ K). Either a nontrivial field dependence of the order induced within the wells or an alternative order parameter, such as orbital order, should be invoked to explain this low temperature state. Rather, our key finding is a striking realization of interface-induced magnetic polarization across nominally

nonmagnetic $SrTiO_3$ quantum wells nearly 2 nm thick embedded within a Mott insulating $GdTiO_3$ matrix.

Chapter 4

Octahedral Tilt Independent Magnetism in Confined $GdTiO_3$ Films

Polarized neutron reflectometry measurements are presented exploring the evolution of ferrimagnetism in $GdTiO_3$ films as they are confined between $SrTiO_3$ layers of variable thicknesses. As $GdTiO_3$ films approach the thin layer limit and are confined within a substantially thicker $SrTiO_3$ matrix, the TiO_6 octahedral tilts endemic to $GdTiO_3$ coherently relax toward the undistorted, cubic phase of $SrTiO_3$. Our measurements reveal that the ferrimagnetic state within

the $GdTiO_3$ layers survives nearly unperturbed as the TiO_6 octahedral tilts in the $GdTiO_3$ layers are suppressed. Furthermore, our data suggest that a magnetic dead layer develops within the $GdTiO_3$ layer at each $GdTiO_3$/ $SrTiO_3$ interface. The ferrimagnetic moment inherent to the core $GdTiO_3$ layers is negligibly (in models with dead layers) or only weakly (in models without dead layers) impacted as the octahedral tilt angles are suppressed by more than 50% and the t_{2g} bandwidth is dramatically renormalized.

4.1 Introduction

Complex oxide thin films and interfaces continue to constitute an exciting frontier in condensed matter physics where layer thickness, interfacial strain, and chemistry can be used to tune competing interactions and generate emergent ground states [107, 121]. This tunability, when combined with strong electron-electron correlations in these systems, results in a range of electronic and magnetic ground states unique from their bulk components such as interfacial ferromagnetism [44, 122], metal-to-insulator transitions [34], and voltage-tunable superconductivity [123, 124].

Within the realm of engineered heterostructures, ABO_3 perovskites have received considerable attention owing in part to the wide range of possible

chemistries and the atomic precision with which multilayer films can be fabricated. For many bulk perovskites, the A-site cation is too small for the perovskite structure to retain cubic ($Pm\bar{3}m$) symmetry. The consequence is a cooperative distortion (i.e. tilts and rotations) of the BO_6 octahedron that may take one of multiple possible patterns [125] and is proportional in magnitude to the Goldschmidt tolerance factor [126]. As the radius of the A-site cation decreases, the structural distortions increase leading to movement of the B-O-B bond angle away from 180° and a corresponding decrease in orbital overlap affecting both electronic and magnetic properties [15, 127, 128].

These cooperative distortions are altered from their bulk patterns near a heterointerface of two dissimilar perovskite films (i.e. ABO_3/$A'B'O_3$) [129]. Which octahedral network distorts and the degree to which it distorts can be intentionally engineered by the choice layer thicknesses and interfacial strain to generate functionality not possible in either of the bulk components [110, 130]. For example, interfacial octahedral engineering has been successfully employed to enhance ferroelectric polarization in $CaTiO_3$/$BiFeO_3$ superlattices [131], magnetism in $LaMnO_3$/$SrTiO_3$ superlattices [132], and to manipulate quantum criticality in $SmTiO_3$/$SrTiO_3$ and $GdTiO_3$/$SrTiO_3$ quantum wells [28, 112].

Particularly fascinating phenomena appear at engineered $GdTiO_3$/$SrTiO_3$ interfaces. In the bulk, the Mott insulator $GdTiO_3$ (GTO) possesses $GdFeO_3$-type

distortions in its TiO_6 octahedra network while the band insulator $SrTiO_3$ (STO) possesses the undistorted parent cubic structure at room temperature [16, 33]. By interfacing thin epitaxial layers of GTO and STO, the octahedral tilts inherent to each layer can be coherently controlled with dramatic effects on the free carriers generated by the polar discontinuity at the interface. For instance, transport measurements have shown that this system goes through a Mott-Hubbard-like metal-to-insulator transition when carriers within STO quantum wells 2 uc (unit cells) thick or less are sandwiched between relatively thick GTO layers [34]. In samples with thin GTO layers, SQUID magnetometry has suggested a critical GTO thickness of 6 uc (2 nm), below which GTO transitions from its bulk ferrimagnetic state [21] into a paramagnetic state in conjunction with a 33% reduction in Ti-O-Ti bond angles in the center of the GTO layers [32]. This implies an ability to exert fine control over the magnetic state of GTO through interfacial manipulation of its octahedral tilts.

In this work, we explore the coupling between octahedral tilts and magnetism in confined GTO films by using polarized neutron reflectometry (PNR) to probe their interplay in thin GTO layers. Surprisingly, our data show no evidence of a ferrimagnetic-paramagnetic transition near the thin well limit, but rather that GTO remains ferrimagnetic down to layers as thin as 4 uc (1.6 nm). The magnetization curves extracted from the PNR data are analyzed us-

ing models both with and without magnetic dead layers (MDLs) in the GTO. When examined using a model with no MDLs, the thinnest GTO layers show $\leq 23\%$ suppression in the apparent, saturated magnetization. With inclusion of MDLs into the model, this saturation value becomes a thickness independent value. Our results indicate that the substantial relaxation of TiO_6 octahedral tilts in GTO/STO interfaces at the thin GTO layer limit has minimal impact on the magnetically ordered state. More broadly, this implies that ferrimagnetism in GTO is largely independent of the interface-engineered t_{2g} bandwidth.

4.2 Sample Design and Experimental Methods

Superlattice samples of alternating GTO and STO layers were grown for this study using hybrid molecular beam epitaxy, as described in detail elsewhere [27, 31, 36]. The degree of distortion/tilting within the GTO titania octahedral network was controlled by varying the thickness of the GTO layers. Previous scanning transmission electron microscopy (STEM) measurements of Gd-O-Gd bond angles are used as a proxy for the relation between layer thickness and titania octahedral tilting [32]. The thin GTO superlattice contained 4 uc (1.6 nm) GTO layers, in which all of atomic planes within the GTO were distorted from their bulk tilting pattern by roughly 50% or more. The thick GTO superlattice

had 11 uc (4.4 nm) GTO layers, in which the bulk GTO tilt structure was present throughout the entirety of the layers with the exception of the one unit cell at each interface where tilts are suppressed as the titania network transitions into the neighboring STO. For this sample, thin STO spacers (0.6 nm) were used to reduce distortions to the interfacial GTO tilts.

Polarized neutron reflectometry measurements were performed on the PBR reflectometer at the NIST Center for Neutron Research. An incident wavelength of 4.75 $\mathring{A}$ neutrons was utilized and incident and outgoing polarization channels were defined via a combination of Mezei spin flipper coils and Fe/Si supermirrors. Samples were mounted in a cryostat with the film's surface normal to the scattering wavevector, q. PNR measurements were collected in a zero field cooled (ZFC) state by cooling the sample from well above the Curie temperature to 5 K under no applied field, then polarizing the sample to μ_0H = 3 T applied in the plane of the film and collecting PNR scans as the field was stepped back to zero. The layer thicknesses and interface quality of these samples were characterized using non-resonant, unpolarized x-ray reflectometry (XRR) performed with a Cu Kα lab diffractometer. XRR measurements were performed in air at room temperature. All reflectometry data sets were refined to layer models using the Refl1D code that implements an optical matrix formalism [82, 117].

4.3 X-ray Reflectivity Data and Models

Figures 4.1 (a) and (c) contain the XRR data and model fits for thin and thick GTO superlattices, respectively. The refined structural models corresponding to these samples are shown in the Figs. 1(b) and 1(d). During refinement, all layers were allowed to have an independently refined thickness, but layer chemistry and interface roughness were confined to be uniform for all layers of a given type in order to reduce the number of free parameters. The topmost layer in each sample was allowed to be unique in order to account for surface degradation, which is more prevalent in samples with a rare earth titanate cap (i.e. here, the thick GTO superlattice). Average GTO layer thicknesses were refined to be 4.48 $\pm$ 0.06 nm for the thick GTO sample and 1.57 $\pm$ 0.06 nm for the thin GTO sample and are in near perfect agreement with the designed structures. The apparent chemical roughnesses, which are effectively averaged over the entire x-ray beam spot ($\approx$ 10 mm^2), span a small range from $2.3 - 4.4$ $\mathring{A}$ and attest to the excellent quality of these films. Previous reflectometry and electron microscopy studies on this system suggest local interfaces are in fact atomically sharp [33, 44], and the apparent roughness values arise from steps on the substrate surface propagating upwards through the film, rather than chemical intermixing.

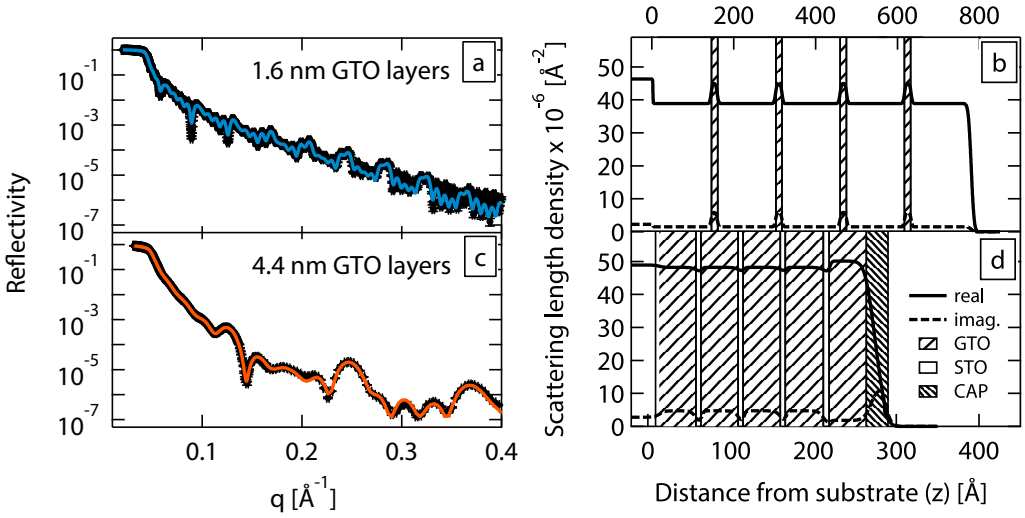

Figure 4.1: X-ray reflectometry data and calculated fits to the two GTO-STO superlattices measured in this study: (a) 1.6 nm or 4 uc thick $GdTiO_3$ layers, and (c) 4.4 nm or 11 uc thick $GdTiO_3$ layers. The refined models from which the curve fits were calculated are shown in panels (b) and (d) for thin and thick GTO samples respectively.

4.4 Polarized Neutron Reflectivity Data and Models

We begin by analyzing PNR data for the thin GTO sample with 4 uc GTO layers using a magnetization model without dead layers, similar to that previously applied to the GTO/STO system [44]. Figure 4.2(a) shows PNR data collected at 5 K after cooling under zero field then applying μ_0H = 3 T at base temperature. Refinement of this data shows that the thin GTO layers still exhibit a net in-plane magnetization and reach 2.7 $\pm$ 0.1 μ_B/fu in the center of the GTO layers under the assumption of no magnetic dead layers. This is reduced from the 3.5 $\pm$ 0.1 μ_B/fu observed in the thick GTO superlattice (Fig. 4.2 (b)) measured under the same conditions and refined using the same model [44]. The survival of robust ferrimagnetism at this thin well limit where TiO_6 octahedral tilts have been suppressed by over 50% is surprising [32] and deviates from the current picture of completely quenched magnetism at this limit. Instead, the small ($\approx 23\%$) apparent suppression of the moment suggests the presence of magnetic dead layers at interfaces that begin to occupy a larger volume fraction of the thinner GTO layers.

Therefore, the data were reanalyzed incorporating MDLs into the layer model of the multilayer film. A number of different MDL models were com-

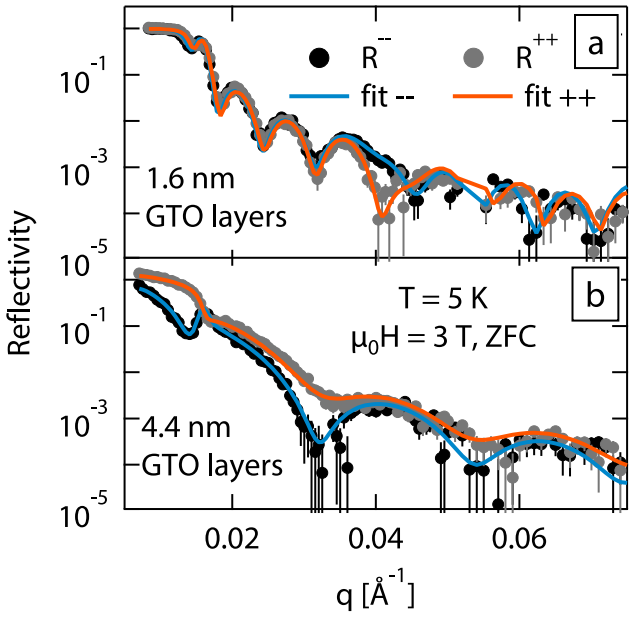

Figure 4.2: Polarized neutron reflectometry data and refined fits for (a) thin GTO layer and (b) thick GTO layer superlattices measured in a ZFC state under a μ_0H = 3 T applied field.

pared, the most descriptive of which is shown in Fig. 4.3 where refined magnetization profiles of the thin GTO superlattice with and without MDLs are overlaid on the chemical layers. This model has matching MDLs on both sides of the GTO layer that begin at the chemical GTO/STO interface and extend 2.5 $\mathring{A}$ into the GTO layer (i.e. none of the MDL is contained in the STO layers). Roughnesses of the MDLs were constrained to be no smaller than the chemical roughnesses of the interfaces where the MDLs were located. The justification for this roughness constraint stems from the interpretation of the local chemical interface roughnesses arising from the stepped substrate, which implies these values represent lower limits below which roughness values lose physical meaning. Because of the small MDL thicknesses relative to the chemical roughness, roughnesses were propagated across multiple interfaces when calculating reflectometry profiles.

Within this MDL model, the moment in the center of the thin GTO layers rises to 3.9 $\pm$ 0.1 μ_B/fu, and thick GTO layers show a smaller rise to 3.8 $\pm$ 0.1 μ_B/fu. This highlights that the effect of MDLs on the refined magnetization is proportional to the relative volume fraction of GTO layers lost due to the addition of MDLs. The fits to the 3 T ZFC data from these MDL models are plotted in Fig. 2(a) and 2(b), respectively. Further analysis demonstrates that the incorporation of MDLs improves modeling of PNR data both visually and numerically.

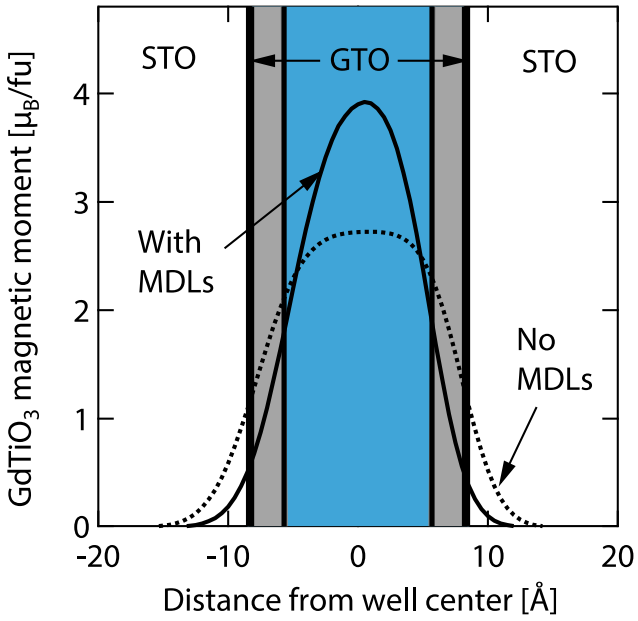

Figure 4.3: Refined GTO layer magnetization profiles for the thin GTO superlattice under the assumptions of no MDLs (dashed) and 2.5 $\mathring{A}$ MDLs. These profiles are overlaid on a schematic representation of the best MDL model, in which the MDLs (grey regions) begin at the chemical GTO/STO interface and extend 2.5 $\mathring{A}$ into the GTO layers.

4.5 Alternative Magnetic Dead Layer Models

Three progressively more complex layer models were used to analyze the existence and features of magnetic dead layers within the GTO/STO heterostructures. These models are:

1. Uniform MDLs at only buried interfaces
2. Uniform MDLs at all interfaces (including surface)
3. Unique MDLs at the surface and substrate interfaces

Determination of which model was most consistent with the measured data was done using the 0.7 T FC and 3 T ZFC base temperature data sets. These measurements conditions were chosen because they represent the most fully-polarized states in which these samples were measured. Additionally, and for aid in model determination, data were collected out to higher momentum transfer values, q, for these samples and fields to reduce as much as possible the number of models that could accurately capture features in the data. Note that when refining each of the three models, both nuclear and magnetic scattering length densities (SLDs) were allowed to vary slightly in order for the sample model and calculated fits to be optimized for a given MDL configuration.

In applying the three models to these data sets, Model (2) was found to be a significantly better description than Model (1). In other words, the presence of a MDL at the film-air interface significantly improved the models fit to the data. To illustrate this point, Fig. 4.4(a) and (b) compares these two models for the thick GTO film in its FC state while Fig. 4.5(a) and (b) show the refined layer profiles. Upon moving from Model (1) to Model (2), there is an improvement in χ^2 from 3.59 to 2.97 as well as a notably better visual fit to the data at the bilayer repeat reflection q $\approx$ 0.10-0.11 $\mathring{A}^{-1}$.

Model (3) does perhaps provide a slight improvement over Model (2) at the highest q range ($>$0.13 $\mathring{A}^{-1}$). However, this change comes at the expense of adding four free parameters to the model (i.e. thickness and roughness of each MDL), and the overall χ^2 actually rises from 2.97 to 3.08. Moreover, there is a visual discrepancy that develops in the region immediately prior to the bilayer repeat position, q $\approx$ 0.07-0.09 $\mathring{A}^{-1}$. In this region, the measured data from the two polarization channels lie on top of one another, but as shown in Fig. 4.4(c), Model (3) causes a slight splitting in the fit curves to widen relative to Model (2). Together these results demonstrate that the additional freedom of Model (3) does not lead to a meaningful improvement in the models goodness of fit.

Therefore, Model (2) was chosen as the most appropriate model; the one that captures all relevant features of the measured data without incorporating

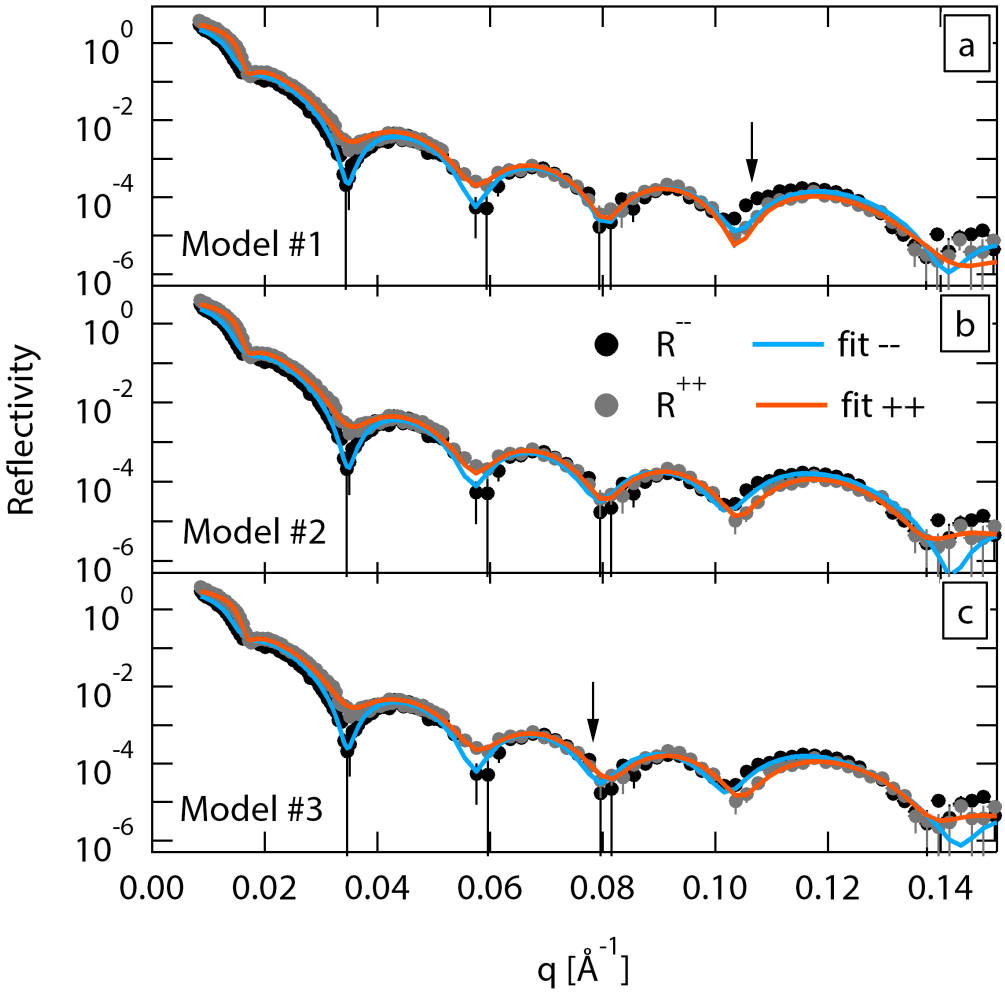

Figure 4.4: Polarized neutron reflectivity data from the superlattice with thick GTO layers measured at 5 K in a field cooled state and fit to the three different MDL models described in the text. Arrows highlight regions of poor fitting.

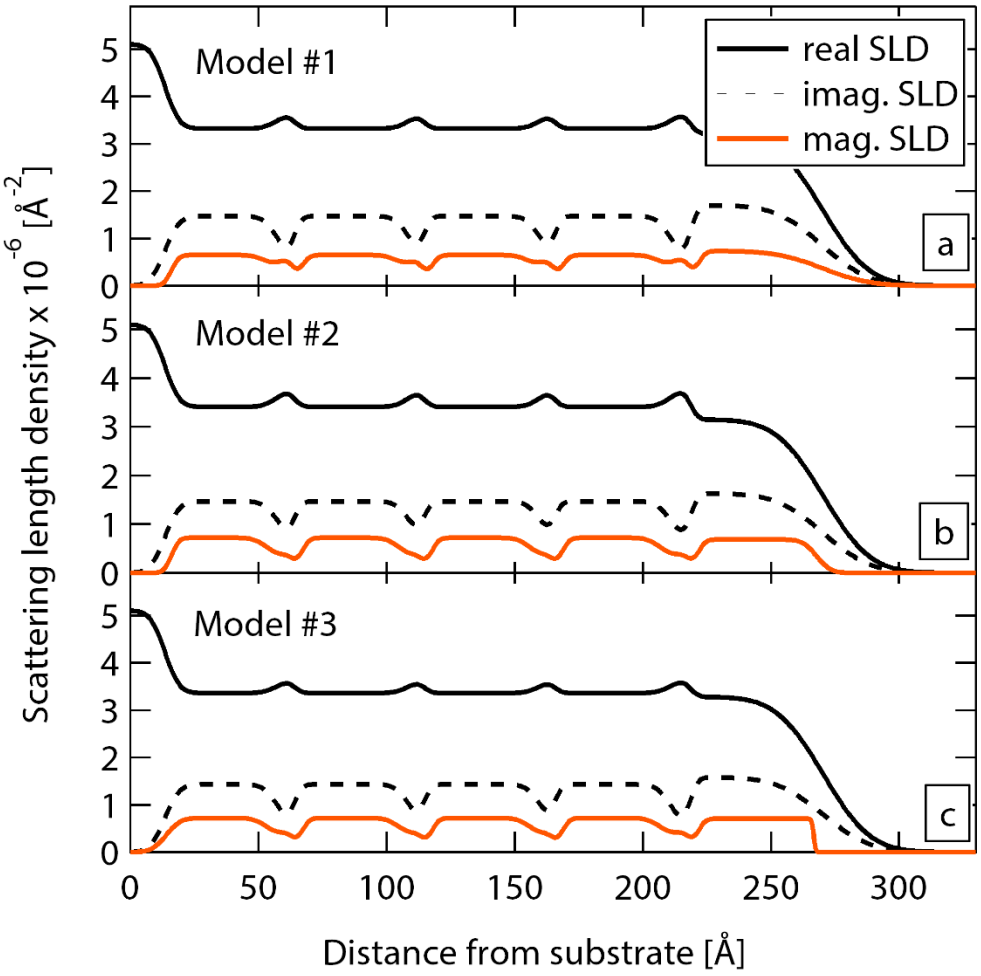

Figure 4.5: Refined sample layer models corresponding to the data and fits shown in Fig. 4.4. The real and imaginary components of the nuclear scattering length densities are shown as solid and dashes black lines, respectively. The magnetic contribution is shown in orange.

extra fit parameters. While the thick GTO sample was used here to illustrate the difference between MDL models, similar trends were observed when refining models for the thin GTO sample.

Finally, in Figure 4.6, we compare the best MDL model (i.e. Model (2)) to an identical model with the MDLs removed. The model with MDLs has 2.5 $\mathring{A}$ MDLs incorporated at the STO/GTO interface. Chi squared values are reported for each model and clearly indicate a better mathematical fit is achieved by the model with MDLs. Furthermore, the arrows near q = 0.105 $\mathring{A}^{-1}$ highlight a region in the data that is not captured well by models without MDLs. In short, this model comparison shows that a model with MDLs provides a better fit to the measured data, both visually and numerically, and substantiates the use of MDL models in analyzing PNR data collected at other fields.

4.6 Zero Field Cooled Magnetization Summary

Applying the MDL model to the entire ZFC dataset for both thick and thin GTO samples results in a field polarized magnetization that is independent of GTO layer thickness, as shown by the filled symbols in Fig. 4.7. The thin GTO superlattice refined to a model with no MDLs is also included as a reference. Isothermal magnetization data on both films are characterized by little to no

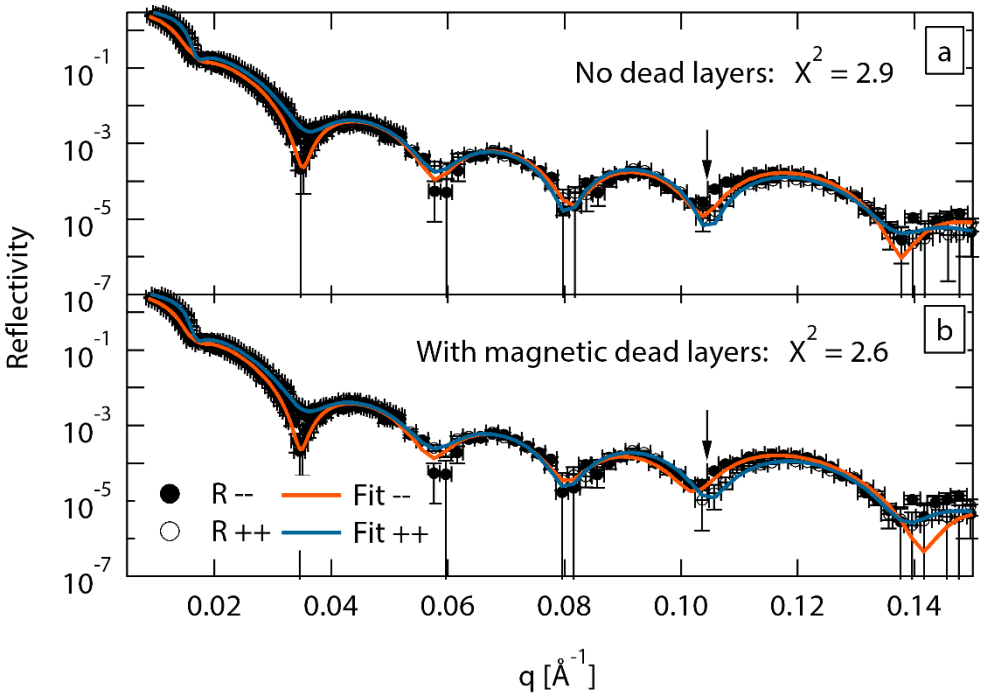

Figure 4.6: Polarized neutron reflectivity data fit to otherwise identical models (a) without MDLs and (b) with MDLs. Arrows highlight regions of poor fitting.

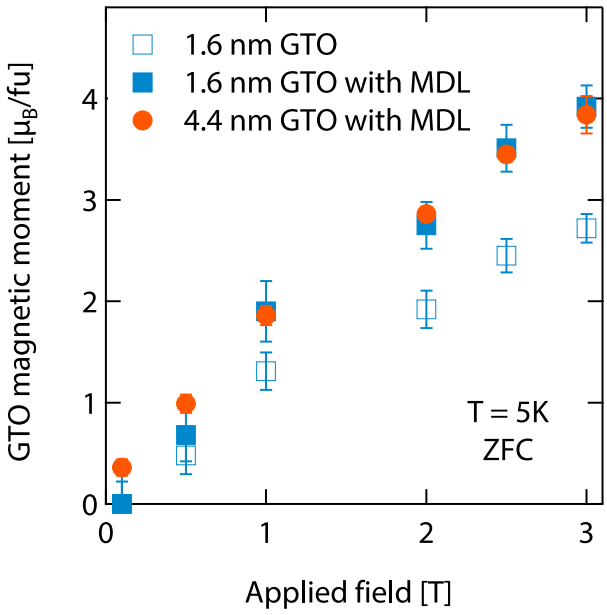

Figure 4.7: GTO magnetic moment values determined via refinement of polarized neutron reflectometry data measured in a ZFC state and plotted as a function of applied magnetic field. Moments refined with an MDL model are shown by filled symbols. Open symbols show the refined moments for the thin GTO sample when no MDL are included.

remnant magnetization upon field removal and a slow onset of saturation that agree well with previously reported magnetometry data from bulk GTO [21]. Note that single ion paramagnetism is easily be ruled out as a possible explanation of this data by considering the well-defined order parameter of these films and comparing the temperature dependence of the observed magnetization with that predicted by a Brillouin function.

4.7 Evidence Against Single Ion Paramagnetism

We can conclusively show that the single-ion physics modeled by a trivial Brillouin function cannot account for the magnetization we observe in our GTO/STO multilayer films. Below we provide three clear reasons why such a paramagnetic response is the wrong physical interpretation for our data.

First, we begin by noting that GTO thin films have been studied extensively in the literature and previous SQUID magnetometry studies on GTO films that were grown by the same group and of similar thicknesses as the samples reported here (3.5 and 2.4 nm vs. 4.4 and 1.6 nm) show a well-defined ferrimagnetic order parameter with an onset between 20 K and 30 K [32, 36]. This combined with small hysteresis loops reveal a ferrimagnetic response akin to that reported in bulk GTO. We observe only subtle evidence of the small hysteresis in our PNR data, likely because the polarization spin flip ratio is diminished at small fields where the applied field becomes comparable to the neutron guide field. Nonetheless, an ordering response within GTO films has been repeatedly shown and precludes a paramagnetic interpretation at 5 K

Moreover, we can leverage the fact that we know that 4 nm GTO layers order ferrimagnetically near 30 K and the fact that the magnetization response of 4.4 nm and 1.6 nm GTO layers in our samples look identical once MDLs are

accounted for. It is reasonable to deduce magnetization in these samples shares a common origin (ferrimagnetic order).

Second, the observed magnetic response in our thin GTO sample does not conform to the expectations of a trivial Brillouin function. In very thick films (20 nm) at H = 3 T and T = 5 K, the magnetization is only $\sim$4.5 μ_B/f.u. [3]. This is very close to the $\sim$4.0 μ_B/f.u. we observe in the thin GTO layer limit (1.6nm film) at 5 K and 3 T. As the referee notes, both are substantially smaller than the expectations of a J=7/2 free Gd^{3+} ion which should be nearly 5.5 μ_B/f.u. at 5 K and 3 T. Since we know the volume of Gd ions via the chemical profile in reflectometry, the only way to account for this reduced moment using this Brillouin treatment is to introduce an exchange field in a modified Brillouin function treatment. Since the magnetization response of the ordered GTO films at both 20 nm and 4 nm thicknesses matches that of the thin 1.6 nm film, this would require the same exchange field for all samples (if you ignore the MDLs, the exchange field would even have to increase in the thin GTO sample, which doesnt make physical sense). In this modified single-ion scenario, the conclusions would still be that lowering the GTO thickness has little to no impact on the magnetic exchange/ground state.

(3) Even ignoring the previous two points, the data do not follow the temperature-dependence of a Brillouin function single-ion response. We can

compare the temperature evolution of the response that we observe in the 1.6 nm GTO film with that expected for a Brillouin single-ion treatment of Gd moments. At 30 K and 0.7 T, a paramagnetic response in the GTO layers should still show a 0.33 μ_B/Gd moment polarization. However, a measurement of our thin GTO film (1.6 nm) taken under these conditions and displayed in Fig. 4.8 shows zero magnetization even though 0.33 μ_B/Gd is well within the resolution of our measurement.

4.8 Discussion

The results of the field-dependent PNR analysis suggest that the apparent suppression of magnetization, in this work and also the previous SQUID magnetometry study [32], is likely an effect of neglecting the magnetic dead layers at the GTO/STO interface and instead averaging magnetization over the entire GTO layer. When these dead layers are incorporated into a model of these systems, the two PNR data sets collapse onto one another, indicating that the magnetism in the center of the GTO layers is independent of the interface-induced octahedral tilting. From the reported bond angles in GTO/STO heterostructures [32], this is true up to at least a 50% change in distortion of the octahedral network from its preferred bulk pattern (Ti-O-Ti angle $\approx 144^\circ$) towards an undis-

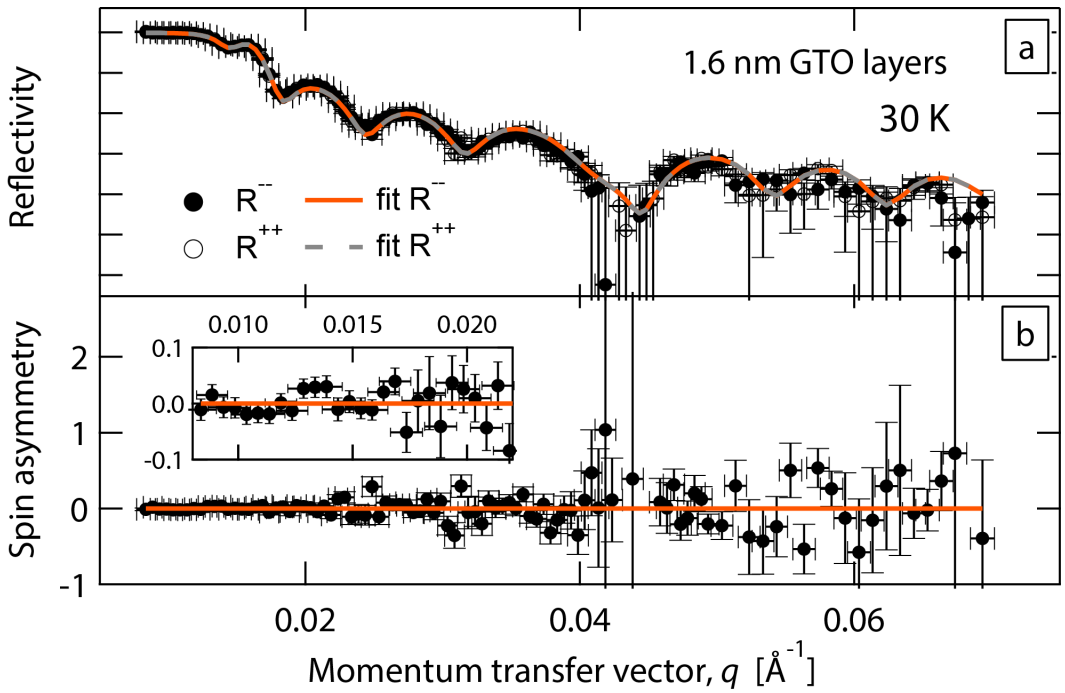

Figure 4.8: Polarized neutron reflectivity (a) and spin asymmetry (b) for the GTO/STO heterostructure with thin, 1.6 nm GTO layers from the main manuscript collected under 0.7 T applied field. There is no splitting between polarization channels and the spin asymmetry data falls statistically along zero.

torted structure (Ti-O-Ti angle = 180°).

We stress here that even absent the presence of modeled MDLs, the observed ferrimagnetism in 4 uc thick GTO is only suppressed 23% relative to bulk-like, 11 uc thick GTO. This is a surprisingly weak perturbation to the magnetism given the known alteration of the octahedral tilt structure in these thin GTO layers and an unambiguous demonstration that robust ferrimagnetism persists well below the previously reported bound of 6 uc thick GTO layers.

Additional support for the inclusion of MDLs into the model of GTO/STO interfaces comes from the frequency with which heterointerfaces result in the formation of MDLs near the interface. For instance, MDLs are often observed in both ferromagnetic metals [133–135] and oxides such as $La_{1-x}Sr_xMnO_3$ (LSMO) and $La_{1-x}Ca_xMnO_3$ (LCMO) [136–140]. The origins of these MDLs are typically unique to the interface in question. While structural distortions are a common source of MDLs, that explanation is ruled out in the GTO/STO system because the interfacial, MDL-containing unit cell in thick ($\geq$ 3.5 nm) GTO is distorted by approximately 50%, the same level of distortion that is present in the center of thin (1.6 nm) GTO layers that show unperturbed ferrimagnetism.

Another possible source of MDLs is orbital reconstruction at the interface. This is particularly relevant for oxide heterostructures where orbital reconstruc-

tion is a regularly observed feature [43, 141–143]. In the case of thin LSMO layers, x-ray measurements have shown that the $3z^2$-r^2 orbital is preferentially occupied, leading to a weakening of the double exchange responsible for LSMO's FM and resulting in its observed MDLs [109, 144]. In bulk GTO, first principles calculations suggest both orbital ordering and FM are stabilized by a hybridization of the t_{2g}-e_g orbitals [15]. This hybridization is due to the $GdFeO_3$-type octahedral distortion and, as that distortion is decreased, FM exchange is weakened. Thus while evidence for orbital reconstruction in GTO/STO has yet to be reported, it is possible to speculate towards a case where, either via compressive strain or symmetry breaking at the interface, an orbital reconstruction occurs. This may result in decreased t_{2g}-e_g overlap and hybridization pushing the system towards a FM-AFM instability, but this is not directly reflected in the reported Gd-O-Gd bond angles that have been used as a proxy for octahedral tilting and rotations in this study.

4.9 Conclusions

In summary, polarized neutron reflectometry was employed to explore the relationship between the cooperative structural distortion of the TiO_6 octahedral network and the ferrimagnetic state in GTO thin films. PNR measurements

provide evidence that ferrimagnetism in GTO layers survives nearly unperturbed as the single layer limit is approached. Specifically, the saturated moment of the ferrimagnetic state in GTO layers as thin as 4 uc is reduced by only 23% relative to bulk-like layers in models neglecting the potential presence of MDLs and becomes identical to bulk-like layers once models incorporating MDLs are used. Incorporating thin MDLs at GTO/STO interfaces improves refined models of PNR data; however analysis of the data within either approach reveals that the magnetization in the interior of GTO layers (excluding MDLs) is largely independent of changes in octahedral tilts and rotations as measured by Ti-O-Ti bond angles. Our data curiously point toward a picture of correlated magnetism in GTO which is decoupled from the modified octahedral tilts thought to drive the metal-insulator instability in this compound.

Chapter 5

Quasistatic Antiferromagnetism in the Quantum Wells of $SmTiO_3/SrTiO_3$ Heterostructures

High carrier density quantum wells embedded within a Mott insulating matrix present a rich arena for exploring unconventional electronic phase behavior ranging from non-Fermi-liquid transport and signatures of quantum criticality to pseudogap formation. Probing the proposed connection between unconventional magnetotransport and incipient electronic order within these quantum wells has however remained an enduring challenge due to the ultra-thin layer

thicknesses required. Here we address this challenge by exploring the magnetic properties of high-density $SrTiO_3$ quantum wells embedded within the antiferromagnetic Mott insulator $SmTiO_3$ via muon spin relaxation and polarized neutron reflectometry measurements. The one electron per planar unit cell acquired by the nominal d0 band insulator $SrTiO_3$ when embedded within a d^1 Mott $SmTiO_3$ matrix exhibits slow magnetic fluctuations that begin to freeze into a quasistatic spin state below a critical temperature T^*. The appearance of this quasistatic well magnetism coincides with the previously reported opening of a pseudogap in the tunneling spectra of high carrier density wells inside this film architecture. Our data suggest a common origin of the pseudogap phase behavior in this quantum critical oxide heterostructure with those observed in bulk Mott materials close to an antiferromagnetic instability.

5.1 Introduction

The origin of pseudogaps near electronic instabilities and their relationship to emergent phase behaviors in numerous transition metal oxides remains an enduring topic of research [145, 146]. Though the underlying mechanisms of pseudogap formation remain debated in many compounds, canonical examples of pseudogaps in strongly correlated oxide systems often appear coincident with

the partial suppression of the Mott state and the disappearance of long-range antiferromagnetism [147, 148]. Pseudogaps in these systems develop below a characteristic temperature T^*, leading to the conjecture that they are the consequence of an unresolved order parameter or crossover [149, 150]; however, the myriad of competing states ($e.g.$ superconductivity [151], charge density wave order [152, 153], spin stripe order [154]) that also arise in close proximity to the Mott phase render this connection difficult. Furthermore, the ubiquitous transition into nanoscale electronically phase separated states upon doping Mott states further blurs the unique resolution of an order parameter accompanying the pseudogap's formation [152, 155, 156].

While the majority of studies begin with the Mott state and introduce carriers to access the pseudogap regime [7, 157–159], an alternative approach to exploring pseudogap formation is to step toward the insulating state from a weakly correlated Fermi liquid ground state. This is challenging to do under fixed disorder in bulk transition metal oxides; however thin film heterostructures with two dimensional quantum wells provide a novel means of accomplishing this alternative approach. For instance, carriers can be induced within the conduction band of a d^0 layer such as $SrTiO_3$ via the creation of polar discontinuities at its bounding interfaces [30]. The induced carriers form two-dimensional electron gases at each interface and the total carrier density delocalized into the $SrTiO_3$

well can be controlled by tuning the well's thickness. Correlation effects can be activated as the electron density in the well diverges [112], and heterostructures built from $R^{3+}TiO_3/SrTiO_3$ (R = rare earth) interfaces have demonstrated that metal-insulator transitions can be driven near the thin well limit of a single SrO layer [34].

Recent studies exploring heterostructures built from $SrTiO_3$ quantum wells embedded within a $SmTiO_3$ Mott insulating matrix have shown that, as the thin well limit is neared, $SmTiO_3/SrTiO_3$ architectures manifest an unconventional non-Fermi liquid metallic state with anomalous magnetotransport properties [28, 113]. Chief among these is the appearance of a low temperature pseudogap state whose onset temperature T^* is enhanced with increasing carrier density (thinner wells) [160]. The proximity of antiferromagnetism in the Mott insulating $SmTiO_3$ host matrix of this heterostructure is hypothesized to be endemic to this behavior and suggests parallels to the pseudogap states observed in close proximity to antiferromagnetic Mott states in a variety of bulk transition metal oxides.

In this paper, we report the results of a combined muon spin relaxation (μSR) and polarized neutron reflectometry (PNR) study exploring the origins of the pseudogap state in high carrier density $SmTiO_3/SrTiO_3$ quantum well heterostructures. Low energy μSR measurements capable of implanting a sub-

stantial fraction of muons within the quantum wells of this structure reveal the onset of an additional channel of muon spin damping within the T^* pseudogap phase. Precessional damping consistent with the onset of magnetic correlations within the unbound electron liquid residing within quantum well of this structure is observed, and PNR measurements preclude ferromagnetic correlations as the origin of this damping. Our data demonstrate the onset of quasistatic antiferromagnetic correlations coincident with the T^* state inside the $SrTiO_3$ quantum wells and suggest that incipient antiferromagnetic order drives the formation of the pseudogap state in this oxide heterostructure [160]. More broadly, our results suggest that high density quantum wells driven close to a correlation driven metal-insulator transition emulate the essential physics underlying bulk antiferromagnetic Mott states as they are destabilized via carrier substitution.

5.2 Sample Design and X-ray Characterization

Low energy SR data were collected from three thin film samples in both a weak transverse field (wTF) and under zero applied field (ZF). One sample was a 20 nm $SmTiO_3$ (SmTO) film used to observe muon depolarization arising from SmTO in the absence of proximate $SrTiO_3$ (STO). The other two samples were trilayer heterostructures containing 10 nm SmTO barrier layers bounding a STO

quantum well with thicknesses of 2 and 4 nm. A 2 nm (4 nm) STO quantum well is composed of 5 SrO (10 SrO) planes alternating with 6 (11) planes of TiO_2, and all quantum well thicknesses are hereafter referenced by their number of SrO planes. Previous tunneling spectra show that in a 5 SrO quantum well a pseudogap opens at $\sim$20 K, while a 10 SrO well does not display a gap opening above 2 K [160].

Excellent sample quality consistent with previous reports [32, 33, 44], including uniform layer thicknesses and sharp interfaces, was verified for a 5 SrO quantum well heterostructure embedded between thick SmTO spacer layers using x-ray reflectometry (Fig. 5.1(a)). Simulated muon implantation profiles for the samples above were calculated for various implantation energies with the TRIM.SP Monte Carlo code [91]. Figures 5.1(b) and (c) show the simulated implantation profile for 1.5 keV incident muons for the 5 SrO and SmTO control samples, respectively. This energy was found to maximize the percentage of muons landing within the STO quantum wells, resulting in nearly a quarter of all incident muons landing within the STO layer for the case of the 5 SrO thick well.

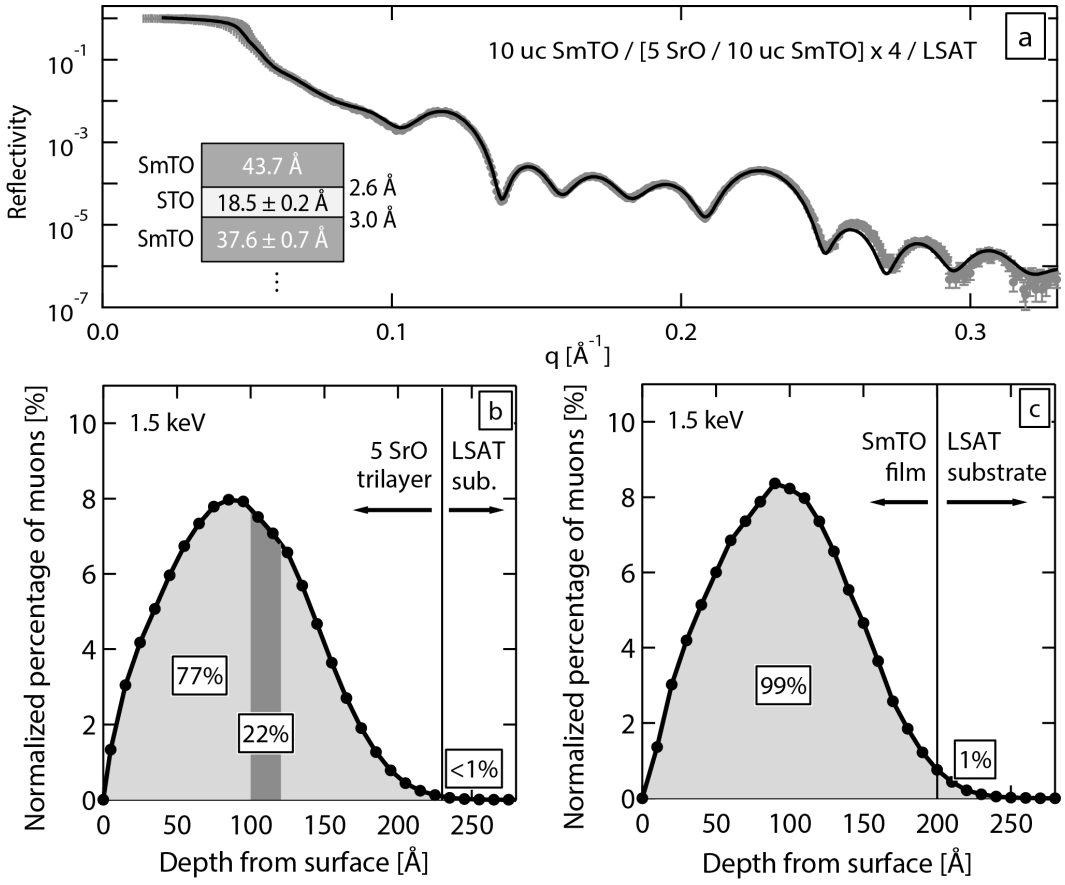

Figure 5.1: (a) X-ray reflectometry data and fit to a $SmTiO_3/SrTiO_3$ superlattice with 5 SrO thick quantum wells. Schematic inset shows the superlattice layer stack with interfacial rms roughness values for the top interface of each type of layer. Simulated muon implantation profiles, for (b) the trilayer quantum well and (c) the $SmTiO_3$ film, calculated using the TRIM.SP Monte Carlo code.

5.3 Weak Transverse Field μSR Data

wTF μSR measurements are shown in Fig. 5.2 where the average time-dependent muon polarization $P(t)$ was fit to the form $P(t)$=exp(-λt)cos(γ_μBt+ϕ) where B is the local field at the muon stopping site, γ_μ = 851.6 Mrad s^{-1} T^{-1} is the muon gyromagnetic ratio, and ϕ is a phase constant which is determined by the detector positions relative to the initial muon spin polarization. Here the depolarization rate λ represents an average response of the muons throughout the sample volume. In wTF measurements λ is typically dominated by dephasing between individual muon decay events due to slight variations in the static local field at the muon location [89, 104]. An increase in λ for a system containing local magnetic moments is conventionally interpreted as the slowing down of the magnetic moment fluctuation rate due to the onset of spin freezing or ordering.

Figure 5.2(a) shows the temperature evolution of the transverse depolarization rate, λ, for the 5 SrO film. As the film is cooled, an initial increase in λ is observed followed by a partial saturation near the expected Neel temperature T_{N1}= 60 K for the Ti^{3+} sublattice in bulk $SmTiO_3$. Upon further cooling, a second increase in λ followed by a partial saturation is observed at T_{N2}=40 K, consistent with the expected Sm^{3+} sublattice bulk ordering temperature [21, 63].

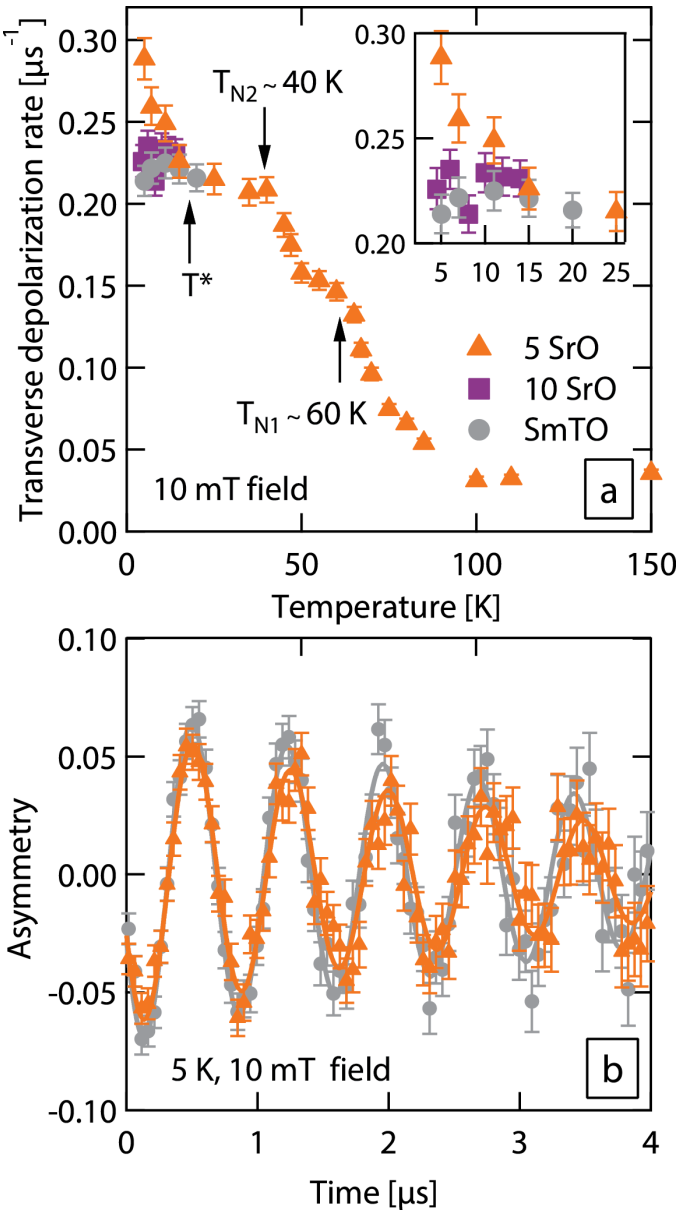

Figure 5.2: Temperature-dependence of the muon transverse depolarization rates (a) for the trilayer 5 SrO film (orange triangles), 10 SrO film (purple squares), and SmTO control film (grey circles) extracted from fitting weak transverse field data, as shown in (b) for the 5 SrO and SmTO samples at 5 K. Both plots use the key shown in (a).

Surprisingly however, as the 5 SrO film is cooled below T_{N2}, a third, nonsaturating upturn in λ appears below 20 K.

Instead, this anomalous low temperature increase in the wTF λ suggests a third set of moments freezing, distinct from the two ordered sublattices in the SmTO layers. Further illustrating this distinction, low temperature wTF μSR measurements collected on the 10 SrO and SmTO control films are overplotted with the 5 SrO data in Fig. 5.2(a). Importantly, no comparable low temperature upturn in λ below 20 K is observed in either sample. This demonstrates that the enhanced λ observed in the 5 SrO architecture is not inherent to SmTO, nor is it due simply to the addition of an STO layer or SmTO/STO interface. Raw data demonstrating the difference in the decay envelope of asymmetry values $P(t)$, from which λ is extracted, of the 5 SrO and SmTO films at 5 K are plotted Fig. 5.2(b).

We stress that muonium formation cannot be the origin for this additional upturn in λ the 5 SrO data for a number of reasons. First, muonium is suppressed in both conducting (STO quantum wells) and magnetic materials (SmTO). Second, no upturn is observed in the 10 SrO sample, where approximately 50% of the well width is outside of extent of the interface induced 2DEL (i.e. insulating regions) [31]. In the case of an undoped STO film, muonium formation was previously shown to occur at 70 K [161], far from the 20 K up-

turn in the trilayer wTF data. Finally, muonium formation leads to the formation of additional frequencies in wTF measurements as well as substantially reduced initial asymmetry values, neither of which are present in our data.

5.4 Zero Field μSR Data

Zero field μSR data were collected to provide further insight into the different low temperature magnetic states observed in wTF. Shown in Fig. 5.3 are zero field cooled, ZF μSR data collected at 5 K that have been fit to a model composed of a linear combination of two exponential functions, $P_{ZF}(t) = fe^{-\lambda_{fast}t} + (1-f)e^{-\lambda_{slow}t}$. This type of function is commonly used to capture disordered magnetic systems in which oscillations from long-range magnetic order have been overdamped [162–164]. The fast relaxation term λ_{fast} conventionally reflects muons depolarized via an inhomogeneous, static local field while the λ_{slow} term is reflective of muons depolarized via slower fluctuations [164]. The lack of ZF oscillations in the ordered state of $SmTiO_3$ may be attributed to these layers possessing two magnetic sublattices with similar ordered moments [63] and four-fold symmetric domains 50-100 nm in diameter when grown on cubic LSAT substrates [33, 36]. In addition, the large energy spread ($\sim$0.5 keV) of the incident muons reduces the t_0 resolution of the spectrometer [91]. Together

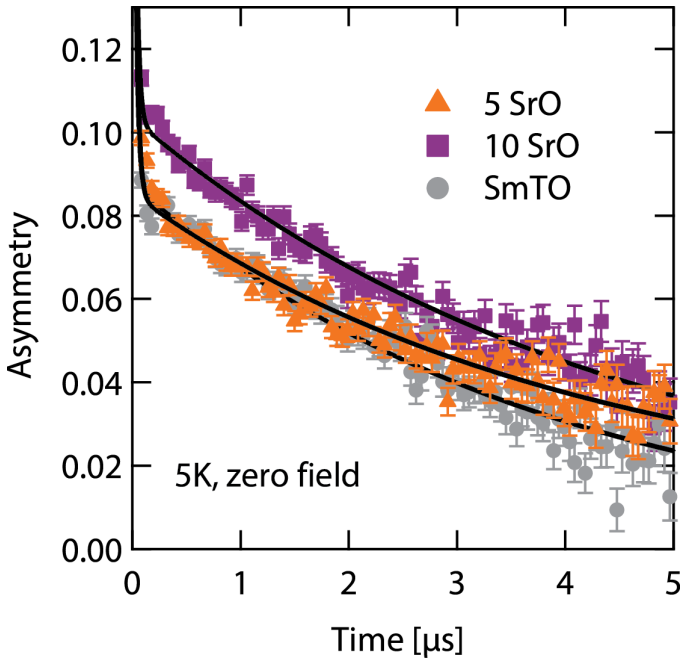

Figure 5.3: Zero field muon spin relaxation measurements of the 5 SrO film (orange triangles), 10 SrO film (purple squares), and SmTO control film (grey circles) at 5 K.

these features make the observation of ZF oscillations unlikely, and instead λ_{fast} is determined by the nonuniformity of the internal field seen by the muons.

Relaxation rates for the fast and slow depolarization processes in the STO portion of the quantum well structures were extracted using rates measured independently from the SmTO control film to represent the 78% (70%) of the 5 (10) SrO film muon stopping sites outside of the STO well. The best fit to the SmTO data was achieved with a fast fraction of muons, $f_{fast} = 0.73 \pm$

0.003, decaying at 44.5 $\pm$ 1.05 μs^{-1} while the slowly decaying fraction of muons decayed at 0.26 $\pm$ 0.005 μs^{-1}. The remaining 22% (30%) of the 5 (10) SrO film volume is described by using the same form of fast and slow relaxation terms, representing the quasistatic ordered and slow spin fluctuation contributions to the muon decay in the STO well respectively.

The STO in the 5 SrO film had a similar fraction of fast decaying muons, f_{fast} = 0.79 $\pm$ 0.006, as the pure SmTO film. This similarity suggests two corollaries: (1) the 5 SrO film is magnetized to a similar degree as the SmTO film, a known antiferromagnet well below its Neel temperature, and (2) the entirety of the 5 SrO sample, including the entire STO quantum well, possesses these magnetic correlations, as was previously shown to be the case for STO quantum wells embedded within a $GdTiO_3$ matrix [44]. In a homogeneous or nearly ordered picture of the STO layer, this corresponds to the onset of quasistatic magnetic order with $\cos^2\theta = 0.21$ with θ being the angle between the muon's incident spin and the local magnetic field. In an inhomogeneous picture, the reduction in the slowly fluctuating volume fraction corresponds to slow fluctuations freezing into a distinct volume possessing quasi-static spin correlations. Both scenarios are consistent with the wTF results showing a low temperature onset of quasistatic magnetism in the STO layer, and ZF data suggest the lack of saturation in wTF data below 20 K as due to robust fluctuations persisting in the STO layer at 5 K.

By comparison, the fraction of fast decaying muon in the 10 SrO film was found to be only 0.57 $\pm$ 0.005. This lower fraction of fast decaying muons in the STO of the 10 SrO film explain why, at short time scales (t $<$ 1 μs) in Fig. 3, the 10 SrO film has notably higher asymmetry values than either of the other samples. This offset arises from implanted muons that localize within a non-magnetic portion of the 10 SrO well and therefore do not undergo fast depolarization. Over longer time scales, the trends in Fig. 3 are controlled by the slowly decaying muons and their relaxation rates. The decay rates for the STO portion of the 10 and 5 SrO films both refine to be slower than the slowly decaying muons in the SmTO, 0.15 $\pm$ 0.007 and 0.08 $\pm$ 0.014 μs^{-1}, respectively.

5.5 Polarized Neutron Reflectivity Data

The low temperature enhancement of λ in the wTF measurement below T^* $\approx$ 20 K and the strong fast depolarization under ZF are suggestive of magnetic moments associated with the free electrons near quantum well interfaces of the 5 SrO film. In order to probe whether these correlations carry a net magnetization and whether a field-induced response appears similar to the case of GTO/STO quantum well heterostructures, PNR measurements were performed on a SmTO/STO superlattice film with 2 SrO thick quantum wells and 4 nm

thick SmTO spacing layers. The switch from a 5 SrO to a 2 SrO thick quantum well structure was motivated by previous measurements showing a stronger magnetic response in more highly confined well structures[44], and a field of 0.7 T (70 times larger than that utilized in wTF SR measurements) was utilized to further maximize any potential field-induced magnetic polarization in the plane of the film.

Figure 4 (a) shows that the PNR data collected at 4 K from the two non-spin flip channels (R^{++} and R^{--}) lie directly on top of one another, revealing no net magnetization in the plane of the film. To highlight the lack of a net magnetization, the spin asymmetry is plotted in Fig. 4 (b), and the nonmagnetic model fit to the data is plotted in Fig. 4 (c). As the antiferromagnetic structure of the $SmTiO_3$ layers in this superlattice has no net magnetization, this measurement is very sensitive to any potential magnetism in the $SrTiO_3$ layers. The sensitivity in this experiment is estimated to be better than 7.25 kA/m (9 mT) or roughly 0.05 μ_B per Ti ion, a value significantly smaller than the reported ordered moments for both Sm^{3+} (0.72 μ_B) and Ti^{3+} (0.43 μ_B) in $SmTiO_3$ [63]. This bound is also much smaller than the value of 1 μ_B/Ti of a fully polarized $S = 1/2$ Ti^{3+} moment naively associated with free electrons in the quantum well [44]. These data preclude a picture of a low temperature, field-driven polarized state in the 5 SrO trilayer film and instead suggest that the magnetic correlations probed in

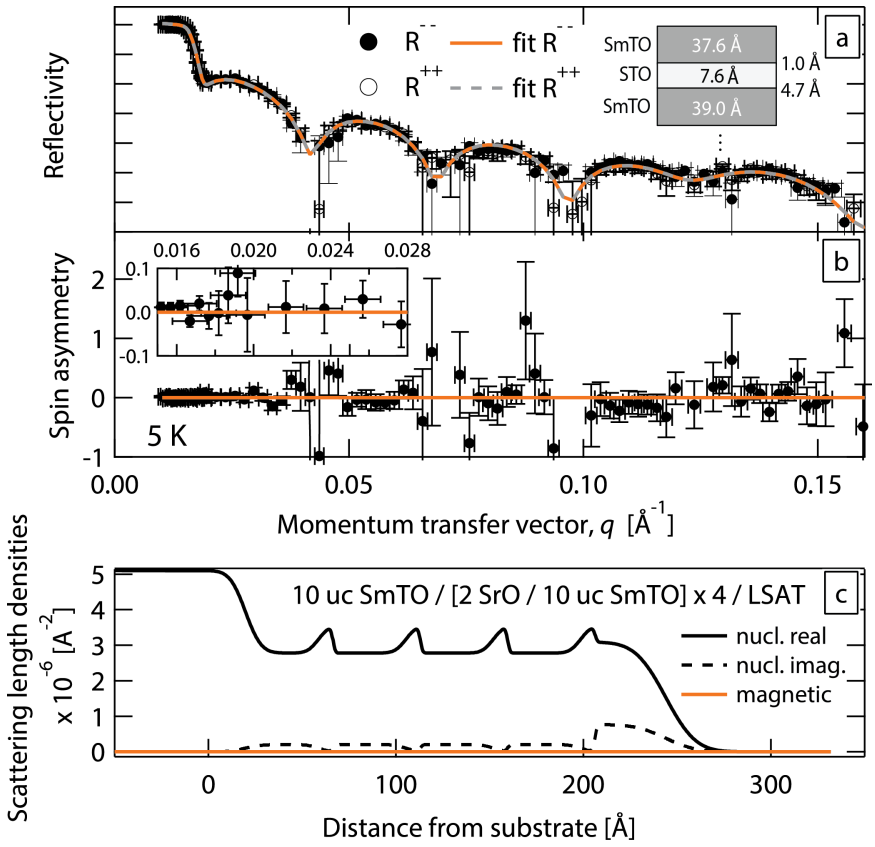

Figure 5.4: Panel (a) displays polarized neutron reflectometry data in both the R^{++} (open circles) and R^{--} (closed circles) channels. Inset shows layer structure with interfacial rms roughness given for the top of each layer type. The spin asymmetry (b) is calculated from PNR data in (a). In both (a) and (b), the best fit to the data is overlaid on the data (lines). Inset in (b) is a close up of the spin asymmetry over the critical edge and has the same axis units as the larger panel. The refined layer model of the superlattice (c) includes the real nuclear (solid black), imaginary nuclear (dashed black), and magnetic (solid orange) components of the scattering profile.

μSR data are antiferromagnetic in nature.

5.6 Non-influence of Oxygen Vacancies

When approaching the limit of rare oxygen vacancies at the interfaces, a very low density of background vacancies is difficult to ever completely preclude from contributing to conduction. However, the magnetism observed in the quantum wells of SmTO/STO heterostructures cannot arise from these hypothetical rare vacancies. Specifically, any potential small density of oxygen vacancies cannot account for the relaxation response in the main texts μSR data, which is a volume sensitive probe. The entirety of the STO quantum well exhibits slow spin fluctuations, and this is not possible from a dilute concentration of interface defects. Similarly, previous studies of magnetism arising in the quantum wells of related GTO/STO heterostructures observe an induced moment of $\sim$1 μ_B/Ti atom that appears throughout the quantum wells [44]. Both observations demonstrate that moment formation in RTO/STO (R=rare earth) quantum wells is not a small, rare region effect.

Equally important, signatures of magnetism arising from STO oxygen vacancies, in bulk form or at thin film interfaces, can be definitively differentiated from the magnetic behavior we observe in the SmTO/STO quantum wells. When

oxygen vacancies are intentionally introduced into STO, they create either ferromagnetic or superparamagnetic domains locally [165]. These vacancy-driven states have a large field induced response and are not consistent with our observation of antiferromagnetism in the quantum well of the SmTO/STO heterostructure. Our neutron reflectometry data in Fig. 5.4 further precludes any global, field-polarized state. Finally, the magnetic states formed in RTO/STO quantum wells are dependent on the interface type and well carrier densities; above a critical 3D well carrier density [28], a ferromagnetic state is induced within GTO/STO wells and an antiferromagnetic state is induced within wells formed by SmTO/STO interfaces. This is distinct from local magnetic defects formed by STO oxygen vacancies, which should be independent of interface type and carrier density.

5.7 Discussion

The quasistatic magnetic correlations observed in our μSR experiments and associated with the introduction of free electrons into the 5 SrO quantum well film could have a number of origins; however, data from the 10 SrO sample rule many possibilities out. For example, Sm^{3+} or Ti^{3+} moments localized near the well interfaces, which have not frozen/ordered due to interactions with the free

electrons in the STO layers, could in theory contribute to correlations within the well electrons themselves. Alternatively, oxygen defects in STO or at the SmTO/STO interface could produce a magnetic response. However, if either of these mechanisms were active, their signatures should have been observed in the 10 SrO sample. Furthermore, the magnetic response of trivial oxygen defects in STO is quite distinct from that observed here. One remaining alternative is that the moments of the polarity-induced electrons localized within the wells themselves may undergo quasistatic freezing. In this scenario, the onset of magnetic freezing is coupled to the free carriers in the quantum wells and can naively bias the resulting charge transport through the well.

Earlier measurements of $SmTiO_3/SrTiO_3$ heterostructures have shown that at the critical well thickness of 5 SrO layers, non-Fermi liquid transport manifests and the inverse Hall coefficient (apparent carrier density) diverges, suggestive of the influence of a nearby quantum critical point [112]. The underlying order parameter driving this anomalous well transport is likely coupled to the appearance of a low temperature pseudogap in the tunneling spectra of thin well $SmTiO_3/SrTiO_3$ heterostructures. For 5 SrO thick wells, a pseudogap appears below $\sim$20 K consistent with the T^* freezing transition resolved in our wTF μSR data [160]. This connects the quasistatic spin freezing to the free carriers in the wells and is the likely origin for pseudogap formation. Furthermore, the

proximity of the antiferromagnetic $SmTiO_3$ host is key to stabilizing this behavior. Identical quantum well structures inside a ferrimagnetic $GdTiO_3$ host do not produce a similar pseudogap state, but rather induce ferromagnetism within the quantum wells and Fermi liquid transport [44, 113, 160].

5.8 Conclusions

The opening of a pseudogap in high carrier density $SmTiO_3/SrTiO_3$ quantum well heterostructures is reminiscent of pseduogap formation in bulk transition metal oxides close to destabilized antiferromagnetic Mott states. In systems as diverse as cuprates [147], manganites [157], and iridates [159], pseudogaps emerge as the Mott charge gap is quenched, yet robust short-range/fluctuating antiferromagnetic correlations remain [166–168]. Our combined μSR and PNR data point toward a model of quasistatic antiferromagnetism induced by neighboring antiferromagnetic $SmTiO_3$ layers within high carrier density $SrTiO_3$ quantum wells. The coinciding onset temperatures of antiferromagnetic fluctuations in wTF μSR measurements and pseudogap formation from earlier tunneling measurements strongly suggest that magnetic correlations in the $SrTiO_3$ quantum well constitute the origin of the pseudogap formation in this system. Our results support the notion that the essential physics for pseudogap formation in

an array of doped transition metal oxides with parent antiferromagnetic Mott states is captured in high density quantum wells embedded within an antiferromagnetic Mott matrix.

Chapter 6

Orbital Polarization in $SmTiO_3$ Films and Heterostructures

Strongly correlated electron systems continue to shed new light on the fundamental interactions of electrons in solids. With hallmark behaviors like metal-to-insulator transitions and high temperature superconductivity, Mott insulating transition metal oxides are a canonical example of strong electron-electron correlations. Here we investigate epitaxial heterostructures of the Mott insulating rare earth titanate $SmTiO_3$ (SmTO) embedded with quantum wells of the band insulator $SrTiO_3$ (STO). This system exhibits both quantum critical transport and pseudogap behavior suggesting strong parallels with bulk Mott materials

[28, 160]. In this work, we use resonant X-ray reflectometry at the Ti $L_{2,3}$-edges to probe the orbital polarization depth profile of a SmTO film and SmTO-STO superlattices with varying STO quantum well thickness. Our results suggest that the d^1 electron in SmTO preferentially occupies the in-plane dxy orbital despite nearly 1% compressive strain from the underlying substrate. Similar in-plane polarization is observed for both SmTO and STO layers in the superlattices. These results are analyzed in terms of competition between compressive strain, quantum confinement, and Jahn-Teller distortions to the crystal field.

6.1 Introduction

In bulk rare earth titanates, RTO where R is a triavalent lanthanide series ion, evaluation of the Ti d energy levels requires consideration of crystal field effects from both the oxygen octahedron and the rare earth ions. The oxygen octahedron in bulk RTOs exhibit a cooperative Jahn-Teller distortion that increases in magnitude with decreasing ionic radius and has its strongest effects on the heavy ferrimagnetic RTO members (e.g. $GdTiO_3$, $DyTiO_3$) [15]. On the other hand, the influence of the R ion crystal field decreases with decreasing ionic radius and is most prominent in the antiferromagnetically ordered compounds near the $LaTiO_3$ end of the series. [169]. It is the competition between

these two crystal fields is believed to be responsible for selecting the magnetic and orbital ordering in the ground state of these materials, and this competition reaches a height near $SmTiO_3$ in the middle of the lanthanide series.

Results from previous studies on RTO thin films show that films down to $\sim$10 unit cells thick and sometimes less retain remarkably bulk-like magnetic properties, despite epitaxial strains on the order of one percent [32, 36, 170, 171]. It is therefore possible that the orbital ordering ground state also survives in this strained condition, since the two orderings are closely related in origin. Here we have used linearly polarized X-ray reflectometry at the Ti L-edges to probe the depth dependent orbital occupation profile of the Ti 3d levels.

6.2 Sample Design and Experimental Methods

Analysis of orbital polarization in thin film SmTO and STO-SmTO superlattices was performed using a combination of X-ray absorption spectroscopy (XAS) and resonant X-ray reflectometry (RXR). These experiments were conducted at the BESSY-II synchrotron in Adlershof, Germany on the undulator beamline UE46-PGM1. XAS spectra were collected across the Ti $L_{2,3}$ absorption edges for incident X-rays in both the sigma and pi linear polarization channels. RXR measurements were then made at a pre-resonance energy (440 eV) and

at the four peaks of the Ti XAS profile (458.1, 459.9, 463.4 and 465.5 eV) [cf. Fig. 6.1(a)]. Additional information regarding the experimental setup and the techniques' underlying physical principles can be found elsewhere [52, 61, 73].

Four samples were chosen for these experiments. All were grown on (001) LSAT substrates using hybrid molecular beam epitaxy in which Sm and Sr were supplied by sublimation of solid elemental sources and Ti and O were supplied by the metal-organic tetraisopropoxide [35, 36]. The first sample was a single layer of SmTO $\sim$20 nm thick, and it provides a critical baseline for analysis of the other three samples. These other samples are SmTO-STO superlattices with the general structure, X SmTO/[Y STO/X SmTO]$_{x4}$/LSAT, where X and Y are the thicknesses in number of unit cells of the SmTO and STO layers, respectively, and the whole structure is read from top (left) to bottom (right). The three superlattice layer architectures (X:Y) studied were 16:1, 10:1, and 10:5. This sample design allows the STO quantum well physics to be probed on both sides of its observed quantum critical point [28], and also at the 5 unit cell transition where magnetic correlations begin to propagate through the STO 2DEGs [44, 160]. Due to the coherency of the titania network throughout the superlattice, we hereafter refer to the quantum well thicknesses by the number of SrO planes in keeping with previous reports.

6.3 X-ray Absorption Spectroscopy

Figure 6.1 contains the polarization averaged or isotropic X-ray absorption spectra (a) and the X-ray linear dichroism (XLD) (b) for all four samples and a bare STO substrate. The data were collected in surface-sensitive total electron yield (TEY) mode because fluorescence yield XAS has been shown to poorly reproduce the true XAS spectra as derived from changes in absorption cross section [71]. This is particularly the case for early transition metals like Ti [72]. The measurement of the STO substrate was used to obtain a control Ti^{4+} absorption profile, and indeed the measured spectra matches well with previous reports [58, 172]. Similarly, the SmTO film was meant to provide a control of the Ti^{3+} spectra. However, as Fig. 6.1(a) clearly shows, the SmTO film and all SmTO-STO superlattices have spectra that closely resemble Ti^{4+}. This is not the result of some unusual Sm valence, but the known oxidation of the surface of rare earth transition metal oxide films [44, 173, 174]. From these previous reports, as well as the reflectometry refinements below, the surface oxidation in these materials extends roughly 2-3 nm from the surface. This constitutes the bulk of the $\sim$3-4 nm electron sampling depth calculated for similar perovskites [175]. Moreover, the TEY signal is preferentially weighted towards surface interactions because the probability of an excited electron's escape decays rapidly

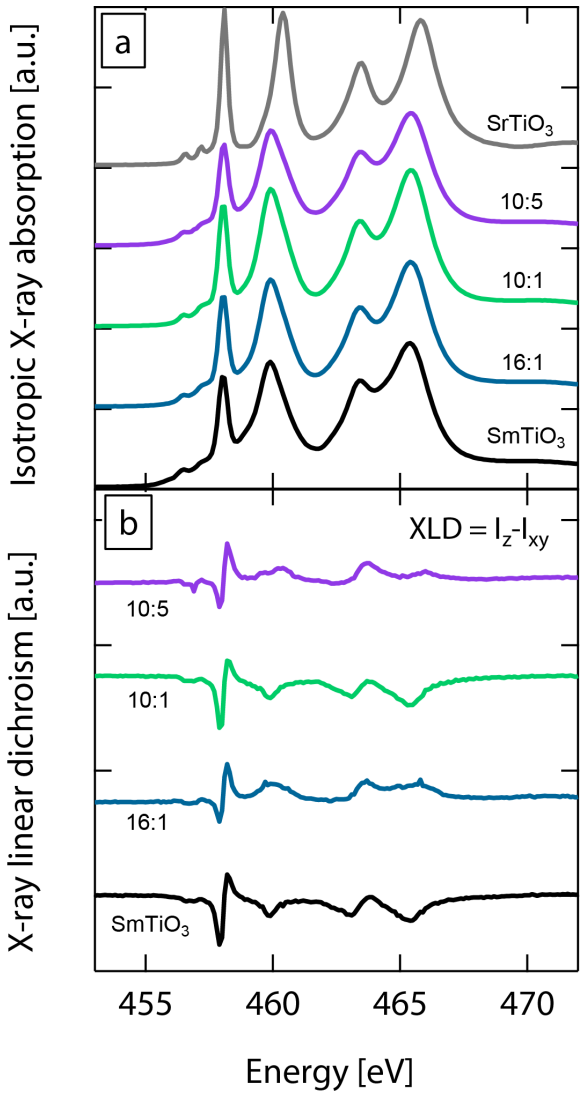

Figure 6.1: Total electron yield isotropic XAS (a) and XLD (b) spectra for a SmTO film, STO substrate, and three SmTO-STO superlattices. The labels X:Y correspond to the SmTO:STO layer architectures of the three superlattices as described in the main text.

with depth into the film. Therefore, it is only oxidized Ti^{4+} near the surface of the SmTO film and superlattices that is observed in the TEY spectra.

By extension, the XLD spectra in Fig. 6.1(b) also pertains primarily to the oxidized surface SmTO layers in each of the samples. A cursory comparison of the measured spectra with calculations and measurements from previous reports shows some similarity in the general line shape [172]. However, closer examination reveals the spectra in Fig. 6.1(b) are not a match for either axially compressed or elongated titania octahedra. Given that the local structure of the oxidized surface SmTO layers is unknown, the XLD spectra provide limited value in understanding orbital polarization of this surface layer without accompaniment.

6.4 Resonant X-ray Reflectometry of a $SmTiO_3$ Film

Nevertheless, knowledge about the surface oxidation in these samples was critical to selecting an appropriate model for the X-ray reflectometry data, and determining how to handle resonant atomic scattering factors in the buried layers. In general, the RXR data was refined using the software package ReMagX [52, 173] in which a layer model of the sample broken into unique profiles for its constituent elements. Each elemental profile was composed of multiple slabs

or layers (here, used interchangibly) each possessing a thickness, roughness, and atomic density. Off-resonant atomic scattering factors were pulled from the Chantler tables [69]. For Ti, on-resonant atomic scattering factors were determined by scaling the meaured XAS for each sample to the imaginary component of the anomalous scattering factor, f'', from the Chantler tables. The real component of anomalous scattering, f', was then calculated through the Kramers-Kronig (KK) relation between the real and imaginary terms [74]. Further details regarding this treatment of resonant scattering factors can be found elsewhere [52].

The calculated resonant scattering factors were only treated as fixed and accurate input for the surface slab in the Ti profile because of the depth-sensitivity of the TEY XAS mode. For buried Ti slabs, whether corresponding to a SmTO or STO layer, the calculated resonant scattering factors were used an initial value and then refined. Initial refinements used to determine a structural layer model and scattering factors was done under the assumption of isotropic scattering. These results were then used as semi-fixed input into anisotropic scattering models needed to fit the observed polarization asymmetry. This is elaborated upon below.

The 20 nm SmTO film was the first sample refined and its results were leveraged during subsequent refinement of the superlattices. Figure 6.2(a) displays

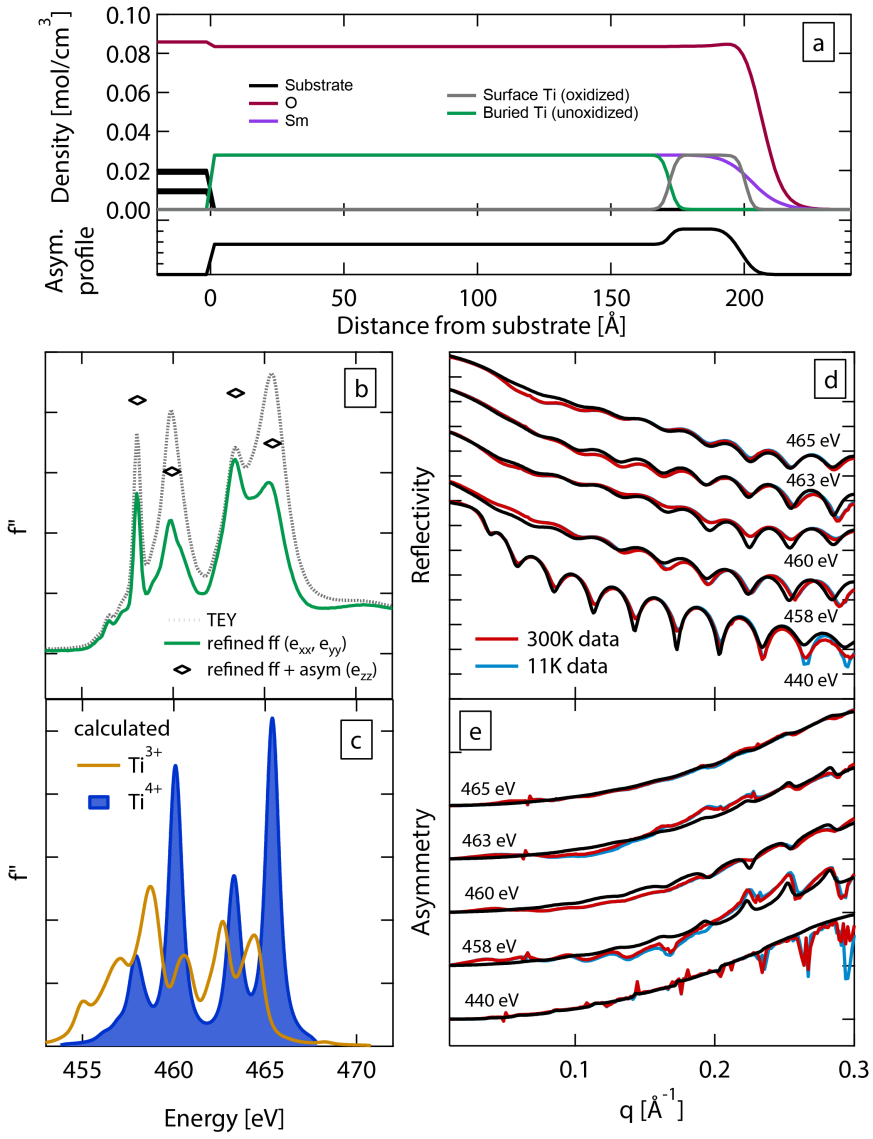

Figure 6.2: Refined layer structure (a) and scattering factors (b) from fit to reflectivity (d) and asymmetry (e) data for a 20 nm $SmTiO_3$ film. Black diamonds in (b) show the value of f'' along the z-axis. For panels (d) and (e), 300 K data is overplotted 11 K data for each energy, but in most cases changes with temperature are invisibly small.

the layer profile refined from fitting the reflectivity and asymmetry data in panels (d) and (e), respectively. The sample is broken up into three slabs or layers: the bottom layer is unoxidized SmTO, the middle layer is the oxidized SmTO near the surface of the film, and the top layer is mainly oxygen that creates an increasingly oxidized profile approaching the surface. The bottom layer, composed of $SmTiO_3$ in a confined 1:1:3 molar ratio, was refined to have an atomically sharp interface with the underlying substrate. The apparent abruptness of the substrate interface is in agreement with results from RXR on similar rare earth epitaxial films [173] and in this case likely results from a combination of the 50 x 100 μm X-ray beam spot size, careful pre-treatment of the substrates [27], and the high quality of the epitaxial growth.

The thickness and roughness of the bottom layer, which defines the transition from unoxidized to oxidized SmTO, was confined to be a single value for all three elements. However, the thickness and roughness of the middle layer, which defines the surface for Ti and Sm, were allowed to be unique for each element. This freedom results in a general surface structure that was found to be the same for all four samples despite independent refinements. Specifically, the oxidized Ti surface terminates first with a relatively small roughness. The Sm extends 2-3 $\mathring{A}$ past the Ti layer and terminates with a notably larger roughness. Finally, the oxygen layer is longer still owing to the oxidation of

the surface, but terminates with a roughness similar to that of the Ti layer. The independent reproducibility of this general profile gives high confidence in this physical picture of the surface. The profile may reflect varying lifetimes of the different atomic and molecular species present in the growth chamber after the nominal termination of the growth, or the relative migration of different atomic species during the surface oxidation process, or some combination of these effects. More detailed studies would be needed to precisely pin down the origin of this trend.

In addition to the sample's structural parameters, the resonant scattering factors for the buried Ti slab were also refined. These results are shown in Fig. 6.2(b) where the solid curve is the refined profile of the buried, unoxidized slab and the dashed profile is the scaled TEY spectra that also serves as the scattering factors for the oxidized Ti surface slab. The general shape of the refined spectra still looks Ti^{4+}-like because RXR measurements were only collected at the four Ti absorption peak energies, and therefore only the values at those positions can be refined accurately. The peak scattering factors were refined by fitting each absorption peak with a Lorentzian, subtracting that Lorentzian from the imaginary scattering factor profile, then adding it back multiplied by a refined scalar. The changes to the refined profile at values between the absorption peaks are due to the tails of the peak fit Lorentzians. The advantage of this approach

is that it allows the Kramers-Kronig relation between the real and imaginary scattering factors to be preserved simply by taking the KK transform of the peak fit Lorentzian and adjusting that by the same scaling parameter used for the imaginary component.

Though the shape of the refined spectra in Fig. 6.2(b) appears at first glance like Ti^{4+}, this is only because of the limited energies at which RXR was measured and the scattering factors could be adjusted. Taking a closer look at the profile shows that the e_g peaks are notably more suppressed than the t_{2g}. This again was a general pattern seen in the buried SmTO layer(s) of all four samples, arrived at through independent refinements. By comparing these refined results with either calculated Ti^{4+} and Ti^{3+} spectra or spectra from other references [176, 177], it can seen that these scattering factor adjustments are in fact an indication that the buried layers contain Ti^{3+} as seen in bulk SmTO. To understand how the refined values in Fig. 6.2(b) represent a Ti^{3+} valence state, consider the calculated Ti XAS profiles in Fig. 6.2(c). By overlaying the two profiles, it becomes easy to see that starting from Ti^{4+} and moving towards Ti^{3+} requires much larger reductions in the imaginary scattering factor for the e_g peaks than the t_{2g} peaks. Even better agreement with our refined adjustments to the SmTO scattering factors is found with experimental XAS spectra measured by Cao *et al.* [176] that may account for some effects of epitaxial strain not included in

the calculated spectra.

Through the refinement of the structural profile and scattering factors in Fig. 6.2(a) and (b), reflectivity curves were fit to the data shown in Fig. 6.2(d). Note that for all five energies, measurements were collected at 300 K (red) and 11 K (blue). Both data sets are plotted in Figs. 6.2(d) and (e), however, the changes measured with temperature are negligibly small in all cases. This means that although $SmTiO_3$ magnetically orders at low temperature [63], our measurements are not sensitive to this ordering. This is likely because $SmTiO_3$ films grown on LSAT have four-fold symmetric crystallographic domain variants [33] that average out any weak magnetic contribution to the signal.

6.5 Polarization Asymmetry and Orbital Occupation in a $SmTiO_3$ Film

Figure 6.2(e) plots the asymmetry between reflectivity curves measured in orthogonal linear polarization channels, defined here as $(R_\sigma - R_\pi)/(R_\sigma + R_\pi)$. This asymmetry is related to the linear dichroism effect arising due to a difference in absorption cross section for the various Ti d orbitals depending on their orientation relative to the polarization of the incident X-rays [178]. There-

fore, the observed asymmetry curves and the changes to the scattering factors needed to fit them contain information regarding the occupation of the various Ti d orbitals.

The general curving lineshape of the asymmetry curves, best seen in the off-resonant data set (i.e. 440 eV), is due to Brewster's angle that causes the pi polarized curve to decay towards total transmission as the incident angle approaches 45 degrees [179]. The polarization asymmetry signal coming from the material anisotropies is imposed on top of this Brewster's angle "background". Note that only RXR scans taken near the Ti absorption edges contain real polarization asymmetry because the absorption processes that the anomalous scattering factors quantify are described by Fermi's golden rule, which is a delta function in energy. This means that the deviations seen in the 440 eV asymmetry data are experimental error that comes from limitations in reflectivity resolution when trying to measure a signal over 6-7 orders of magnitude. Careful comparison of the asymmetry and reflectivity curves (Figs. 6.2(d) and (e)) reveals that all of the errors in asymmetry occur at q values corresponding to dips in the reflectivity curve where the signal is the smallest.

Due to the lack of temperature dependence in the signal (indicating a non-magnetic origin), fitting of the asymmetry was treated through a tetragonal scattering matrix, in which the f_{zz} component was allowed to be unique from

the $f_{xx,yy}$ components. More specifically, the structural model and in-plane scattering factors described above through isotropic scatter models were used as semi-rigid input and the f_{zz} scattering factors refined to fit the asymmetry data using a similar method as before. In practice this was done by adding a fake "asymmetry" element profile to the model. This asymmetry element had a profile almost identical to the Ti profile(s), $f_{xx,yy}$ equal to zero, and a non-zero f_{zz}. Because of the additive nature of the elemental contributions to the refractive index of a film layer (c.f. Eq. 2.5), this is mathematically equivalent to directly refining f_{zz} of Ti. The advantage in this approach is that is allows the asymmetry profile, which corresponds to a orbital occupation profile, to have roughnesses different than the underlying chemical profile.

The refined values for f_{zz} are indicated by open black diamonds in Fig. 6.2(b). Note that these values are all *larger* than the refined values of $f_{xx,yy}$. In a simple picture where the imaginary scattering factor profile is proportional to the unoccupied density of states [61], larger scattering factors reflect smaller orbital occupation. Therefore, the fact that f_{zz} refines to higher values than $f_{xx,yy}$ naively suggests the d^1 electron in Ti preferentially occupies the in-plane orbitals.

This in-plane orbital polarization in a SmTO film contrasts with expectations from the film's compressive strain state. Given the lattice parameters of LSAT

and SmTO [16, 36], epitaxial SmTO is under an average in-plane $\sim$1.0$\%$ compressive strain. In the absence of any competing interactions, this compressive strain would increase overlap of the in-plane d_{xy} orbitals and raise their energy relative to the other octahedral t_{2g} levels. In bulk SmTO, electronic structure calculations taking into account both the cooperative Jahn-Teller distortion and the R ion crystal field suggest two of the four Ti sites see a reduction in the in-plane orbital energy, while the other two sites see an increase [15]. To date, no studies we are aware of have calculated the expected orbital ordering for strained SmTO. However, a qualitative application of compressive strain in the xy-plane of Mochizuki and Imada's model suggests that both d_{xy} orbitals would be raised in energy relative to their unstrained values. Therefore it does not seem likely that an altering of the bulk orbital ordering pattern due to epitaxial strain is the explanation for the observed of in-plane polarization in these films. At present, an alternative explanation for our results is being discussed with collaborators and theorists.

6.6 Resonant X-ray Reflectometry of $SmTiO_3$-$SrTiO_3$ Superlattices

The refined layer structures for the three SmTO-STO superlattices are shown in Fig. 6.3. Determination of these profiles was accomplished using the following procedure. Initially, layer models assuming isotropic scattering were created from idealized versions of the sample stacks targeted during growth with a free surface to account for the known oxidation of SmTO. Buried SmTO and STO layers were initially constrained to have uniform thickness and roughness with the other layers of the same chemical composition. A combination of manually adjustment and Parratt algorthm calculations using this reduced set of model parameters enabled us generate approximate solutions to our reflectivity data set and to explore the relative sensitivity of various parameters.

For example, it was quickly determined that our models were to first-order insensitive to the exact roughness of the SmTO-LSAT interface as well as the SmTO-STO and STO-SmTO interfaces for the two superlattices with 1 SrO thick quantum wells. Refinements in which these values were allowed to refine results in the refined parameters hitting the lower bound, including if that bound was zero. This insensitivity can be understood by considering the very thin nature of the quantum wells in our superlattice structures that causes changes in these

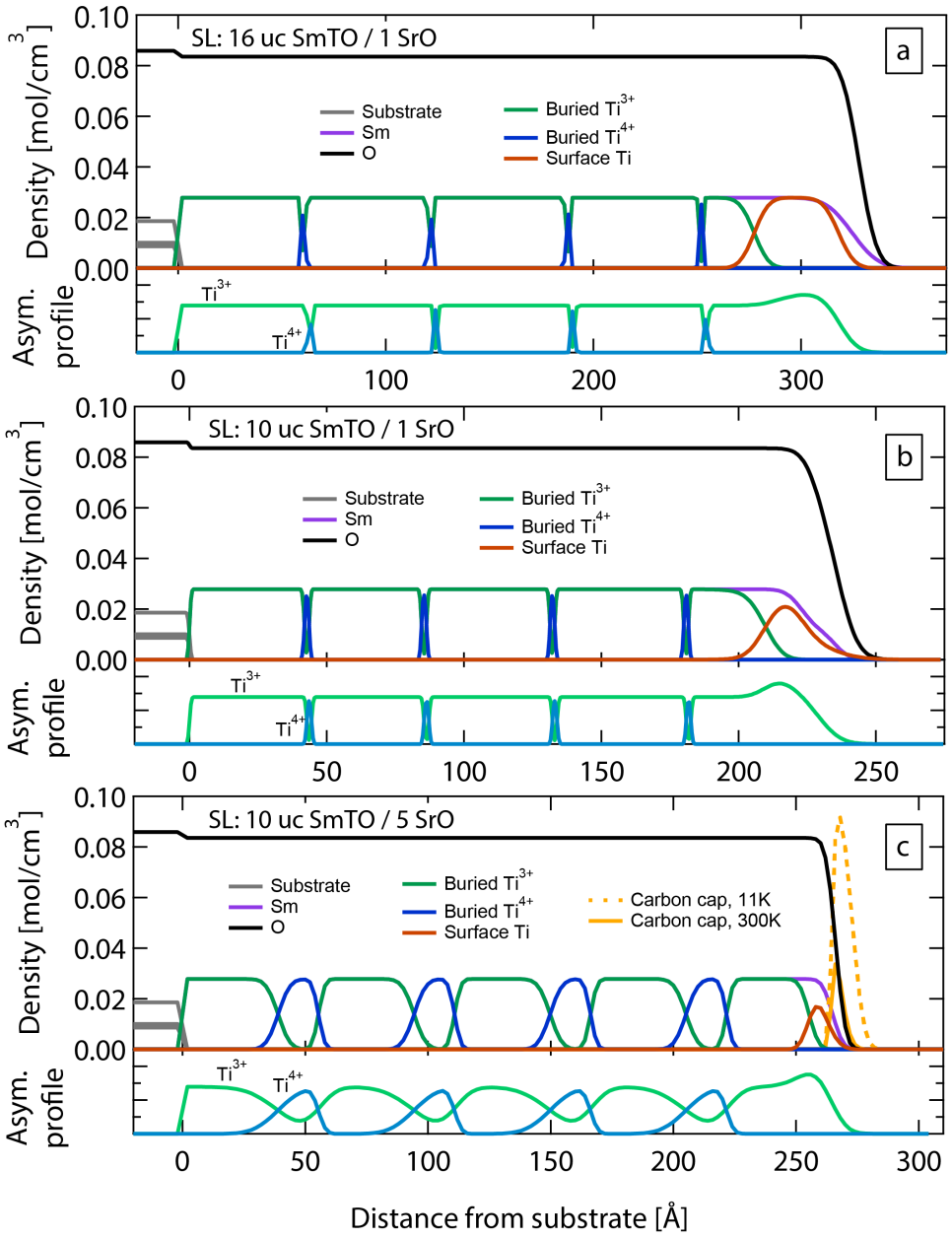

Figure 6.3: Refined layer structures for the 16:1 (a), 10:1 (b), and 10:5 (c) $SmTiO_3$-$SrTiO_3$ superlattices. These are the structures corresponding to the best fit models arrived at through the process described in the main text.

roughnesses to become apparent at high angles where signal-to-noise is poor. Therefore the buried interface roughnesses were fixed at 0.5 $\mathring{A}$ in order to keep the total number of refined parameters in more complex models to a reasonable value. This is the same value used for the substrate interface in the SmTO single layer film and is reasonable given the high epitaxial quality of these films and local atomic sharpness observed by electron microscopy probes. It is worth noting that periodically throughout the subsequent refinement process for these superlattices, these roughnesses were freed to see if in the phase space of better fitting models these values became important, but that was never found to be the case.

In the case of the 5 SrO superlattice, the SmTO-STO and STO-SmTO roughnesses were larger and refined to 3.9 and 2.0 $\mathring{A}$, respectively. However, this sample was grown in a separate growth run from the other two superlattices so it is unclear whether this difference in interface quality comes from thicker STO layers or lower sample quality.

In these initial refinements, the resonant scattering factors for Ti in the SmTO and STO layers were refined using the sample approach described in the case of the SmTO film. All layers of the same nominal composition were assumed to chemically identical and therefore were constrained to have one common set of scattering factors. Here we found that the refined profiles of the buried SmTO

layers looked almost identical to the buried portion of the SmTO film. In moving to more complex models, the reasonable assumption was made that the buried SmTO layers in the superlattice were identical to the buried SmTO portion of the thin film. Specifically this meant using the SmTO scattering factors refined for the buried portion of the SmTO film as fixed input into the superlattice models. Figure 6.4 compares the average of the freely refined SmTO scattering factor profiles from the three superlattices to the profile refined from the SmTO film.

The freely refined isotropic scattering factor profiles for STO layers also displayed remarkable similarities between superlattices. These profiles, the average of which is shown in Fig. 6.5, were generated in the same manner as the other refined scattering factors using the TEY XAS measurement from the STO substrate as the initial scattering factors. In all cases, there is a suppression of the t_{2g} peaks while the e_g peaks remain close to their original value. We believe this reduction in the t_{2g} absorption comes from the occupation of those orbitals by the charge transfer electrons induced by the electrostatic discontinuity between SmTO and STO [31]. Because of the uniformity between these freely refined profiles, an standard STO profile was generated by averaging the refined profiles and fixing the e_g peaks to be nearly their original value. This profile was then used as fixed input during the refinements of more complex layer models and when allowing for scattering factor anisotropy during asymmetry

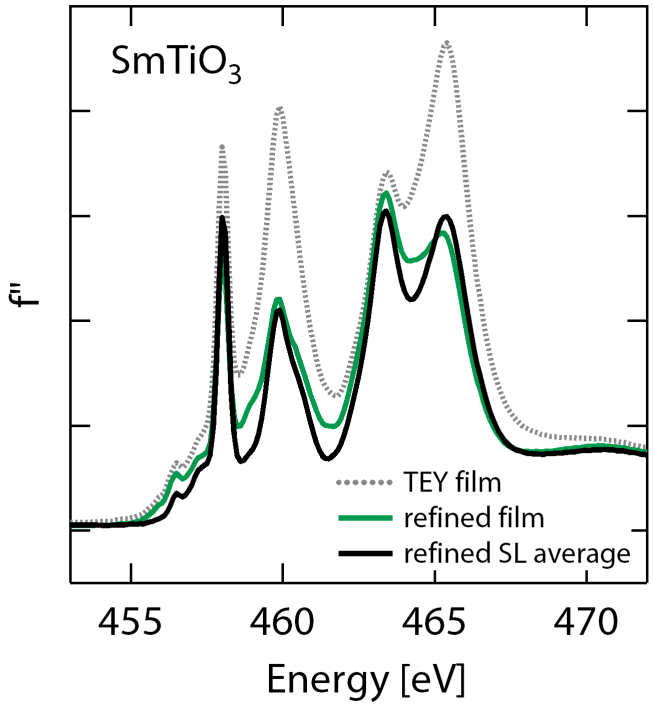

Figure 6.4: Average of the freely refined isotropic scattering factors of the buried SmTO layers in the SmTO-STO superlattices compared to the refined scattering factors and TEY measurements of the SmTO film.

refinements.

After developing standard scattering factor profiles for buried SmTO and STO layers in the superlattices, the model complexity was increased by allowing the individual SmTO layers to have a uniquely refined thickness value. The STO layers remained constrained to a uniform thickness. In the case of the two superlattices with 1 SrO thicknesses (i.e. 16:1 and 10:1), the rationale for constraining the STO layer thickness is the same as already described for the interface roughnesses. Namely, these STO quantum wells are roughly 1.5-2 $\mathring{A}$ thick so fractional changes in their roughness are on the order of tenths of an angstrom for which we have insufficient sensitivity to detect. Thus freeing these layers to have unique thicknesses provides the model with unwarranted degrees of freedom that only serve to tax the refinement algorithms. Nevertheless, such models were attempted and the results were in keeping with our expectations; the individual STO thickness values bounced around aimlessly, often ending up at one parameter bound of the other, with no discernible pattern. For the 5 SrO superlattice (10:5), the STO layers were temporarily given the freedom to refine unique thicknesses. However, the STO thicknesses consistently refined to the values within a few tenths of angstroms of one another, and manual adjustment of the thicknesses did not show any clear improvement over this uniformity. Therefore, these STO thicknesses were also kept constrained to limit

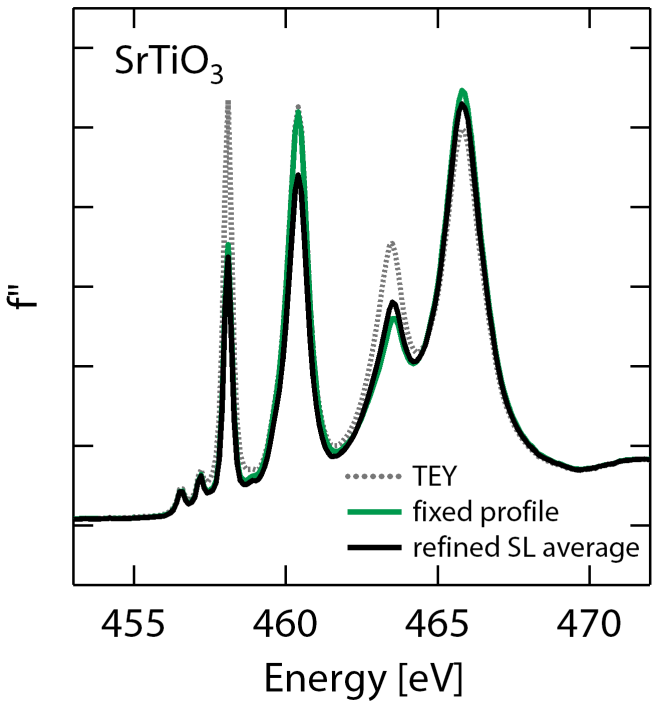

Figure 6.5: Average of the freely refined isotropic scattering factors of the STO layers in the SmTO-STO superlattices compared to the TEY measurements on an STO substrate and the fixed STO scattering factor profile used in subsequent models and asymmetry refinements.

free parameters in our asymmetry models. Note that while some of the STO layers in the 1 SrO superlattices appear different than others in Fig. **??**, this is an artifact of very thin layers and the resolution in which they are graphic sliced and exported.

Finally, it should be noted that throughout the modeling process just described the oxidized surface layers of the three superlattice samples were given total freedom with the exception of their scattering factors that were fixed to be the values measured from TEY XAS. The reason being that the absorption coefficients in our samples are large due to the fact that these measurements were collected at the absorption peak energies. This reduces the X-ray penetration depth and means our measurements (excluding the off-resonant 440 eV data set) are very sensitive to the chemical profile at the surface. Indeed, manual adjustment of surface layer parameters clearly shows a larger change in the reflectivity or asymmetry profiles than adjustments to the buried layers that are of a similar magnitude. Therefore, these parameters were given full freedom to try and maximize the goodness of fit.

6.7 Polarization Asymmetry and Orbital Occupation in $SmTiO_3$-$SrTiO_3$ Superlattices

Having optimized the superlattice layer models in an isotropic scattering approximation, the layer profiles were fixed and the asymmetry curves were fit using a tetragonal scattering matrix as was done for the SmTO film. Here two "asymmetry" element profiles were used to account for asymmetry in the SmTO and STO layer independently. The thicknesses of these layers were that of the underlying chemical profile, and the atomic density in the center of the asymmetry layers equal to that of the Ti atomic density such that this treatment of the asymmetry remained mathematically equivalent to the direct refinement of the Ti scattering factors. The interlayer roughnesses were initially freed for all samples, but found to be irrelevant for the 1 SrO superlattices as was the case with their chemical roughnesses. In the 5 SrO superlattice, the asymmetry roughness was found to be an exaggeration of the underlying chemical roughness.

Four different models for the asymmetry refinements of the superlattice scattering factors. First, the f_{zz} values for both the SmTO and STO layers were refined independently. However, this method was found to be fairly unreliable in that the refined value for a given calculation depended strongly on the starting values of those parameters. This is perhaps not surprising given the small

asymmetry signal, the instrumental noise in that signal, and the fact that these changes in f_{zz} constitute only a few percent of the total scattering length density of a layer.

Therefore, the assumption was made that the f_{zz} values of the buried SmTO in the superlattices film were the same as the SmTO film. This is basically just an extension of the previous assumption made concerning the isotropic scattering factors, namely, that the buried SmTO layers in the superlattices are chemically identical to the buried SmTO film. From there, three different models were devised for the STO f_{zz}. In the first model, the STO f_{zz} were allowed to refine. In the second model, the STO f_{zz} were fixed to be identical to the SmTO values (i.e. same as the SmTO film). Finally, in the third model, the STO f_{zz} were set to zero (i.e. all of the sample's asymmetry arises from the SmTO layers). These three models are compared for each of the three superlattices in Fig. 6.6-6.8.

Considering first the 1 SrO superlattices, like the SmTO film, these two superlattices showed very little variation in either the reflectivity or asymmetry data with temperature, and the 300 K and 11 K data sets are overplotted where collected. While the fits are poorer quality than excellent fits refined for the SmTO film, the samples are significantly more complicated and our fits are still very comparable with the fitting accuracy of other RXR reports in the literature [173]. In particular, the non-resonant 440 eV data are fit very well, indicating

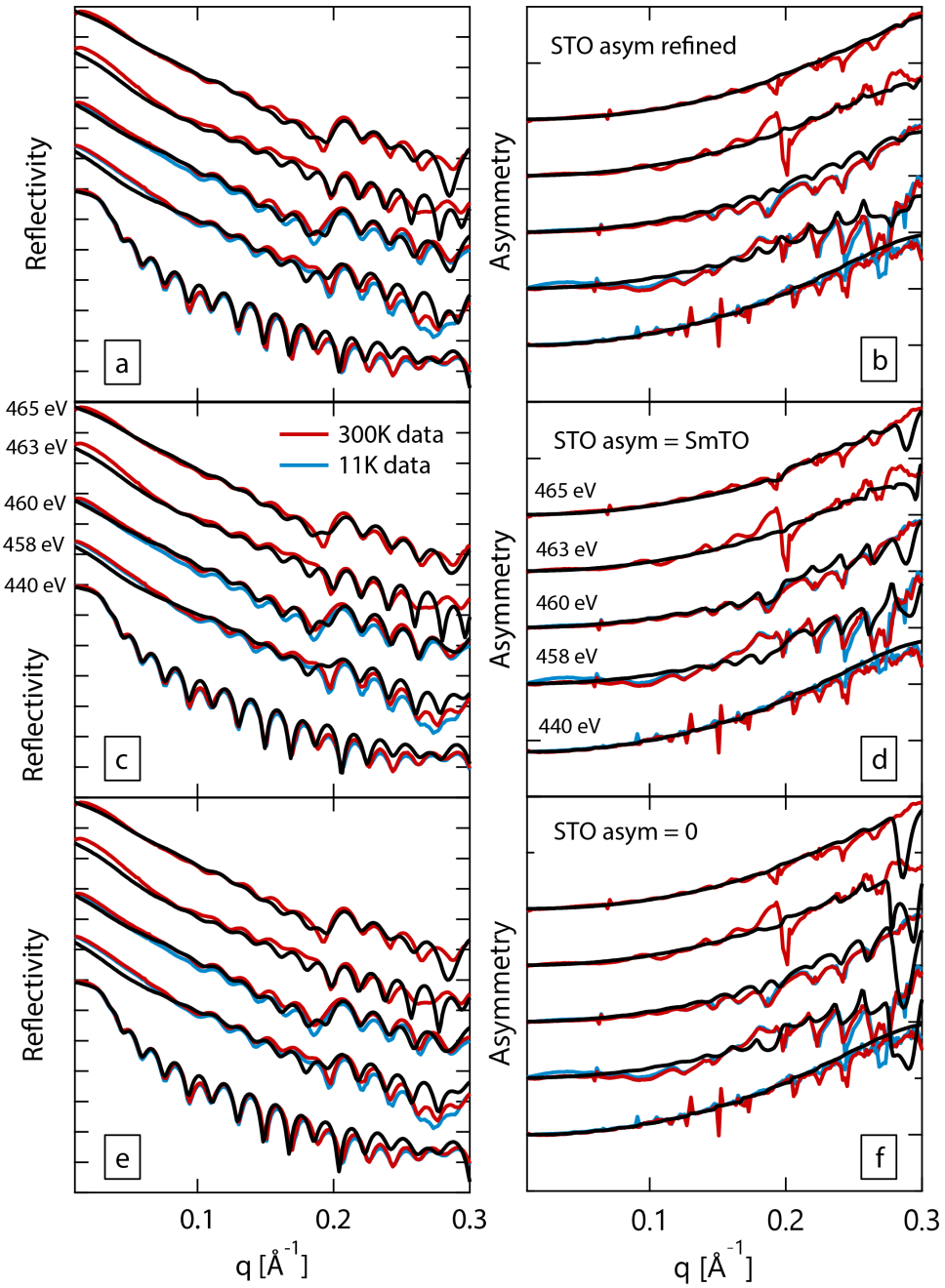

Figure 6.6: Fits to reflectivity and asymmetry data for the 16:1 $SmTiO_3$-$SrTiO_3$ superlattice. Models where the STO asymmetry parameters were refined (a,b), fixed to the SmTO values (c,d), and set to zero (d,e) are compared.

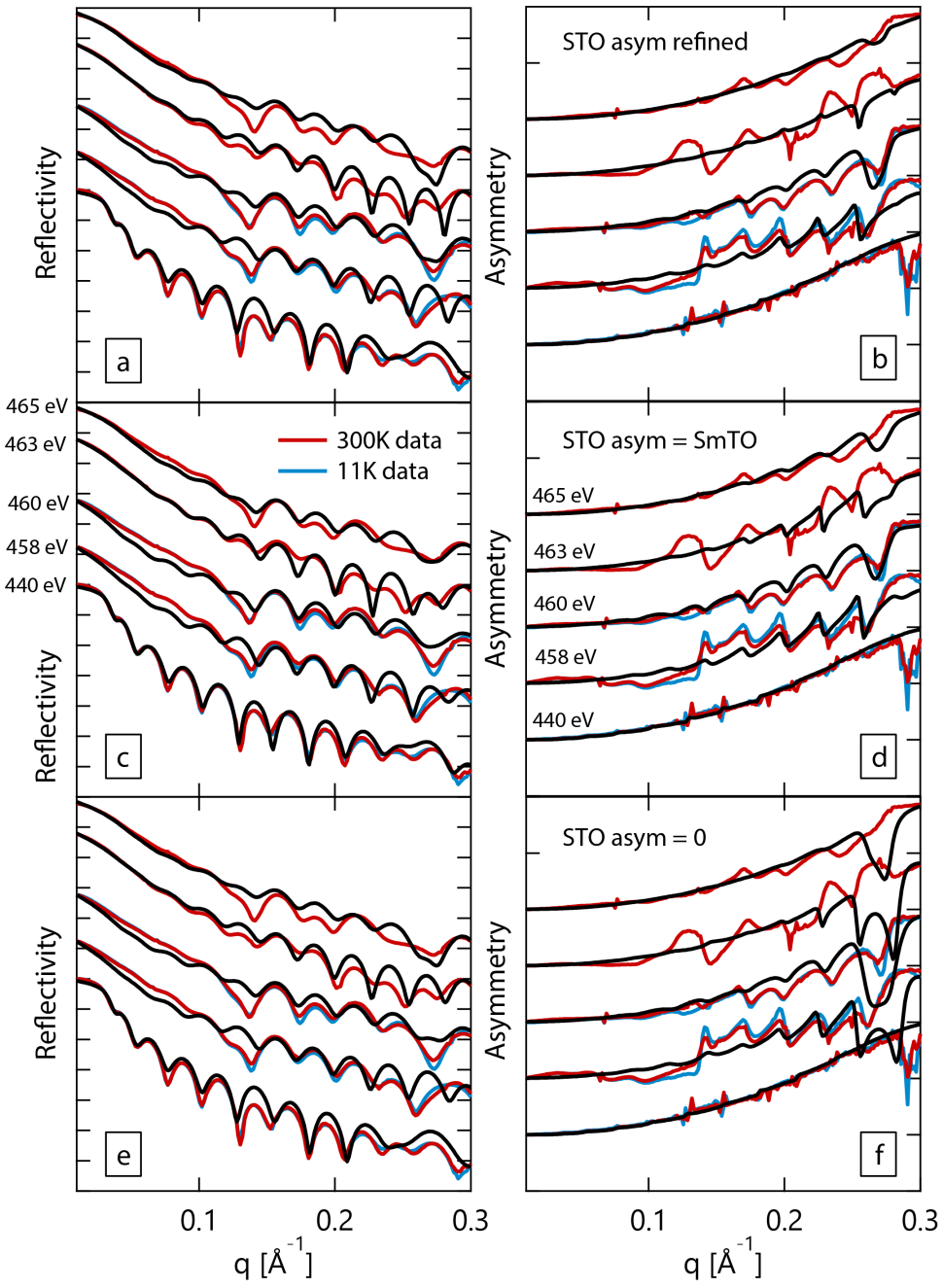

Figure 6.7: Fits to reflectivity and asymmetry data for the 10:1 $SmTiO_3$-$SrTiO_3$ superlattice. Models where the STO asymmetry parameters were refined (a,b), fixed to the SmTO values (c,d), and set to zero (d,e) are compared.

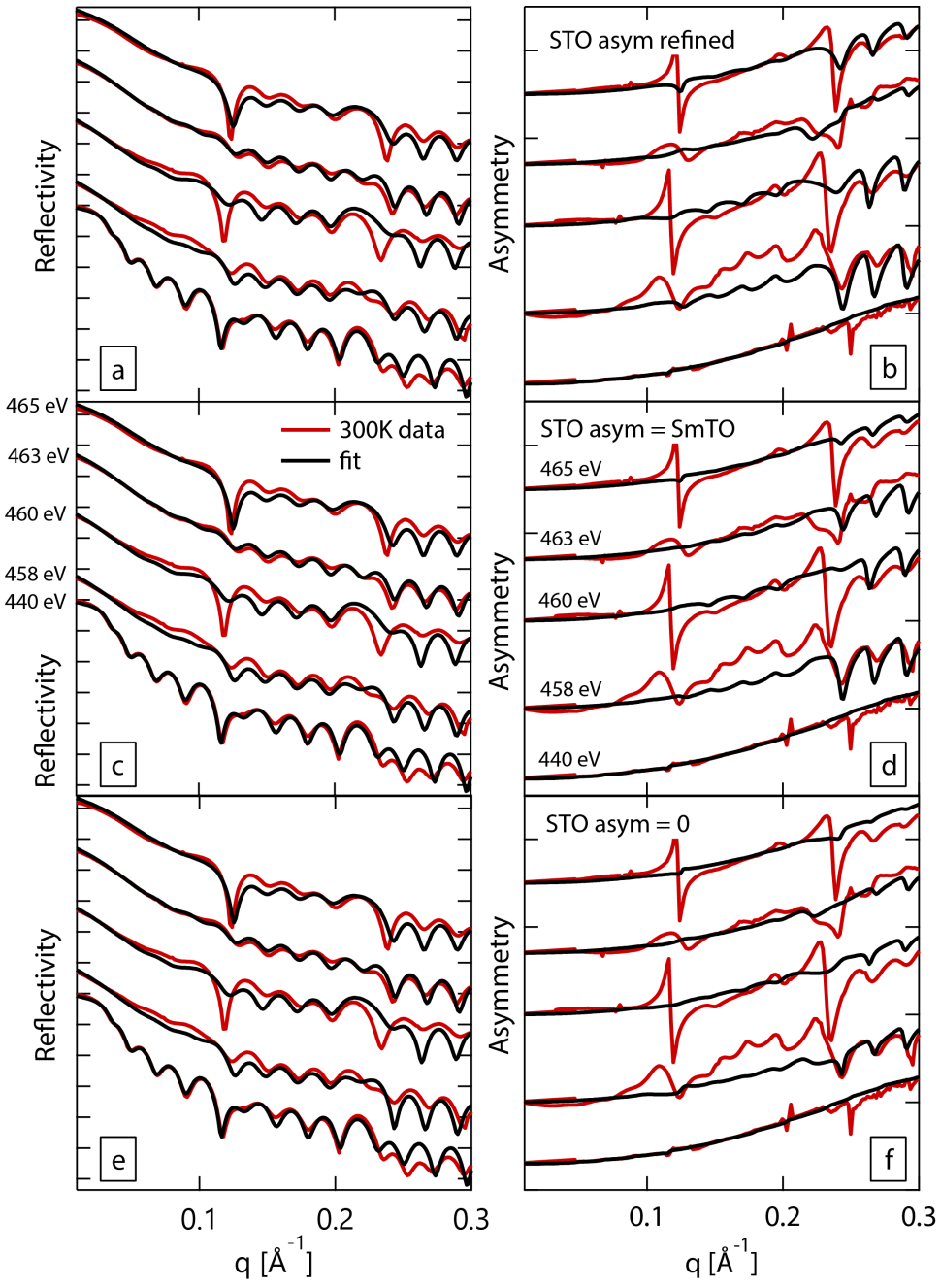

Figure 6.8: Fits to reflectivity and asymmetry data for the 10:5 $SmTiO_3$-$SrTiO_3$ superlattice. Models where the STO asymmetry parameters were refined (a,b), fixed to the SmTO values (c,d), and set to zero (d,e) are compared.

that fitting errors seen in the other energies arise mainly from subtitles in the Ti profile and scattering factors. For both 1 SrO superlattices, the first two STO asymmetry models are qualitatively identical. There are at least two reasons for this similarity. One is that the STO f_{zz}, when allowed to freely refine, end up as positive values of the same order of magnitude as the SmTO values. The other is that the STO layers in these samples are <2 $\mathring{A}$ thin and sensitivity to their absolute scattering factors is limited. That being said, we are sensitive to the models that create large changes in the periodicity of the sample, as demonstrated by the very poor fits when the STO f_{zz} are forced to zero. In this third model, both sample data sets show a clear dip in model fit around $q = 0.27$ $\mathring{A}^{-1}$ that is not present in the data. Therefore, while we do not have the ability to refine the exact STO f_{zz} values, we can say that under the reasonable assumption that the SmTO layers retain bulk-like orbital polarization the STO orbitals must be similarly polarized in the plane of the film.

The 5 SrO superlattice results are complicated by the presence of a temperature-dependent surface contamination layer that can be seen in Fig. 6.3. The presence changes with temperature in the non-resonant reflectivity data indicates must be a change in the structure of the sample, and not some intriguing phenomenon like magnetic or orbital ordering. This is because at this non-resonant energy contributions from anomalous scattering are negligi-

ble, and the Thomson scattering mechanism that is active is only sensitive to the total electron density of the atoms. Figure 6.8 displays only the 300 K data for simplicity of comparison with the other two, temperature-independent superlattices. While the quality of the reflectivity fits is equivalent to that of the 1 SrO superlattices, clearly something has been missed in the fitting of the asymmetry as none of the three models capture the data well. Dramatically increasing the STO f_{zz} by roughly an order of magnitude does generate larger amplitude features in the asymmetry curve fit. However, no model attempted was able to reproduce the discontinuity-like features in the e_g data sets (463 and 465 eV), which suggests something more fundamental is incorrect with our models.

6.8 Conclusions

In conclusion, we have used a combination of X-ray absorption spectroscopy and resonant X-ray reflectometry near the Ti L-edges to extract information about electronic symmetry breaking in SmTO films and heterostructures. XAS spectra collected in TEY mode revealed oxidation of the SmTO surface layer in all samples. Reflectivity data from a 20 nm SmTO film was fit well by a model that contains a buried SmTO layer with its expected Ti^{3+} valence beneath an oxidized surface. Refinement of the Ti scattering factors within a tetragonal

scattering matrix enabled the polarization asymmetry data of this SmTO to be fit accurately, and indicates an in-plane orbital polarization within the SmTO film. The results from the SmTO film were leveraged to simplify the refinement of SmTO-STO superlattices by assuming the buried SmTO layer within each superlattice acted as identical scatterers. Fitting of the 1 SrO superlattice asymmetry suggested the STO orbital polarization was similar in magnitude and sign to the SmTO barriers. However, the asymmetry curves in the thicker 5 SrO superlattice were not well fit by any of the models attempted here. The in-plane orbital polarization extracted here for the SmTO film and thin STO well superlattices contradicts simple expectation from a strain argument as well as more detailed electron structure calculations that predict the bulk SmTO orbital ordering. Additional work is needed to reconcile these discordant results, and that work is already underway.

Chapter 7

Conclusions and Future Directions

The studies presented here add to our collective understanding of Mott insulating thin films and particularly those interfacing a high electron density quantum well. In the case of thin STO quantum wells between magnetic rare earth titanate barriers, we used polarized neutron reflectometry and muon spin rotation to show that there is a critical well thickness (or electron density) below which the 2DEL electrons exhibit magnetic correlations. While the type of magnetism induced within the quantum well depends on the nature of the exchange interactions in the neighboring rare earth titanate, the critical thickness appears to be independent from it. Finally, this quantum well magnetism coincides with pseudogap formation in the SmTO/STO system and suggests a magnetic ori-

gin to the pseudogap along with strong parallels to bulk Mott insulators near a quantum critical point.

A focused study of thin GTO layers constrained between larger STO barriers revealed the existence of magnetic dead layers on the GTO side of GTO/STO interfaces. These dead layers create a finite-thickness effect in the bulk magnetometry signal that mimic suppression of the GTO moment as the GTO layer is thinned. However, depth-dependent PNR measurements indicate that the ferrimagnetism in the center of the GTO layers survives unperturbed by changes in Ti-O-Ti bond angle. This shows that in ferrimagnetic GTO, and likely other heavy rare earth titanates with similar magnetic responses (e.g. $DyTiO_3$, $ErTiO_3$), magnetic exchange interactions are not strongly coupled to electronic bandwidth.

Finally, by applying element-specific resonant X-ray techniques, we were able to probe electronic symmetry breaking in SmTO-STO films. Measurements on a SmTO film display a linear polarization asymmetry that is best fit by a model in which d^1 electron from Ti^{3+} preferentially occupies the in-plane orbitals. Despite contracting results from previous electronic structure calculations, independent refinements of SmTO-STO superlattices that arrive at a similar SmTO orbital preference for all samples studied lend credence to this picture. The precise origin of this observed orbital polarization is still under investigation.

While this work has shed light on a number of correlated phenomena in rare earth titanate thin films, there are still many unanswered questions. Some of these questions center around the critical electron density/well thickness that we found to be necessary to observe magnetic correlations in STO quantum wells. Though this critical point was found to be common to all the STO quantum well systems we have investigated, the mechanism underlying the transition to a magnetized well is still an open question. Is it truly a critical well thickness that creates significant overlap between the 2DEL wavefunctions at opposite interfaces and mediates magnetic exchange interactions? Or is it a critical spatial confinement of the total electron density that pushes the average electron-electron spacing past a threshold? How are these related to transport signatures of an electronic instability (i.e. lifetime divergence, pseudogap opening) at this critical point?

One way to start answering some of these questions is the fabrication and characterization of asymmetric GTO/STO/SmTO films. Given that GTO is a ferrimagnet that exhibits magnetic hysteresis loops and SmTO is an antiferromagnet, it should be possible to observe exchange bias when STO wells are sufficiently thin. The question then is: does one observe the same critical well thickness to turn on exchange bias that was seen in our previous studies? A study of this nature could begin with lower cost SQUID magnetometry on an

appropriate series of heterostructures to get a general picture of the magnetic behavior. If the results were promising, a combination of neutron reflectometry and AC susceptibility measurements could provide additional enlightening information about the depth-dependence and dynamics of the quantum wells' magnetic behavior.

Another more difficult approach is to develop an analogous material system with high-density 2DELs sitting at the interface of an insulting quantum well. It would be ideal if this system was also either a d^0 or low-spin d^6 system, such that the 2DEL electrons sit in relatively isolated orbital and the single band picture remains valid. These constraints, plus the additional requirements related to high quality film growth and interfaces, significantly limits the number of potential systems. One material family where this may be possible is the zirconates. At room temperature, $SrZrO_3$ (SZO) is an insulating d^0 compound with the distorted orthorhombic perovskite structure and an electronic band structure similar to STO [180]. The presence of tilted titania octahedra in the bulk and increased spin-orbit coupling from the 4d transition metal are notable differences from STO, but would also provide opportunities to test the effect of orbital bandwidth and spin-orbit coupling on some of these correlated phenomena. However, it may prove difficult to place a trivalent cation on the A-site. Typically, previous attempts at rare earth substitution in this system have focused on the

transition metal B-site to generate mixed-ion conductors [181], doping of the piezoelectric prototype Pb(Zr,Ti)O_3 [182], or alloying the pyrochlore structure for thermal barrier coatings [183]. It is unclear whether $A^{3+}Zr^{3+}O_3$ compounds are unstable or simply have not received much attention. Regardless, molecular beam epitaxy is well known to be a kinetically-controlled, non-equilibrium growth method [184] and therefore it may be possible to stabilize such materials even if solid state methods cannot.

In conclusion, STO quantum wells embedded within rare earth titanates have provided a fruitful phase space in which to explore nuanced electron correlation physics. While there are still many open questions in the titanate thin films, we have been able to shed light on the magnetic behavior induced in STO quantum wells and near STO/RTO interfaces. Moving forward, the development of other transition metal oxide analogues could provide insight from a new direction, though there are still a number of experiments in the STO/RTO family that could add to the discussion and understanding of these strongly correlated systems.

Appendix A

Growth and Characterization of Transition Metal Chalcogenides and an Intermetallic Skyrmion Host

A.1 Binary TMCs: $NbSe_2$ and WTe_2

Binary transition metal chalcogenides (TMCs) were grown as a stepping platform towards the more complicated ternary variants. These long-studied binary compounds have the general formula MX_2 where M is an element from the transition metal block of the period table and X is a chalcogenide (i.e. S, Se,

Te). Like graphite, TMCs possess a two-dimensional (2D) layered structure with van der Waals gaps separating adjacent layers [185]. The weak interlayer bonding means these materials can easily be thinned down to the monolayer limit and thus make excellent candidates for 2D electronics. However, unlike their metallic analogue graphene, TMCs are often semiconductors with tunable bandgaps ideal for optoelectronic devices [185, 186].

$NbSe_2$ consists of Nb atoms surrounded by a trigonal pyramid of Se atoms in what is known as the 2H or 4H polytype, depending on whether the layer stacking contains two or four adjacent layers [187]. The two $NbSe_2$ polytypes possess superconducting transitions at 7 K and 6.3 K for the 2H and 4H compounds, respectively [188]. 2H-$NbSe_2$ also undergoes a charge density wave transition at 33.5 K [189].

We grew crystals of $NbSe_2$ using the vapor transport method with excess Se as both a self-flux and transport agent [190–192]. Specifically, 0.5 g of stoichiometric $NbSe_2$ plus 1% excess Se was ground from high-purity elemental powders in an agate mortar and pestle for 15 min inside an argon glovebox. The powder was then loaded into a 15 cm long fused quartz ampoule with a 4 mm inner diameter and sealed under high vacuum, roughly 3 x 10^{-5} mbar. The ampoule was then loaded into a horizontal tube furnace with metal baffles inserted in one end of the tube and a combination of quartz wool and alumina

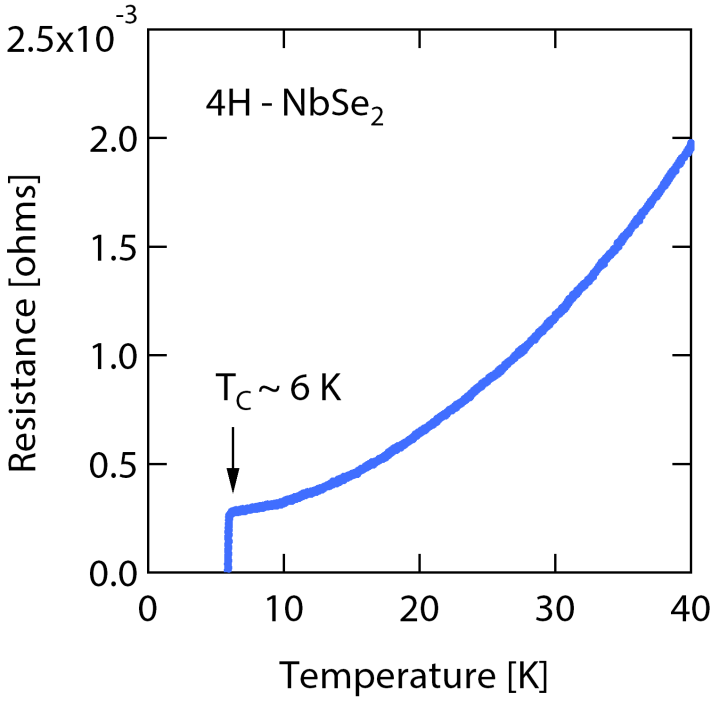

Figure A.1: Four point probe resistivity measurement taken on a 4H-$NbSe_2$ single crystal grown by vapor transport.

at the other. This asymmetry created a 30 K temperature gradient across the ampoule as measured using a thermocouple prior to the heat treatment. After placing the ampoule in the furnace, the furnace was ramped to 820°C at 10°/hr then held at 820°C for 168 hrs (1 wk). The sample was "furnace quenched" by turning off power to the elements and opening the clamshell furnace.

The resulting crystals had a fine needle morphology with the largest of them being slightly longer than 1 mm. Four point probe measurements, an example of which is shown in Fig A.1, revealed a superconducting transition at 5.9-6 K and no anomaly near 33 K, suggesting our crystals were the 4H polytype.

The other binary compound explored was WTe_2. Like $NbSe_2$, it is a 2D layered solid with van der Waals gaps. However, unlike the 2H or 4H polytypes discussed above, WTe_2 is of most interest when it crystallizes in the 1T' structure. This structure, where each W atom is surrounded by a distorted octahedron of Te atoms, has been predicted to lead to a large gap quantum spin Hall state [193] and shown to exhibit an almost titanic magnetoresistance [194]. These unique physical properties are derived from the 1T' band structure that is thought to have an inverted band structure giving rise to topologically protected edge states and similarly sized electron and hole pockets in the Fermi surface.

WTe_2 was grown using both the vapor transport method and a self-flux plus

centrifuge technique. For the vapor transport growths, bromine was used as the transport agent following Ref. [194]. Stoichiometric ratios of W and Te powder were mixed and ground in an argon glovebox, identical to the treatment of $NbSe_2$. After adding the powder to a fused quartz ampoule, a few microliters of bromine were pipetted into the ampoule with care taken such that the droplets had minimal contact with the sidewalls prior to hitting the powder at the bottom of the ampoule. This gives greater confidence that minimal bromine is lost while sealing the ampoule under 10^{-5} mbar vacuum.

Electrical resistivity ratio (i.e. R_{300K}/R_{4K}) was used as a proxy for crystal quality. By systematically varying the amount of bromine added to the reaction while keeping the amount of powder and ampoule volume constant, we were able to tune the resistivity ratio by almost two orders of magnitude. As shown in Fig. A.2, our best crystals were those used 3 μL Br_2/g of precursor powder, and compare extremely well with the results reported in Ref. [194].

Later, following reported improvement in crystal quality using a Te flux method [195], WTe_2 crystals were grown using this method as well. Specifically, high-purity W and Te powders were mixed in a 1:20 molar ratio in an argon environment. The precursor powder was then loaded into the bottom of a quartz ampoule followed by quartz wool that was pushed roughly halfway down the length of the ampoule, such that it was not in direct contract with

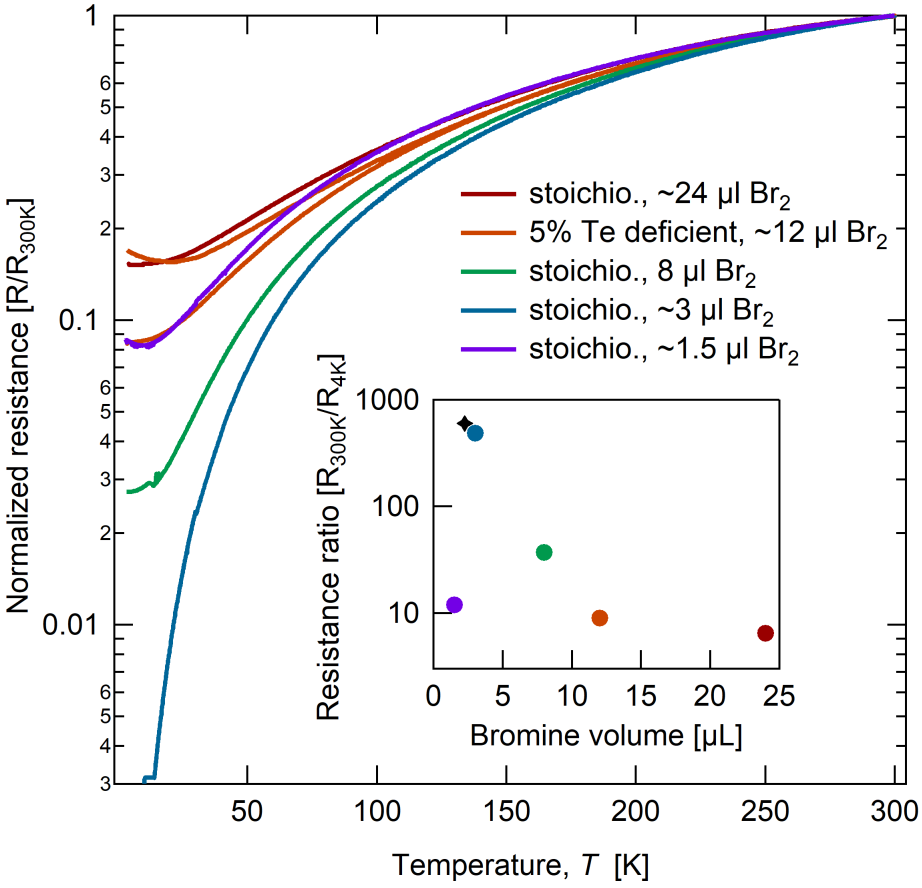

Figure A.2: Four point probe resistivity measurements taken on a 1T'-WTe_2 single crystal grown by vapor transport. Resistivity ratio is maximized at the optimum Br_2 concentration of 3 μL. The black diamond symbol in the inset represents the RR from Ref. [194].

the powder or the location where the ampoule was sealed. After sealing under 10^{-5} mbar vacuum, the ampoule was placed upright in a box furnace and heated to 825°C at 10°/hr, soaked at high temperature for 1 day, then cooled to 545°C at -2°/hr. When the temperature reached 545°C, the hot ampoule was removed from the furnace, inverted, and immediately placed into a metal-tubed centrifuge to drain the still molten excess Te from any crystals that had grown within the melt.

The few flux-grown WTe_2 crystals measured for electrical transport had a resistivity ratio around 25, that improved to 65-70 upon annealing at ∼415°C for 2 days. This is considerably lower than values reported in Ref. [195] and even our best vapor transport grown crystals. However, only two batches of flux-grown WTe_2 were made and no system parameters were optimized since the project focus had shifted to ternary TMC compounds.

A.2 Ternary TMC: $NbIrTe_4$

Ternary TMCs can also form layered, van der Waals compounds suitable for integration into 2D electronic devices. Generally speaking, these compounds possess a wider variety of molar ratios and crystal structures than their binary counterparts [196, 197]. However, we were focused on systems that were sim-

ply a doubling of the binary chemical formula, $MM'X_4$, where M and M' are unique transition metal elements. Many of these compounds have been shown to preserve the 1T' local environment seen in WTe_2 and thus preserve some elements of its exciting band structure [198, 199].

The work was further motivated by predictions from recent electronic structure calculations [200]. In their calculations, Liu *et al.* evaluated four $MM'X_4$ compounds and predicted the same quantum spin Hall ground state for monolayers of these materials as was previously suggested for WTe_2. Moreover, when these materials were considered in the bulk form, the authors found that the stacking of multiple layers caused a loss of crystallographic inversion symmetry and resulted in the formation of either Type-I or Type-II Weyl semimetals depending on the van der Waals gap size.

We used $NbIrTe_4$ as a starting point for our study of these materials. Nearly phase pure polycrystalline powder was produced following a procedure similar to that reported by Mar and Ibers [198]. First, high purity elemental powders were ground together in a 1:1:4 Nb:Ir:Te molar ratio inside an argon glovebox. These were added to a fused quartz ampoule and sealed under 10^{-5} mbar vacuum as was done for the binary compounds. The ampoule was placed upright inside a box furnace, heated to 500°C and held one day, raised to 800°C and held one day, raised to 1000°C and held for 12 days, then cooled down to room

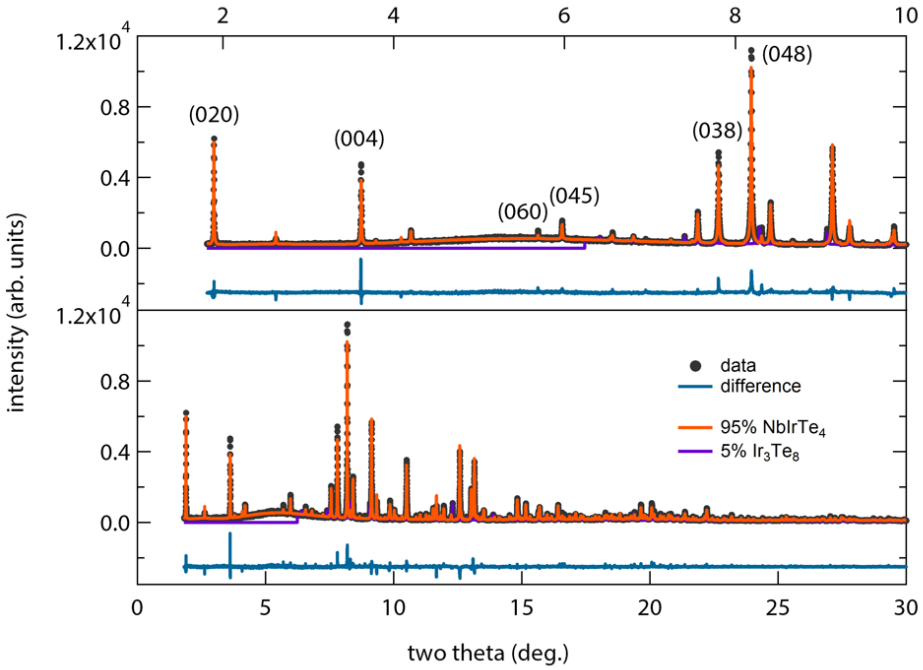

Figure A.3: Synchrotron powder X-ray diffraction data and Rietveld refinement of $NbIrTe_4$ powder. Data collected from Argonne's 11-BM beamline. Refinement courtesy of Dr. Geneva Laurita.

temperature over 1 day. The resulting powder was analyzed with both lab and synchrotron X-ray diffraction. Refinement of the synchrotron data, shown in Fig A.3, reveals the presence of $\sim 5\%$ of the impurity phase Ir_3Te_8. Analysis of cation site occupancy from Rietveld refinement suggests a 1.1:1 Nb:Ir ratio. Both of these results arse consistent with the findings of Mar and Ibers who saw small amounts of Ir_3Te_8 and $NbTe_4$ in their reacted powder and an off-stoichiometry Nb:Ir ratio of 1:1.2 [198].

For crystal growth, both vapor transport and Te flux methods were attempted. However, even when starting from the nominally phase pure powder, all vapor transport growth attempts met with failure owing to the additional complexity from the second metal cation and the correspondingly larger set of stable binary intermetallics. Better success was met with growing crystals from a melt of excess Te flux. In fact, two separate and repeatable routes based on Te flux were verified to produce $NbIrTe_4$ single crystals.

The first route utilizes the reacted $NbIrTe_4$ powder just described as starting material. That powder is reground in an inert argon atmosphere and then cold pressed into a pellet at 45 kpsi. The pellet is then loaded into a fused quartz ampoule with 10% excess Te by mass, and the whole ampoule sealed under high vacuum. The ampoule is then loaded upright into a box furnace where it is heated to 500°C, held 1 day, heated to 800°C, held 4 days, then slowly cooled to room temperature at -10°C/hr. Like the example shown in Fig. A.4, most of the crystals had an elongated platelet morphology with the longest axis parallel to the crystallographic a-axis and the thinnest dimension parallel to the 2D layer stacking. Resistivity ratios from transport measured along the a-axis were $\sim$10, again comparable with previously reported results [198], and cation ratio was determined to be near stoichiometric from energy dispersive spectroscopy.

The second route for $NbIrTe_4$ single crystal growth is considerable faster as

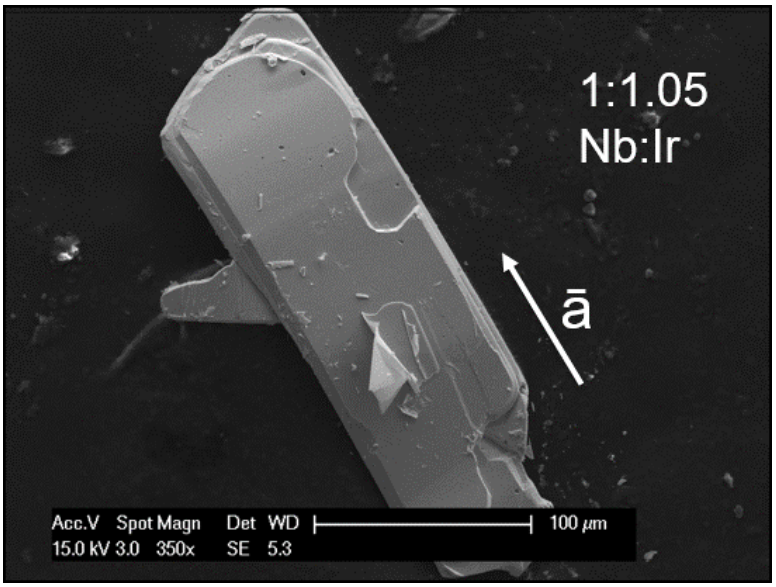

Figure A.4: Scanning electron micrograph of a $NbIrTe_4$ crystal grown from reacted ternary powder using the Te flux method. Text displays the approximate Nb:Ir cation ratio as determined from energy dispersive spectroscopy.

it requires only elemental powders, rather than the pre-reacted $NbIrTe_4$ powder. It is also directly analogous to the WTe_2 crystal growth described in the previous section. To begin, high purity Nb, Ir, and Te powders are mixed in a 1:1:10 molar ratio and ground together in a dry argon atmosphere. The mixture is then loaded into the bottom of a fused quartz ampoule, quartz wool is wedged into the ampoule halfway down it's length, and the whole ampoule is sealed under high vacuum. The ampoule is then placed upright in a box furnace and heated to 1000°C at 10°/hr, held at 1000°C for 1 day, then cooled to ∼700°C at -2°C/hr. At ∼700°C, the hot ampoule is pulled from the furnace, inverted, and centrifuged to drain the molten Te to the opposite end of the ampoule.

Figure A.5 shows an electron micrograph of a $NbIrTe_4$ crystal grown from elemental powders for comparison with Fig. A.4. In both cases, the crystal morphology is the same. However, note the difference in image scales and sizes of the two crystals. The crystal grown directly from elemental powders is roughly twice as large as that from reacted powder. Although this is only one crystal from each processing route, it is representative of the general trend that the elemental powder route produced notably larger crystals. Roughly speaking, the largest crystals grown via the reacted powder synthesis route were ∼1 mm to 2 mm in length, while the elemental powder route regularly produced crystals as long as ∼3 mm to 4 mm. This may simply be due to the large difference

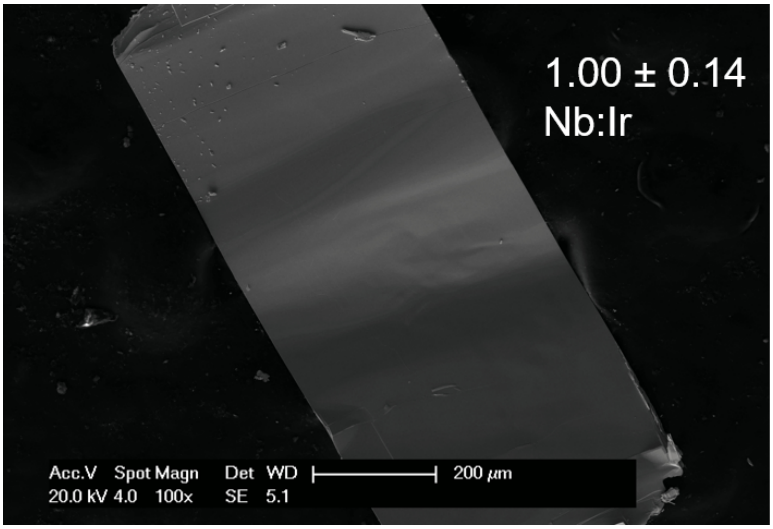

Figure A.5: Scanning electron micrograph of a $NbIrTe_4$ crystal grown from elemental powders using the Te flux method. Text displays the average Nb:Ir cation ratio as determined from energy dispersive spectroscopy measured on five samples.

between the amount of excess Te flux used in the two different methods, but no experiments were ever performed to probe this relation.

Regardless of growth method the resistivity ratio for our $NbIrTe_4$ remained of order 10. In addition to those zero field resistivity measurements, magnetoresistance sweeps were also collected given $NbIrTe_4$'s similarity to WTe_2 and that compound's large magnetoresistance response. Figure A.6 compares the magnetoresistance response of $NbIrTe_4$ and WTe_2 grown by analogous Te flux and centrifuge methods. The large magnetoresistance response seen by Ali *et al.* is clearly present in our WTe_2 samples. On the other hand, there is only about a 40% increase in the low temperature resistivity in our $NbIrTe_4$. This could be related to the fact that our WTe_2 crystals appear to have a higher overall crystalline quality as judged from their lower resistivity and larger resistivity ratio, which in turn may be related to cation site disorder in the ternary compound. Alternatively, the smaller magnetoresistance in $NbIrTe_4$ could be the result of the electronic band structure shifting away from the unique Fermi surface predicted for WTe_2, where the electron and hole pockets had almost precisely the same volume supposedly allowing for its large magnetoresistance [194].

In an attempt to test this experimentally, $NbIrTe_4$ batches were grown with an intentional deviation in the Nb:Ir precursor ratio. Specifically, Nb-rich and Ir-rich batches with Nb:Ir=1.3:1 and Nb:Ir=1:1.3, respectively, were made fol-

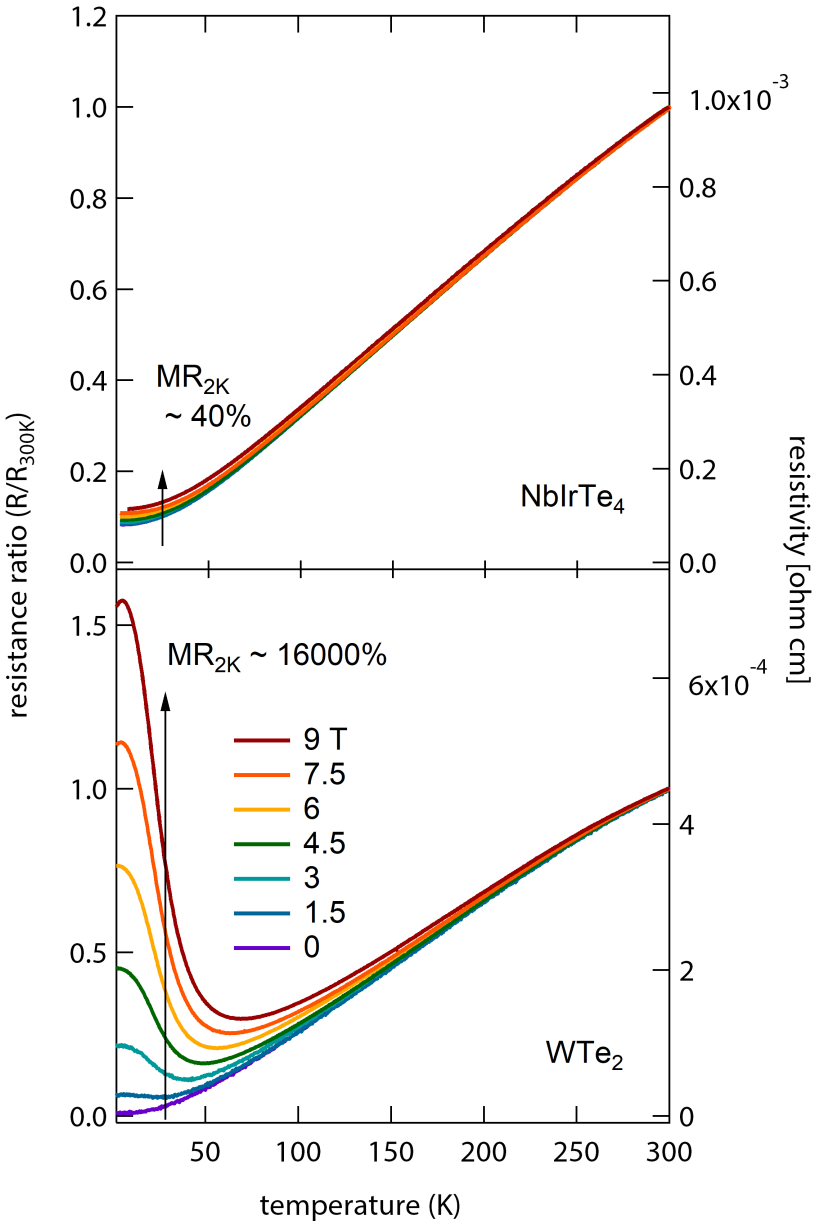

Figure A.6: Magnetoresistance comparison of flux-grown $NbIrTe_4$ and WTe_2 starting from elemental precursors. Both samples were annealed in vacuum for 48 hrs after growth and prior to measurement.

lowing the elemental powder procedure above. In the Nb-rich case, $NbIrTe_4$ were grown, but energy dispersive spectra showed that the excess Nb did not incorporate into the crystals and the Nb:Ir ratio was within error of unity. The Ir-rich case failed to produce any $NbIrTe_4$ crystals, instead forming a combination of Ir_3Te_8, $NbTe_4$, and Te crystals. While this does not answer the question above regarding the origin of $NbIrTe_4$'s smaller magnetoresistiance relative to WTe_2, it does reveal that the system's bandstructure has limited ability to be tuned through cation substitution.

There are a number of directions one could take this project moving forward. On the synthesis end, it would be interesting to try to tune the bandstructure through substitution of Se onto the Te site to see if some of the lost magnetoresistance can be recovered. Corresponding electronic structure calculations for both the stoichiometric ternary and variants with cation or anion substitution would be very insightful in this regard and could comment on the worth of these various synthesis options. Probably more exciting however would be angle-resolved photoemission spectroscopy (ARPES) measurements on the already in hand $NbIrTe_4$ single crystals to look for signatures of the Weyl state. If successfully determined to be a Weyl fermion, then the predictions of Liu *et al.*[200] could be examined by either applied uniaxial pressure during the ARPES measurement (if the interlayer spacing is too large) or intercalation of

H, H_2O, or even Li prior to ARPES (if the interlayer spacing is too small).

A.3 Skyrmion Host: FeGe

Unrelated to the previous TMC projects, the intermetallic skyrmion host FeGe was grown for a series of collaborators. Skyrmions, named after the physicist Tony Skyrme who developed the initial mathematical concept [201], are topological solitons that resemble single particles in their spatial localization and quantized charge. Within condensed matter, skyrmions can be found in a wide range of material systems from Bose-Einstein condensates to quantum Hall magnets to certain liquid-crystals [202]. A useful way to envision a skyrmion is as a protected defect within an otherwise continuous field. This protection arises from the discontinuous or quantized nature of their energetic states, and is considered highly attractive for a variety of technological applications as it vastly improves the particle's stability against otherwise perturbing fluctuations.

Magnetic skyrmions were identified early on as one manifestation with a clear and exciting technological application – as individual, nanoscale magnetic memory bits for high-density, non-volatile data storage [203]. The magnetization of these tiny memory bits can be manipulated using spin polarized currents, in much the same way as ferromagnetic (FM) domain walls in more conven-

tional spintronic systems (e.g. spin valves). However, compared to current densities required to move domain walls (DW), only extremely small current densities, roughly 10^5 times smaller, are needed to drive skyrmion motion [204, 205]. This means that skyrmion-based memory storage systems have inherently lower energy consumption than technologies based upon domain wall motion.

Magnetic skyrmions come in a variety of sizes and textures as depicted in Fig. A.7, from a handful of atoms to "hedgehogs" spanning 10's of nanometers, yet they can all be described as a point-like reversal of magnetization in the center of a region of chiral spins. Despite their different appearances, magnetic skyrmions all share the common requirement of broken inversion symmetry. This broken inversion symmetry adds an antisymmetric exchange term known as the Dzyaloshinskii-Moriya interaction (DMI) to the total exchange energy of the system. The DMI term can be expressed as $D_{ij}(S_i \times S_j)$ where D_{ij} is the DM vector that quantifies the strength and chirality of the interaction between neighboring spins S_i and S_j. The vector product DMI term favors orthogonal alignment of S_i and S_j. However, because DMI generally acts as a perturbation on the symmetric exchange term, it tends to create canted magnetic structures and, in the case of skyrmions, their characteristic spiral. In bulk crystals, broken inversion symmetry requires a non-centrosymmetric crystallographic space group. For FeGe specifically, the B20 phase has the space group $P2_13$ (No. 198)

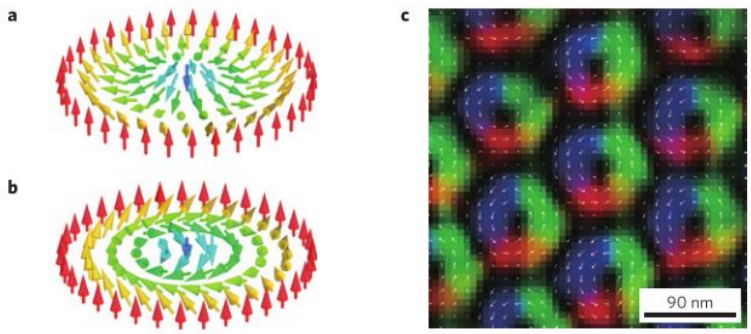

Figure A.7: So-called hedgehog (a) and spiral (b) two-dimensional magnetic skyrmions. Image (c) is a Lorentz micrograph illustrating how it is possible to observe skyrmions and their motion in real space. Adapted from Ref. [203]

[206].

FeGe crystals in the B20 structure were grown using iodine vapor transport from pre-reacted FeGe powder and iodine in a 130:1 mass ratio. The precursor FeGe powder was generated by arc melting pieces of Fe and Ge (99.999% Sigma Aldrich) together under an argon atmosphere. The arc melted pellet was flipped and remelted at least 12 times to increase mixing and homogeneity, and subsequently annealed under vacuum in a sealed quartz ampoule at 580°C for a period of 7 days. This procedure resulted in FeGe powder that was ∼25% B20 and ∼75% B35 as determined by Rietveld analysis of x-ray powder diffraction data. The powder and iodine (99.999% Alfa Aesar) were then sealed in one end of a quartz ampoule under vacuum below 5 x 10^{-5} mbar. The ampoule was

placed in a three zone tube furnace with the precusors held at 570°C, the middle zone at 565°C, and the far end at 570°C for 14 days. The middle portion of the ampoule, with smooth side walls, was chosen to be the cold deposition region to reduce the number of nucleation sites. In subsequent crystal growths, small ($<$100 μm diameter) B20 crystals were placed in the middle of the ampoule to act as nucleation sites.

Successful crystal growth using this procedure resulted in B20 crystals roughly 250 μm in diameter with a truncated octahedron morphology. Despite attempts at longer crystal growths, crystals larger than this were not able to be grown. This is in keeping with previous results from the literature [207] and is likely due to an unoptimized relation between powder mass, ampoule volume, and iodine precursor, though competition with the stoichiometric polymorph B35 may also play some role. The B20 phase of these crystals was confirmed via single crystal x-ray diffraction, which determined the space group, and SQUID magnetometry, which confirmed an ordering temperature in agreement with previous results [208]. An example of the crystal morphology and magnetization is shown in Fig. A.8.

These crytals were then used as part of a proof-of-concept experiment as a potential magnetocaloric material in collaboration with Josh Bocarsly and Prof. Ram Seshadri. Using a newly developed method requiring only a vibrating sam-

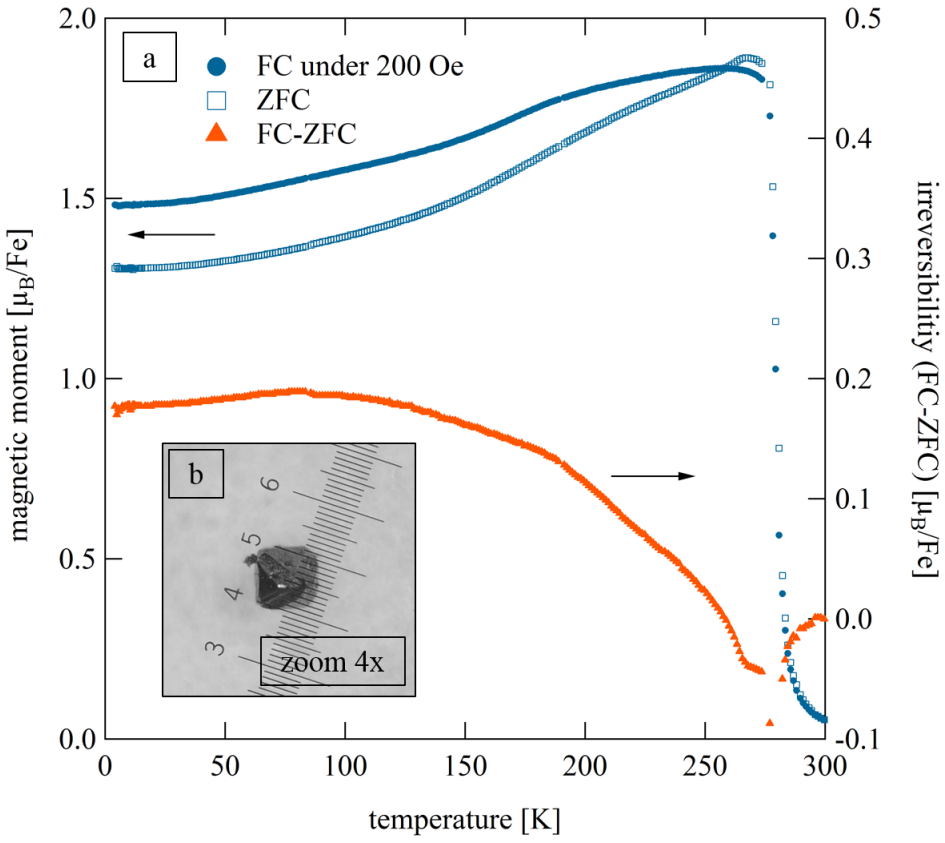

Figure A.8: SQUID magnetometry measurements on an FeGe single crystal. Inset shows an optical micrograph of the crystal morphology. Scale bar is in mm.

ple magnetometer, the magnetic entropy change of FeGe and $Co_8Zn_9Mn_3$ were mapped out as a function of temperature and field. This entropy change is proportional to the heat that can be extracted upon each magnetocaloric cycle and thus is a critical value for determining the refrigeration efficiency. While neither material performed better than current industry standards, the study established this new method as a high throughput means of analyzing future magnetocaloric candidates.

A considerable body of literature regarding the skyrmions in both bulk [209] and thin film [210] FeGe already exists. In thin films, a combination of high crystalline quality and epitaxial strain are able to stabilize skyrmions in wider temperature and magnetic field phase space than is found in the bulk [211]. However, the stable skyrmion temperature range remains below room temperature, limiting it's applicability in novel computer memory technology. Moving forward, one interesting experiment would be to grow FeGe on a substrate or buffer layer of a heavy transition metal (e.g. Pt, Ir) with large spin-orbit coupling (SOC). In other thin film skyrmion systems, neighboring heavy metal layers with large SOC have been shown to increase the net Dzyaloshinskii-Moriya interaction in the system and stabilize skyrmions at room temperature [212]. Though this strategy has only been applied to simple ferromagnetic layers like Fe or Co thus far, the interfacial DMI interaction only requires the non-SOC layer to have

itinerant spins near the interface and therefore should be applicable to materials like FeGe. The growth of such heterostructures would likely be difficult1, but success here could lead stabilization of skyrmions at room temperature or higher and lead to a technologically viable skyrmion platform.

Appendix B

Evidence of a Monoclinic Distortion in $SmTiO_3$ Films

X-ray resonant magnetic scattering experiments were performed with the intention determining the magnetic structure of strained SmTO thin films. These experiments were conducted at at Argonne National Laboratory's Advanced Photon Source using beamline 6-ID-B in collaboration with Dr. Zahir Islam. Figure B.1 shows a series of L-scans taken through the (3/2 -1 3/2) reflection taken on a 20 nm thick SmTO film. This position corresponds to a reported bulk magnetic reflection [63], but is here indexed in a pseudo-cubic reference frame. While there is a weak reflection at this position, it does not display any no-

table change in intensity across the two Neel temperatures, suggesting perhaps a non-magnetic origin. This hypothesis is supported by L-scans taken at 5 K for three energies across the Sm L_3-edge shown in Fig. B.2 that reveal a similar independence of the peak intensity from X-ray energy.

Together these data point towards a non-magnetic origin for this observed (3/2 -1 3/2) reflection. Light can be shed on the nature of this reflection by considering prior work on orthorhombic perovskite films growth and strain accomodation. It has previously been shown that many such orthorhombic perosvkite films undergo a symmetry-lowering transition from $Pnma$ to $P2_1/m$ when grown compressively-strained to substrates with cubic symmetry [213]. $SmTiO_3$ grown epitaxially on LSAT fits this description with an average 1% in-plane compressive strain. In the $P2_1/m$ space group, structural reflections at the (3/2 -1 3/2) are no longer forbidden. Calculations using a strained crystal structure with monoclinic symmetry suggest the reflection at (3/2 -1 3/2) should be three orders of magnitude smaller than the most intense structural peaks from the film, which is in good agreement with our data.

Therefore, we concluded that SmTO films grown on LSAT substrates possess a monoclinic distortion relative to the bulk orthorhombic structure. Moreover, this monoclinic distortion allows for structural reflections at points in reciprocal space where in the orthorhombic structure only magnetic signal is present.

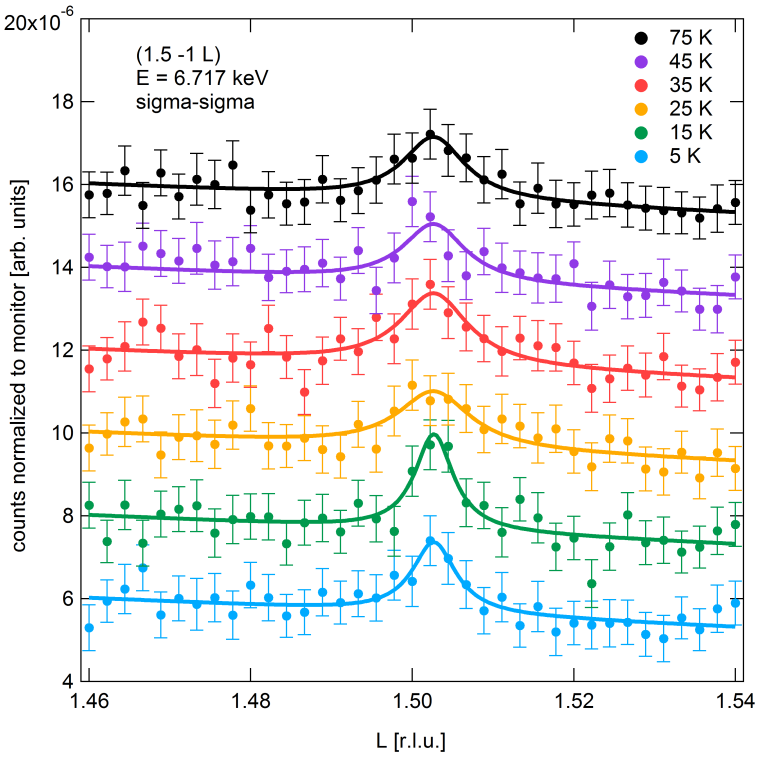

Figure B.1: X-ray resonant scattering L-scans of a $SmTiO_3$ film taken at the Sm L_3-edge showing a weak reflection that is temperature-independent across the known $SmTiO_3$ magnetic transitions.

Unfortunately, the presence of these overlapping structural peaks at the antiferromagnetic Bragg peak locations, combined with the very low intensity of the feature, inhibited our ability to cleanly observe magnetic scattering and determine the magnetic structure of these films.

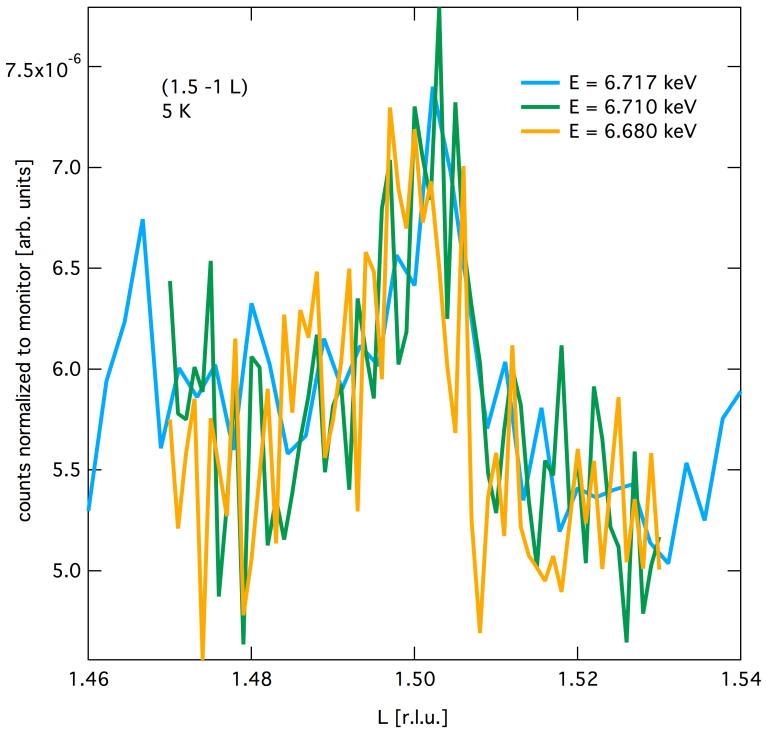

Figure B.2: X-ray resonant scattering L-scans across (3/2 -1 3/2) taken at three energies across the Sm L_3-edge at 5 K.

Bibliography

[1] T. Stocker, *Climate Change 2013: The Physical Science Basis* (Cambridge University Press, 2014).

[2] P. Drude, Ann. Phys. **308**, 369 (1900).

[3] A. Sommerfeld, Z. Phys. **47**, 1 (1928).

[4] G. Zwicknagl, Rep. Prog. Phys. **79**, 124501 (2016).

[5] T. Ramakrishnan, Curr. Sci. **95** (2008).

[6] E. Dagotto, Rev. Mod. Phys. **66**, 763 (1994).

[7] P. A. Lee, N. Nagaosa, and X.-G. Wen, Rev. Mod. Phys. **78**, 17 (2006).

[8] A. Ramirez, J. Phys. Condens. Mat. **9**, 8171 (1997).

[9] E. Dagotto, T. Hotta, and A. Moreo, Physcs. Rep. **344**, 1 (2001).

[10] K. Andres, J. Graebner, and H. Ott, Phys. Rev. Lett. **35**, 1779 (1975).

[11] F. Steglich, J. Aarts, C. Bredl, W. Lieke, D. Meschede, W. Franz, and H. Schäfer, Phys. Rev. Lett. **43**, 1892 (1979).

[12] Q. Si and F. Steglich, Science **329**, 1161 (2010).

[13] N. Mathur, F. Grosche, S. Julian, I. Walker, D. Freye, R. Haselwimmer, and G. Lonzarich, Nature **394**, 39 (1998).

[14] E. Dagotto, Science **309**, 257 (2005).

[15] M. Mochizuki and M. Imada, New J. Phys. **6**, 154 (2004).

[16] A. Komarek, H. Roth, M. Cwik, W.-D. Stein, J. Baier, M. Kriener, F. Bourée, T. Lorenz, and M. Braden, Phys. Rev. B **75**, 224402 (2007).

[17] D. A. MacLean, H.-N. Ng, and J. Greedan, J. Solid State Chem. **30**, 35 (1979).

[18] M. Kubota, H. Nakao, Y. Murakami, Y. Taguchi, M. Iwama, and Y. Tokura, Phys. Rev. B **70**, 245125 (2004).

[19] M. Cwik, T. Lorenz, J. Baier, R. Müller, G. André, F. Bourée, F. Lichtenberg, A. Freimuth, R. Schmitz, E. Müller-Hartmann, et al., Phys. Rev. B **68**, 060401 (2003).

[20] E. Pavarini, A. Yamasaki, J. Nuss, and O. Andersen, New J. Phys. **7**, 188 (2005).

[21] H. D. Zhou and J. B. Goodenough, J. Phys. Condens. Mat. **17**, 7395 (2005).

[22] J. Greedan, J. Less Common Metals **111**, 335 (1985).

[23] A. Ohtomo, D. Muller, J. Grazul, and H. Hwang, Appl. Phys. Lett. **80**, 3922 (2002).

[24] D. A. Muller, N. Nakagawa, A. Ohtomo, J. L. Grazul, and H. Y. Hwang, Nature **430**, 657 (2004).

[25] A. Kalabukhov, R. Gunnarsson, J. Börjesson, E. Olsson, T. Claeson, and D. Winkler, Phys. Rev. B **75**, 121404 (2007).

[26] Y. Kozuka, Y. Hikita, C. Bell, and H. Hwang, Appl. Phys. Lett. **97**, 012107 (2010).

[27] P. Moetakef, D. G. Ouellette, J. Y. Zhang, T. A. Cain, S. J. Allen, and S. Stemmer, J. Cryst. Growth **355**, 166 (2012).

[28] C. A. Jackson, J. Y. Zhang, C. R. Freeze, and S. Stemmer, Nat. Commun. **5** (2014).

[29] K. Ahadi, L. Galletti, and S. Stemmer, Appl. Phys. Lett. **111**, 172403 (2017).

[30] S. Stemmer and S. James Allen, Ann. Rev. Mater. Res. **44**, 151 (2014).

[31] P. Moetakef, T. A. Cain, D. G. Ouellette, J. Y. Zhang, D. O. Klenov, A. Janotti, C. G. Van de Walle, S. Rajan, S. J. Allen, and S. Stemmer, Appl. Phys. Lett. **99**, 232116 (2011).

[32] J. Y. Zhang, C. A. Jackson, S. Raghavan, J. Hwang, and S. Stemmer, Phys. Rev. B **88**, 121104 (2013).

[33] J. Y. Zhang, J. Hwang, S. Raghavan, and S. Stemmer, Phys. Rev. Lett. **110**, 256401 (2013).

[34] J. Y. Zhang, C. A. Jackson, R. Chen, S. Raghavan, P. Moetakef, L. Balents, and S. Stemmer, Phys. Rev. B **89**, 075140 (2014).

[35] B. Jalan, R. Engel-Herbert, N. J. Wright, and S. Stemmer, J. Vac. Sci. Technol. A **27**, 461 (2009).

[36] P. Moetakef, J. Y. Zhang, S. Raghavan, A. P. Kajdos, and S. Stemmer, J. Vac. Sci. Technol. A **31**, 041503 (2013).

[37] B. Jalan, P. Moetakef, and S. Stemmer, Appl. Phys. Lett. **95**, 032906 (2009).

[38] J. Son, P. Moetakef, B. Jalan, O. Bierwagen, N. J. Wright, R. Engel-Herbert, and S. Stemmer, Nat. Mater. **9**, 482 (2010).

[39] P. Moetakef, J. R. Williams, D. G. Ouellette, A. P. Kajdos, D. Goldhaber-Gordon, S. J. Allen, and S. Stemmer, Phys. Rev. X **2**, 021014 (2012).

[40] C. Majkrzak, Physica B **173**, 75 (1991).

[41] A. Greer, J. Magn. Magn. Mater. **126**, 89 (1993).

[42] J. Geissler, E. Goering, M. Justen, F. Weigand, G. Schütz, J. Langer, D. Schmitz, H. Maletta, and R. Mattheis, Phys. Rev. B **65**, 020405 (2001).

[43] E. Benckiser, M. W. Haverkort, S. Brück, E. Goering, S. Macke, A. Frañó, X. Yang, O. K. Andersen, G. Cristiani, H.-U. Habermeier, et al., Nat. Mater. **10**, 189 (2011).

[44] R. Need, B. Isaac, B. J. Kirby, J. A. Borchers, S. Stemmer, and S. D. Wilson, Phys. Rev. Lett. **117**, 037205 (2016).

[45] J.-H. Kim, I. Vrejoiu, Y. Khaydukov, T. Keller, J. Stahn, A. Rühm, D. K. Satapathy, V. Hinkov, and B. Keimer, Phys. Rev. B **86**, 180402 (2012).

[46] H. Jing, D. Hong, B. Kwak, D. Choi, K. Shin, C.-J. Yu, J. Kim, D. Noh, and Y. Seo, Langmuir **25**, 4198 (2009).

[47] K. Kago, H. Matsuoka, R. Yoshitome, H. Yamaoka, K. Ijiro, and M. Shimomura, Langmuir **15**, 5193 (1999).

[48] T. Russell, Mater. Sci. Rep. **5**, 171 (1990).

[49] J. Schmitt, T. Gruenewald, G. Decher, P. S. Pershan, K. Kjaer, and M. Loesche, Macromolecules **26**, 7058 (1993).

[50] R. K. Thomas and J. Penfold, Curr. Opin. Collid In. **1**, 23 (1996).

[51] M. Born and E. Wolf, *Principles of Optics: Electromagnetic Theory of Propagation, Interference and Diffraction of Light* (Elsevier, 2013).

[52] S. Macke and E. Goering, J. Phys. Condens. Mat. **26**, 363201 (2014).

[53] L. G. Parratt, Phys. Rev. **95**, 359 (1954).

[54] J. Zak, E. R. Moog, C. Liu, and S. D. Bader, Phys. Rev. B **43**, 6423 (1991).

[55] S. A. Stepanov and S. K. Sinha, Phys. Rev. B **61**, 15302 (2000).

[56] J. Fink, E. Schierle, E. Weschke, and J. Geck, Rep. Prog. Phys. **76**, 056502 (2013).

[57] S. Grenier and Y. Joly, in *J. Phys. Conf. Ser.* (IOP Publishing, 2014), vol. 519, p. 012001.

[58] F. De Groot, M. Figueiredo, M. Basto, M. Abbate, H. Petersen, and J. Fuggle, Phys. Chem. Miner. **19**, 140 (1992).

[59] J. Hill and D. McMorrow, Acta Crystallogr. A **52**, 236 (1996).

[60] J. Hannon, G. Trammell, M. Blume, and D. Gibbs, Phys. Rev. Lett. **61**, 1245 (1988).

[61] F. De Groot, Coordin. Chem. Rev. **249**, 31 (2005).

[62] Y. Murakami, H. Kawada, H. Kawata, M. Tanaka, T. Arima, Y. Moritomo, and Y. Tokura, Phys. Rev. Lett. **80**, 1932 (1998).

[63] G. Amow, J. Greedan, and C. Ritter, J. Solid State Chem. **141**, 262 (1998).

[64] J. J. Thomson, *Conduction of Electricity Through Gases* (University press, 1903).

[65] A. Fox, M. O'Keefe, and M. Tabbernor, Acta Crystallogr. A **45**, 786 (1989).

[66] S. Caticha-Ellis, *Anomalous Dispersion of X-rays in Crystallography* (University College Cardiff Press, 1981).

[67] F. De Groot and A. Kotani, *Core Level Spectroscopy of Solids* (CRC press, 2008).

[68] B. L. Henke, E. M. Gullikson, and J. C. Davis, Atom. Data Nucl. Data **54**, 181 (1993).

[69] C. T. Chantler, J. Phys. Chem. Ref. Data **29**, 597 (2000).

[70] J. Yano and V. K. Yachandra, Photosynth. Res. **102**, 241 (2009).

[71] F. De Groot, M. Arrio, P. Sainctavit, C. Cartier, and C. Chen, Solid State Commun. **92**, 991 (1994).

[72] R. Kurian, K. Kunnus, P. Wernet, S. M. Butorin, P. Glatzel, and F. M. de Groot, J. Phys. Condens. Mat. **24**, 452201 (2012).

[73] S. Brück, S. Bauknecht, B. Ludescher, E. Goering, and G. Schütz, Rev. Sci. Instrum. **79**, 083109 (2008).

[74] V. Lucarini, J. J. Saarinen, K.-E. Peiponen, and E. M. Vartiainen, *Kramers-Kronig Relations in Optical Materials Research*, vol. 110 (Springer Science & Business Media, 2005).

[75] S. Macke, *Online kramers-kronig transformation of optical constants in the x-ray regime*, URL http://remagx.org/KK.html.

[76] M. Björck and G. Andersson, J. Appl. Crystallogr. **40**, 1174 (2007).

[77] I. A. Zaliznyak and S.-H. Lee, Tech. Rep., Brookhaven National Laboratory (2004).

[78] E. Fermi and L. Marshall, Phys. Rev. **71**, 666 (1947).

[79] J. B. Parise, Rev. Mineral. Geochem. **63**, 1 (2006).

[80] V. F. Sears, *Neutron Optics: An Introduction to the Theory of Neutron Optical Phenomena and Their Applications*, vol. 3 (Oxford University Press, USA, 1989).

[81] M. Fitzsimmons and C. Majkrzak, Mod. Tech. Character, Magn. Mater. p. 107 (2005).

[82] C. Majkrzak, K. O'Donovan, and N. Berk, in *Neutron Scattering from Magnetic Materials*, edited by T. Chatterji (Elsevier Science, Amsterdam, 2006).

[83] G. E. Bacon, *Neutron Diffraction* (Oxford University Press, 1975).

[84] V. F. Sears, Neutron News pp. 26–37 (1992).

[85] F. Ott, C. R. Phys. **8**, 763 (2007).

[86] R. Moon, T. Riste, and W. Koehler, Phys. Rev. **181**, 920 (1969).

[87] C. Dhital, T. Hogan, W. Zhou, X. Chen, Z. Ren, M. Pokharel, Y. Okada, M. Heine, W. Tian, Z. Yamani, et al., Nat. Commun. **5**, 3377 (2014).

[88] K. Kakurai, M. Steiner, R. Pynn, and J. Kjems, J. Phys. Condens. Mat. **3**, 715 (1991).

[89] P. D. De Reotier and A. Yaouanc, J. Phys. Condens. Mat. **9**, 9113 (1997).

[90] S. Cox, J. Phys. C Solid State **20**, 3187 (1987).

[91] E. Morenzoni, H. Glückler, T. Prokscha, R. Khasanov, H. Luetkens, M. Birke, E. Forgan, C. Niedermayer, and M. Pleines, Nucl. Instrum. Meth. B **192**, 254 (2002).

[92] J. Möller, P. Bonfà, D. Ceresoli, F. Bernardini, S. Blundell, T. Lancaster, R. De Renzi, N. Marzari, I. Watanabe, S. Sulaiman, et al., Phys. Scripta **88**, 068510 (2013).

[93] J. E. Sonier, *Muon Spin Rotation/Relaxation/Resonance* (TRIUMF Centre for Molecular and Materials Science, 2002).

[94] E. Brandt, Phys. Rev. B **37**, 2349 (1988).

[95] D. MacLaughlin, D. Cooke, R. Heffner, R. Hutson, M. McElfresh, M. Schillaci, H. Rempp, J. Smith, J. Willis, E. Zirngiebl, et al., Phys. Rev. B **37**, 3153 (1988).

[96] R. Heffner, D. Cooke, A. Giorgi, R. Hutson, M. Schillaci, H. Rempp, J. Smith, J. Willis, D. MacLaughlin, C. Boekema, et al., Phys. Rev. B **39**, 11345 (1989).

[97] S. Dunsiger, R. Kiefl, K. Chow, B. Gaulin, M. Gingras, J. Greedan, A. Keren, K. Kojima, G. Luke, W. MacFarlane, et al., Phys. Rev. B **54**, 9019 (1996).

[98] J. Lago, T. Lancaster, S. Blundell, S. Bramwell, F. Pratt, M. Shirai, and C. Baines, J. Phys. Condens. Mat. **17**, 979 (2005).

[99] Y. Li, D. Adroja, P. K. Biswas, P. J. Baker, Q. Zhang, J. Liu, A. A. Tsirlin, P. Gegenwart, and Q. Zhang, Phys. Rev. Lett. **117**, 097201 (2016).

[100] H. Guo, K. Manna, H. Luetkens, M. Hoelzel, and A. Komarek, Phys. Rev. B **94**, 205128 (2016).

[101] A. Pifer, T. Bowen, and K. Kendall, Nucl. Instrum. Meth. **135**, 39 (1976).

[102] A. Boris, Y. Matiks, E. Benckiser, A. Frano, P. Popovich, V. Hinkov, P. Wochner, M. Castro-Colin, E. Detemple, V. K. Malik, et al., Science **332**, 937 (2011).

[103] L. Schulz, L. Nuccio, M. Willis, P. Desai, P. Shakya, T. Kreouzis, V. K. Malik, C. Bernhard, F. Pratt, N. Morley, et al., Nat. Mater. **10**, 39 (2011).

[104] L. Maurel, N. Marcano, T. Prokscha, E. Langenberg, J. Blasco, R. Guzmán, A. Suter, C. Magén, L. Morellón, M. Ibarra, et al., Phys. Rev. B **92**, 024419 (2015).

[105] T. Prokscha, E. Morenzoni, K. Deiters, F. Foroughi, D. George, R. Kobler, A. Suter, and V. Vrankovic, Nucl. Instrum. Meth. A **595**, 317 (2008).

[106] A. Suter and B. Wojek, Physcs. Proc. **30**, 69 (2012).

[107] H. Y. Hwang, Y. Iwasa, M. Kawasaki, B. Keimer, N. Nagaosa, and Y. Tokura, Nat. Mater. **11**, 103 (2012).

[108] A. Bhattacharya, S. J. May, S. G. E. te Velthuis, M. Warusawithana, X. Zhai, B. Jiang, J.-M. Zuo, M. R. Fitzsimmons, S. D. Bader, and J. N. Eckstein, Phys. Rev. Lett. **100**, 257203 (2008).

[109] A. Vailionis, H. Boschker, Z. Liao, J. R. A. Smit, G. Rijnders, M. Huijben, and G. Koster, Appl. Phys. Lett. **105**, 131906 (2014).

[110] J. M. Rondinelli, S. J. May, and J. W. Freeland, MRS Bull. **37**, 261 (2012).

[111] S. Stemmer and A. J. Millis, MRS Bull. **38**, 1032 (2013).

[112] E. Mikheev, C. R. Freeze, B. J. Isaac, T. A. Cain, and S. Stemmer, Phys. Rev. B **91**, 165125 (2015).

[113] C. A. Jackson and S. Stemmer, Phys. Rev. B **88**, 180403 (2013).

[114] J. A. Borchers, J. F. Ankner, C. F. Majkrzak, B. N. Engel, M. H. Wiedmann, R. A. Van Leeuwen, and C. M. Falco, J. App. Phys. **75**, 6498 (1994).

[115] B. J. Kirby, J. W. Lau, D. V. Williams, C. A. Bauer, and C. W. Miller, J. App. Phys. **109**, 063905 (2011).

[116] T. S. Santos, B. J. Kirby, S. Kumar, S. J. May, J. A. Borchers, B. B. Maranville, J. Zarestky, S. G. E. te Velthuis, J. van den Brink, and A. Bhattacharya, Phys. Rev. Lett. **107**, 167202 (2011).

[117] B. Kirby, P. Kienzle, B. Maranville, N. Berk, J. Krycka, F. Heinrich, and C. Majkrzak, Curr. Opin. Collid In. **17**, 44 (2012).

[118] J. Lynn and P. Seeger, Atom. Data Nucl. Data **44**, 191 (1990).

[119] J. F. Ankner, C. F. Marjkrzak, and S. K. Satija, J. Res. Natl. Inst. Stand. Technol. **98**, 47 (1993).

[120] F. Ott, J. Phys. Condens. Mat. **20**, 264009 (2008).

[121] A. Bhattacharya and S. J. May, Ann. Rev. Mater. Res. **44**, 65 (2014).

[122] K. Takahashi, M. Kawasaki, and Y. Tokura, Appl. Phys. Lett. **79**, 1324 (2001).

[123] N. Reyren, S. Thiel, A. Caviglia, L. F. Kourkoutis, G. Hammerl, C. Richter, C. Schneider, T. Kopp, A.-S. Rüetschi, D. Jaccard, et al., Science **317**, 1196 (2007).

[124] A. Caviglia, S. Gariglio, N. Reyren, D. Jaccard, T. Schneider, M. Gabay, S. Thiel, G. Hammerl, J. Mannhart, and J.-M. Triscone, Nature **456**, 624 (2008).

[125] P. M. Woodward, Acta Crystallogr. A **53**, 32 (1997).

[126] V. M. Goldschmidt, Naturwissenschaften **14**, 477 (1926).

[127] T. Katsufuji, Y. Okimoto, and Y. Tokura, Phys. Rev. Lett. **75**, 3497 (1995).

[128] T. Katsufuji, Y. Taguchi, and Y. Tokura, Phys. Rev. B **56**, 10145 (1997).

[129] S. May, J.-W. Kim, J. Rondinelli, E. Karapetrova, N. Spaldin, A. Bhattacharya, and P. Ryan, Phys. Rev. B **82**, 014110 (2010).

[130] S. May, C. Smith, J.-W. Kim, E. Karapetrova, A. Bhattacharya, and P. Ryan, Phys. Rev. B **83**, 153411 (2011).

[131] H. Wang, J. Wen, D. J. Miller, Q. Zhou, M. Chen, H. N. Lee, K. M. Rabe, and X. Wu, Phys. Rev. X **6**, 011027 (2016).

[132] X. Zhai, L. Cheng, Y. Liu, C. M. Schlepütz, S. Dong, H. Li, X. Zhang, S. Chu, L. Zheng, J. Zhang, et al., Nat. Commun. **5** (2014).

[133] K. Hayashi, M. Sawada, H. Yamagami, A. Kimura, and A. Kakizaki, Physica B **351**, 324 (2004).

[134] K. Oguz, P. Jivrajka, M. Venkatesan, G. Feng, and J. M. D. Coey, J. Appl. Phys. **103**, 07B526 (2008).

[135] S. Y. Jang, S. Lim, and S. Lee, J. Appl. Phys. **107**, 09C707 (2010).

[136] J. Freeland, J. Kavich, K. Gray, L. Ozyuzer, H. Zheng, J. Mitchell, M. Warusawithana, P. Ryan, X. Zhai, R. Kodama, et al., J. Phys. Condens. Mat. **19**, 315210 (2007).

[137] T. L. Meyer, A. Herklotz, V. Lauter, J. W. Freeland, J. Nichols, E.-J. Guo, S. Lee, T. Z. Ward, N. Balke, S. V. Kalinin, et al., Phys. Rev. B **94**, 174432 (2016).

[138] S. Liang, J. Sun, J. Wang, and B. Shen, Appl. Phys. Lett. **95**, 182509 (2009).

[139] Y. Sun, Y. Zhao, H. Tian, C. Xiong, B. Xie, M. Zhu, S. Park, W. Wu, J. Li, and Q. Li, Phys. Rev. B **78**, 024412 (2008).

[140] M. Bibes, S. Valencia, L. Balcells, B. Martínez, J. Fontcuberta, M. Wojcik, S. Nadolski, and E. Jedryka, Phys. Rev. B **66**, 134416 (2002).

[141] J. Chakhalian, J. Freeland, H.-U. Habermeier, G. Cristiani, G. Khaliullin, M. Van Veenendaal, and B. Keimer, Science **318**, 1114 (2007).

[142] M. Salluzzo, J. Cezar, N. Brookes, V. Bisogni, G. De Luca, C. Richter, S. Thiel, J. Mannhart, M. Huijben, A. Brinkman, et al., Phys. Rev. Lett. **102**, 166804 (2009).

[143] E. Moon, P. Balachandran, B. J. Kirby, D. Keavney, R. Sichel-Tissot, C. Schleputz, E. Karapetrova, X. Cheng, J. M. Rondinelli, and S. May, Nano Lett. **14**, 2509 (2014).

[144] A. Tebano, C. Aruta, S. Sanna, P. Medaglia, G. Balestrino, A. Sidorenko, R. De Renzi, G. Ghiringhelli, L. Braicovich, V. Bisogni, et al., Phys. Rev. Lett. **100**, 137401 (2008).

[145] S. Sachdev, Science **288**, 475 (2000).

[146] T. Senthil, L. Balents, S. Sachdev, A. Vishwanath, and M. P. Fisher, Phys. Rev. B **70**, 144407 (2004).

[147] T. Timusk and B. Statt, Rep. Prog. Phys. **62**, 61 (1999).

[148] M. Norman, D. Pines, and C. Kallin, Adv. Phys. **54**, 715 (2005).

[149] H. Ding, T. Yokoya, J. Campuzano, T. Takahashi, et al., Nature **382**, 51 (1996).

[150] T. Kondo, R. Khasanov, T. Takeuchi, J. Schmalian, and A. Kaminski, Nature **457**, 296 (2009).

[151] M. Kastner, R. Birgeneau, G. Shirane, and Y. Endoh, Rev. Mod. Phys. **70**, 897 (1998).

[152] B. Sipos, A. F. Kusmartseva, A. Akrap, H. Berger, L. Forró, and E. Tutiš, Nat. Mater. **7**, 960 (2008).

[153] J. Chang, E. Blackburn, A. Holmes, N. Christensen, J. Larsen, J. Mesot, R. Liang, D. Bonn, W. Hardy, A. Watenphul, et al., Nat. Phys. **8**, 871 (2012).

[154] J. Tranquada, J. Axe, N. Ichikawa, Y. Nakamura, S. Uchida, and B. Nachumi, Phys. Rev. B **54**, 7489 (1996).

[155] T. Hogan, Z. Yamani, D. Walkup, X. Chen, R. Dally, T. Z. Ward, M. P. M. Dean, J. Hill, Z. Islam, V. Madhavan, et al., Phys. Rev. Lett. **114**, 257203 (2015).

[156] C.-H. Yee and L. Balents, Phys. Rev. X **5**, 021007 (2015).

[157] T. Saitoh, D. Dessau, Y. Moritomo, T. Kimura, Y. Tokura, and N. Hamada, Phys. Rev. B **62**, 1039 (2000).

[158] M. Uchida, K. Ishizaka, P. Hansmann, Y. Kaneko, Y. Ishida, X. Yang, R. Kumai, A. Toschi, Y. Onose, R. Arita, et al., Phys. Rev. Lett. **106**, 027001 (2011).

[159] A. de la Torre, S. M. Walker, F. Y. Bruno, S. Riccó, Z. Wang, I. G. Lezama, G. Scheerer, G. Giriat, D. Jaccard, C. Berthod, et al., Phys. Rev. Lett. **115**, 176402 (2015).

[160] P. B. Marshall, E. Mikheev, S. Raghavan, and S. Stemmer, Phys. Rev. Lett. **117**, 046402 (2016).

[161] Z. Salman, T. Prokscha, A. Amato, E. Morenzoni, R. Scheuermann, K. Sedlak, and A. Suter, Phys. Rev. Lett. **113**, 156801 (2014).

[162] A. Boris, Y. Matiks, E. Benckiser, A. Frano, P. Popovich, V. Hinkov, P. Wochner, M. Castro-Colin, E. Detemple, V. K. Malik, et al., Science **332**, 937 (2011).

[163] E. Stilp, A. Suter, T. Prokscha, E. Morenzoni, H. Keller, B. M. Wojek, H. Luetkens, A. Gozar, G. Logvenov, and I. Božović, Phys. Rev. B **88**, 064419 (2013).

[164] C. W. Schneider, S. Mukherjee, K. Shimamoto, S. Das, H. Luetkens, J. S. White, M. Bator, Y. Hu, J. Stahn, T. Prokscha, et al., Phys. Rev. B **94**, 054423 (2016).

[165] N. Pavlenko, T. Kopp, E. Y. Tsymbal, J. Mannhart, and G. A. Sawatzky, Phys. Rev. B **86**, 064431 (2012).

[166] R. J. Birgeneau, C. Stock, J. M. Tranquada, and K. Yamada, J. Phys. Soc. Japan **75**, 111003 (2006).

[167] X. Chen, T. Hogan, D. Walkup, W. Zhou, M. Pokharel, M. Yao, W. Tian, T. Z. Ward, Y. Zhao, D. Parshall, et al., Phys. Rev. B **92**, 075125 (2015).

[168] H. Gretarsson, N. Sung, J. Porras, J. Bertinshaw, C. Dietl, J. A. Bruin, A. Bangura, Y. Kim, R. Dinnebier, J. Kim, et al., Phys. Rev. Lett. **117**, 107001 (2016).

[169] M. Mochizuki and M. Imada, J. Phys. Soc. Jpn. **73**, 1833 (2004).

[170] R. Need, B. Isaac, B. J. Kirby, S. Stemmer, and S. D. Wilson, Submitted for review (2017).

[171] R. Need, P. Marshall, E. Kenney, A. Suter, T. Prokscha, Z. Salman, B. J. Kirby, S. Stemmer, M. Graf, and S. D. Wilson, Submitted for review (2017).

[172] E. Lesne, N. Reyren, D. Doennig, R. Mattana, H. Jaffrès, V. Cros, F. Petroff, F. Choueikani, P. Ohresser, R. Pentcheva, et al., Nat. Commun. (2014).

[173] S. Macke, A. Radi, J. E. Hamann-Borrero, A. Verna, M. Bluschke, S. Brück, E. Goering, R. Sutarto, F. He, G. Cristiani, et al., Adv. Mater. **26**, 6554 (2014).

[174] M. Zwiebler, J. Hamann-Borrero, M. Vafaee, P. Komissinskiy, S. Macke, R. Sutarto, F. He, B. Büchner, G. Sawatzky, L. Alff, et al., New J.Phys. **17**, 083046 (2015).

[175] A. Ruosi, C. Raisch, A. Verna, R. Werner, B. Davidson, J. Fujii, R. Kleiner, and D. Koelle, Phys. Rev. B **90**, 125120 (2014).

[176] Y. Cao, Z. Yang, M. Kareev, X. Liu, D. Meyers, S. Middey, D. Choudhury, P. Shafer, J. Guo, J. Freeland, et al., Phys. Rev. Lett. **116**, 076802 (2016).

[177] Y. Cao, X. Liu, M. Kareev, D. Choudhury, S. Middey, D. Meyers, J.-W. Kim, P. Ryan, J. Freeland, and J. Chakhalian, Nat. Commun. **7** (2016).

[178] J. Stöhr, J. Electron Spectrosc. **75**, 253 (1995).

[179] D. Brewster, Philos. T. R. Soc. Lond. **105**, 125 (1815).

[180] E. Mete, R. Shaltaf, and Ş. Ellialtıoğlu, Phys. Rev. B **68**, 035119 (2003).

[181] T. Yajima, H. Suzuki, T. Yogo, and H. Iwahara, Solid State Ionics **51**, 101 (1992).

[182] A. Garg and D. Agrawal, Mat. Sci. Eng. B **86**, 134 (2001).

[183] Q. Xu, W. Pan, J. Wang, C. Wan, L. Qi, H. Miao, K. Mori, and T. Torigoe, J. Am. Ceram. Soc. **89**, 340 (2006).

[184] A. Y. Cho and J. Arthur, Prog. Solid State Chem. **10**, 157 (1975).

[185] Q. H. Wang, K. Kalantar-Zadeh, A. Kis, J. N. Coleman, and M. S. Strano, Nat. Nano. **7**, 699 (2012).

[186] D. H. Keum, S. Cho, J. H. Kim, D.-H. Choe, H.-J. Sung, M. Kan, H. Kang, J.-Y. Hwang, S. W. Kim, H. Yang, et al., Nat. Phys. **11** (2015).

[187] J. Wilson and A. Yoffe, Adv. Phys. **18**, 193 (1969).

[188] R. Morris, R. Coleman, and R. Bhandari, Phys. Rev. B **5**, 895 (1972).

[189] D. E. Moncton, J. Axe, and F. DiSalvo, Phys. Rev. B **16**, 801 (1977).

[190] R. Nitsche, H. Bölsterli, and M. Lichtensteiger, J. Phys. Chem. Solids **21**, 199 (1961).

[191] M. Binnewies, R. Glaum, M. Schmidt, and P. Schmidt, Z. Anorg. Allg. Chem. **639**, 219 (2013).

[192] B. Dalrymple, S. Mroczkowski, and D. Prober, J. Cryst. Growth **74**, 575 (1986).

[193] X. Qian, J. Liu, L. Fu, and J. Li, Science **346**, 1344 (2014).

[194] M. N. Ali, J. Xiong, S. Flynn, J. Tao, Q. D. Gibson, L. M. Schoop, T. Liang, N. Haldolaarachchige, M. Hirschberger, N. Ong, et al., Nature **514**, 205 (2014).

[195] M. N. Ali, L. Schoop, J. Xiong, S. Flynn, Q. Gibson, M. Hirschberger, N. Ong, and R. Cava, Europhys. Lett. **110**, 67002 (2015).

[196] A. Mar and J. A. Ibers, J. Am. Chem. Soc. **115**, 3227 (1993).

[197] J. Li, M. E. Badding, and F. DiSalvo, Inorg. Chem. **31**, 1050 (1992).

[198] A. Mar and J. A. Ibers, J. Solid State Chem. **97**, 366 (1992).

[199] A. Mar, S. Jobic, and J. A. Ibers, J. Am. Chem. Soc. **114** (1992).

[200] J. Liu, H. Wang, C. Fang, L. Fu, and X. Qian, Nano Lett. **17**, 467 (2017).

[201] T. Skyrme, Nucl. Phys. **31**, 556 (1962).

[202] S. Heinze, K. Von Bergmann, M. Menzel, J. Brede, A. Kubetzka, R. Wiesendanger, G. Bihlmayer, and S. Blügel, Nat. Phys. **7**, 713 (2011).

[203] A. Fert, V. Cros, and J. Sampaio, Nat. Nano. **8**, 152 (2013).

[204] F. Jonietz, S. Mühlbauer, C. Pfleiderer, A. Neubauer, W. Münzer, A. Bauer, T. Adams, R. Georgii, P. Böni, R. Duine, et al., Science **330**, 1648 (2010).

[205] X. Yu, N. Kanazawa, W. Zhang, T. Nagai, T. Hara, K. Kimoto, Y. Matsui, Y. Onose, and Y. Tokura, Nat. Commun. **3**, 988 (2012).

[206] H. Wilhelm, M. Schmidt, R. Cardoso-Gil, U. Burkhardt, M. Hanfland, U. Schwarz, and L. Akselrud, Sci. Technol. Adv. Mat. **8**, 416 (2007).

[207] M. Richardson, Acta Chem. Scand **21** (1967).

[208] B. Lebech, J. Bernhard, and T. Freltoft, J. Phys. Condens. Mat. **1**, 6105 (1989).

[209] H. Wilhelm, M. Baenitz, M. Schmidt, C. Naylor, R. Lortz, U. Rößler, A. Leonov, and A. Bogdanov, J.Phys.Condens. Mat. **24**, 294204 (2012).

[210] S. Huang and C. Chien, Phys. Rev. Lett. **108**, 267201 (2012).

[211] J. Gallagher, K. Meng, J. Brangham, H. Wang, B. Esser, D. McComb, and F. Yang, Phys. Rev. Lett. **118**, 027201 (2017).

[212] C. Moreau-Luchaire, C. Moutafis, N. Reyren, J. Sampaio, C. Vaz, N. Van Horne, K. Bouzehouane, K. Garcia, C. Deranlot, P. Warnicke, et al., Nat. Nanotech. **11**, 444 (2016).

[213] A. Vailionis, H. Boschker, W. Siemons, E. P. Houwman, D. H. Blank, G. Rijnders, and G. Koster, Phys. Rev. B **83**, 064101 (2011).